DEVELOPMENT AND THERMAL PROPERTIES OF CARBON NANOTUBE-POLYMER COMPOSITES

By

Enrique Monte Jackson

Dissertation

Submitted to the Faculty of the

Graduate School of Vanderbilt University

in partial fulfillment of the requirements

for the degree of

DOCTOR OF PHILOSOPHY

in

Interdisciplinary Materials Science

December, 2014

Nashville, Tennessee

Approved:

Dr. Paul E. Laibinis, Chair

Dr. Warren E. Collins

Dr. Yaqiong Xu

Dr. Timothy Hanusa

Dr. Benjamin Penn

DEDICATION

First of all, I dedicate this dissertation to God who gave me the peace in the midst of it all. To my wife, Mrs. Natasha W. Jackson. I love you very much and thank you for your support and dedication throughout this process. To my late mother Katie Jackson Mangum and my sister Ovetta Jackson, I am finally done!!!! I know both of you are looking down on me and I pray that I am still making you proud. The Johnson family, [Jake, Monakia, Jake Jr. Otis and Ja'vett], thank you all for the support you given me over the years and this is part III of this saga. Mona, Bam and Otis, I am keeping true to my goals and there is no excuse for you not doing the same. The Staine family, [Luella, Kenneth, and Kenisha], I am eternally grateful for the love you gave to me and I am still working hard to make you proud. To my late grandmother, Rachel "Suge" Jackson, keep looking down on me and give me the strength to persevere through it all. The Burrell family, [Gertrude, Lavar, Deanna, James], thank you again for your wisdom, knowledge, patience and the love you have given me over the years. I also dedicate this book to my family and friends that gave me the motivation to keep striving to accomplish my dreams. Finally, I dedicate this dissertation to my brothers of Omega Psi Phi Fraternity, Inc. and the brothers of P.H.F.&.A.M.

ACKNOWLEDGMENTS

I would like to express my deep appreciation in invaluable support from many people throughout my graduate studies at Vanderbilt University culminating in dissertation. I acknowledge my mentors, Dr. Paul E. Laibinis, Dr. Tim Hanusa, Dr. Yaqiong Xu, Dr. Benjamin Penn, Dr. Dennis Tucker and especially Dr. Warren Eugene Collins for their expertise in directing and assisting in laboratory training. I acknowledge my mentors again for their encouraging comments, taking the risks, challenging my abilities, believing in my talents, and never giving up on that belief. I acknowledge Fisk University professors Dr. Akira Ueda, Dr. Chen and Dr. Burger for their continued help in this endeavor. I acknowledge Dr. Choi of Vanderbilt University VINSE laboratories for the use of the carbon deposition chamber.

I would like to acknowledge NASA-MSFC Engineering Directorate for the use of their facilities to finish this project. In particular, Wendell Colberg, Dr. Surendra Singhal, Gail Gordon, James Perkins, Charles "Doug" Wingard, Dr. Frank Ledbetter, Justin Jackson, Dr. Vernotto McMillian, Deborah Bagdigian, Paul Luz, Terrie Gardner, Bruce Bice, Dion Jones, Greg Belue, Eddie Davis, Dr. Curtis Banks, Leonard Alexander, Howard Gibson, Lewis "Chip" Moore, Brittany Boykin, James Morgan, Janice Holden, Brett Smith, Dr. Preston McGill and James Bailey, thank you all for your support.

I would like to acknowledge Dr. John Baker, Janelle Ballard, Joann Scales, Dr. Ebony Walker, Dr. LaQuieta Huey and Dr. Kristen Campbell for your continued support through this endeavor. I finally acknowledge all of my family and friends for your continued support.

TABLE OF CONTENTS

Page

LIST OF TABLES

Table Page

LIST OF FIGURES

Figure Page

LIST OF ABBREVIATIONS AND SYMBOLS

A	Cross-sectional Area
AFM	Atomic force microscopy
C_p	Specific heat capacity
CNT	Carbon nanotube
CVD	Chemical vapor deposition
DSC	Differential scanning calorimetry
HiPco	High pressure carbon monoxide disproportionation process
IPA	Isopropyl alcohol
K_{cp}	Specific heat calibration factor
L	Thickness
MWCNT	Multi-walled carbon nanotube
Q	Heat energy
RBM	Radial breathing mode
SWCNT	Single-walled carbon nanotube
T	Temperature
$t_{1/2}$	Time to half-maximum rise
T_g	Glass transition temperature
TGA	Thermogravimetric analysis
x	Length
α	Thermal diffusivity
λ	Thermal conductivity
ρ	Density

CHAPTER I

INTRODUCTION

Favorable strengths, stiffness, thermal conductivities, and lightweight characteristics are critical property requirements for materials used for aerospace structure and vehicles. For many of these systems, lightweight aluminum alloys such as 2219, 2090, and 2195 are currently used. These three alloys were used in vehicles such as those in the Shuttle and Ares 1-X spacecraft programs and have limited uses in NASA's Space Launch Systems heavy launch vehicle. Some of the problems with these alloys (and or most metals) are that they exhibit reduced thermal conductivities at higher temperatures and that they have high densities in comparison with those for polymers that could serve as structural replacements. Lighter weight alternatives to these alloys that could also provide superior thermal properties would provide immediate benefits in the design and operation of future vehicles.

Carbon nanotubes (CNTs) exhibit a remarkable set of electrical, mechanical, and thermal properties that offer opportunities for materials design for aerospace and other applications.[1,2] Their densities are less than half that of aluminum alloys. While there has been extensive research on the properties of CNTs[1-13] where they have not reached their full potential as additives within composites.[2] To access the favorable thermal properties provided by CNTs in practical aerospace structures or components, the CNTs will need to be assembled into mechanically robust elements that could comprise functional macroscopic structures. An approach would be to incorporate the CNTs within prepreg composite structural elements at sufficient quantities to provide significantly improved properties.

Highly efficient components are required for heat dissipation and heat exchange within the thermal transfer and control systems of many industrial processing and maintenance architectures. Relatedly, materials with high thermal conductivities and directional heat dissipating paths are an important part of successful interstellar space vehicles. The effective development of nanomaterials and technologies with improved thermal conduction and transfer characteristics will impact many figures of merit in assembled units, such as performance, capacity, reliability, and safety. The potential impacts of CNT-based composites and nanomaterials on the aerospace industry are summarized in Table 1.1 – 1.

Table 1.1–1. Potential impacts of CNT-based composites on the aerospace industry.

Advance technology	Expand capacity
• Enable fast heat dissipation in critical structural or functional components • Improve the performance of thermal control system • Encourage performance-based standards for aerospace composites	• Enable multifunctionalities, such as extreme load bearing and electrical conductivity. • Allow structures directly tailored to vehicle and systems needs • Satisfy future growth in demand
Increase vehicle flexibility	**Enhance safety**
• Reduce the weight of space and airship vehicles • Increase the flexibility and efficiency gains of current space vehicles and management systems • Lower the launch cost	• Minimize the impact of temperature, friction and other conditions • Successful implementation of the properties would Improve safety of air transportation systems

The advantages provided by SWCNTs as replacements for metal components used for thermal transfer in aerospace applications is readily apparent by comparing their physical properties. Table 1.1–2 summarizes the thermal conductivities and densities of various metals and compares them to the values for SWCNTs. A number of comparisons between the metals and the SWCNTs are worth noting. First, the thermal conductivity of the SWCNTs is higher at all temperatures than for any of the metals. For instance, gold is regularly considered a very

good thermal conductor; however, the thermal conductivity at 300 K for SWCNTs is more than 50 times that of gold. A notable difference between the metals and the SWCNTs is that as temperature increases, the thermal conductivity of metals decreases, while the thermal conductivity for SWCNT increases.

Table 1.1–2. Thermal conductivities and densities of various metals and SWCNTs. [81,83,84]

	Thermal Conductivity (W/m–K)							
Temperature (K)	Aluminum	Copper	Gold	Iron	Platinum	Silver	Tungsten	Aligned SWCNTs
100	3.0	4.83	3.45	1.32	0.79	4.50	2.35	58
200	2.37	4.13	3.27	0.94	0.748	4.30	1.97	158
300	2.37	3.98	3.15	0.803	0.730	4.27	1.78	215
400	2.40	3.92	3.12	0.694	0.722	4.20	1.62	235
	Density (kg/m^3)							
300	2699	8930	19320	7870	21450	10491	19300	1550

Table 1.1-2 also shows that the density for the SWCNTs is less than for any of the metals. In particular, aluminum is currently used in many aerospace applications as this material offers the combination of good thermal conductivity and low density. Notably, the SWCNTs have a density that is ~40% lower than for aluminum and they offer a much higher thermal conductivity. By providing both a higher thermal conductivity and a lower density, SWCNTs could offer a promising substitute for the present metals used in many aerospace applications.

The ability to develop future high performance composites for thermal management applications will rely on the ability to incorporate the exceptional thermal properties of carbon nanotubes into existing materials. Systems that could make immediate use of these capabilities are heat dissipating components and heat exchangers. Advancements in developing such

materials and manufacturing technologies would offer particular benefits for future space vehicles due to their weight reduction.

There are three major challenges existing in my research: (1) the ability to disperse CNTs in a solvent for casting, (2) uniformly coating of a composite with a CNTs, and (3) measuring the thermal properties of the developed nanocomposites. CNTs have a tendency to form agglomerates and bundles due to the van der Waals attraction between each set of tubes. Functionalization, high shear mixing, ultra-sonication, and surfactant wrapping are some of the methods employed in the literature to assist in uniformly dispersing nanotubes in a solvent. When the thermal properties of the composite are under consideration, functionalization and surfactant wrapping disrupt the sidewall sp^2 hybridization and reduce the thermal conductivity of the nanotubes. Therefore, there is a trade-off between avoiding functionalization of the CNTs and achieving good dispersions. Since nanotubes conduct along their length, their alignment is additionally important for achieving optimal thermal properties. A good dispersion of single-walled carbon nanotubes (SWCNTs) in solution along with modest alignment on the prepreg composite are important needs for this research.

Besides the above mentioned challenges in processing highly conductive composites for large scale purposes, their potential as reinforcing agents continues to be a dominant motivation for further research in this area. As new applications for CNTs emerge, it is necessary to understand the basic thermal behavior of these nano-scaled materials.

The overall goal of this thesis is to develop carbon nanotube-polymer composites with enhanced thermal properties so that they can replace traditional aerospace metallic materials, providing the advantage of reduced weight for thermal processing equipment within space structures. The organization of this dissertation is as follows: The properties of carbon

nanotubes and the factors that influence their thermal properties are discussed in Chapter 2 along with a brief discussion of polymer nanocomposites and their thermal properties.

Chapter 3 summarizes the methods used for dispersing the SWCNTs, applying the SWCNTs to composite plies, and the laying up the plies into multilayered hybrid composite films. The dispersion of the SWCNTs, their surface coverage on the composite plies, the effects of processing, and the characterization of these hybrid composites are detailed.

Chapter 4 presents measurements of the thermal properties of the hybrid composites. Raman spectroscopy and thermogravimetric analysis (TGA) were used to analyze the chemical composition and purity of the SWCNTs. Dispersion of the SWCNTs by ultrasonication and spraying of the SWCNTs onto an IM7 composite were used in prepared the hybrid composites. Thermal measurements were made of the final multilayered structures to determine the thermal diffusivity (α), specific heat (C_p), and density (ρ) values of the hybrid composite for examination of the influences of SWCNT content and temperature, and for comparison to literature values.

Chapter 5 presents a theoretical analysis on the expected effects of SWCNT incorporation on the thermal properties of these hybrid nanocomposites, both as a function of the SWCNT volume fraction and temperature. Two models were developed to predict the thermal transport (α and λ) properties of the hybrid composites, depending on the CNT composition and distribution with the composite. Further, a finite element model was used to examine how changes in the thermal properties of the composite would affect its performance within the specific application of the hybrid composite material as a thermal radiator.

Chapter 6 provides a summary of results for this dissertation along with suggestions for future work.

CHAPTER II

BACKGROUND ON POLYMER NANOCOMPOSITES AND CARBON NANOTUBES

2.1 POLYMER NANOCOMPOSITES

A material that consists of two or more physically or chemically different components separated by an interface is called a composite.[3] Composites are used to improve current designs in high performance aeronautics/aerospace applications such as in space exploratory vehicles, with examples including their use in airframes, pipes, heat exchangers, and propulsion.[4] Composites can be classified based on the manner that the additive is distributed. Common types include particulate-reinforced composites, fiber-reinforced composites, and laminar composites that differ in how the components are structured.[5] The composites prepared in this study using SWCNTs as additives were laminar composites and consisted of multiple stacked layers. In general, laminar composites are composed of two or more layers with two of their dimensions larger than their third.[5]

Polymer nanocomposites are a class of materials where at least one of the dimensions of the filler material is of the order of a nanometer.[2] The unique combination of the nanomaterial's characteristics (size, electrical, thermal and mechanical properties) and the abilities for low concentrations of them to change the composite properties has made them one of the most sought-after materials for a variety of applications.[6]

Nanoscale composites can yield unique properties by decreasing the composite structure down to the nanoscale. Common types of nanomaterials are silica nanoparticles, carbon black, carbon nanotubes, and nanofibers. An advantage of using nanomaterials in composites is their large surface area. The surface area per unit volume of a nanomaterial increases as its smallest defining dimension decreases.[7] The majority of the physical and chemical interactions between the composite and the materials within it are directed by the surface properties. As a result, surface area can play a major role in defining the properties of a composite material. The high surface areas and the presence of quantum effects are two main factors that differentiate the properties of nanomaterials from those of other materials.[8] The focus of this dissertation is the use of carbon nanotubes for enhancing the thermal properties of a composite material. The following sections provide overviews of the properties of carbon nanotubes, approaches for polymer composite processing, and the techniques used to measure thermal properties.

2.2 BACKGROUND ON CARBON NANOTUBES AND THEIR THERMAL PROPERTIES

Carbon nanotubes have been investigated across many areas of materials science for their unique thermal, mechanical and electrical properties.[9-10] Nanoscale carbon tubes were first described in the literature almost 40 years ago.[9] In 1991 Sumio Iijima of the NEC Corporation, when characterizing these tubes by transmission electron microscopy (TEM), discovered that their structures consisted of coaxial tubes of graphitic sheets ranging in number from 2 to 50 bundles.[10] Since then, they have been explored for use in sensors, propulsion systems, solar arrays, etc.[9-20]

Single-wall carbon nanotubes (SWCNT) consists of graphene sheets (graphene being the same poly-aromatic monoatomic layer of hexagonally arranged sp^2-hybridized carbon atoms that stacked together forms graphite) rolled into cylinders with fullerene caps of appropriate diameter at their ends (Figure 2.2-1).[11] SWCNT have diameters that range in size from 0.5 – 2.0 nm and lengths that can be more than a micron.

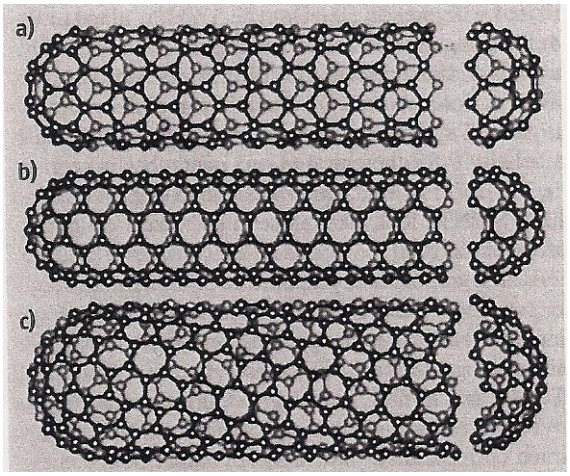

Figure 2.2–1. Illustration of three different SWCNT structures (a) a zig-zag type nanotube, (b) an armchair type nanotube, and (c) a helical (chiral) type nanotube. From Reference 11.

As a consequence of having small defects along their cylindrical topography, SWCNTs exhibit large mean free paths that result in their high thermal conductivity.[11] Theoretical values for their thermal conductivity are as high as 6000 $\frac{W}{m-K}$ while measurements across single MWCNTs have been reported as high as 3000 $\frac{W}{m-K}$.[12-14] The thermal conductivities of polymer composites have been increased by incorporating dispersions of carbon nanotubes; however, the observed increases have been slight because phonon transfer between the added CNTs in the composites was poor.[15-16] For the system explored in this dissertation, SWCNTs were

added as layers to the composite using dispersions of different concentrations. The SWCNT content in the composite was sufficiently high to allow for phonon transfer between the incorporated CNTs and increase the thermal conductivity of the overall composite structure.

2.3 CARBON NANOTUBE PRODUCTION

Carbon nanotubes have been synthesized mainly by three techniques: electric arc discharge, laser ablation, and chemical vapor deposition (CVD). The electric arc discharge technique vaporizes carbon in the presence of a catalyst (iron, cobalt, yttrium, boron, gadolinium, etc.) under an atmosphere of helium or argon.[11] The resulting products contain various graphitic structures, and a purification procedure is needed to obtain high purity CNTs. This process produces research grade CNTs and is not used commercially.

Laser ablation is another technique in which a graphite target is vaporized with a high energy laser and products are retained on a water-cooled copper collector.[11] This technique yields MWCNTs with lengths of 300 nm.[11] Nickel and cobalt are catalysts that can form SWCNTs along with MWCNTs.[11] Extensive purification of the products is required to produce pure CNT materials and the process yields only small batch quantities.

Chemical vapor deposition (CVD) is the most common technique for producing carbon nanotubes. CVD involves the flow of a precursor gas or gases into a chamber containing one or more heated objects to be coated.[17] Chamber temperature of 200 – 1600 °C and plasmas, ions, photons, lasers, hot filaments, or combustion reactions are used to vary the deposition rate.[16] Metal particles can be introduced in the vapor phase through the decomposition of metal-containing species such as ferrocene[18] or iron pentacarbonyl.[19] To promote CNT growth during CVD, catalyst materials are introduced to the chamber to aid in this process. Metal thin

film deposition on silicon substrates has become a common method for creating precise thicknesses of films that can then be heated to form metal nanoparticles appropriate for carbon nanotube growth. Modifying the thickness of the catalyst film affects the particle size and distribution.[20] CNTs produced by this method range in length from tens of microns to millimeters. The SWCNTs that were used in this dissertation and obtained from US Research Nanomaterials, Inc. (Houston TX) were produced by a CVD process.

2.4 METHODS FOR DISPERSING CNTs

Uniform distribution and a good dispersion of the reinforcements are requirements for the high performance of hybrid composites.[33] Dispersion refers to the allocation of the reinforcement within the matrix, whereas the distribution indicates the breaking of the aggregates into small sizes.[33] An adequate distribution does not necessarily mean a good dispersion, as is illustrated in Figure 2.4–1 for the cases of differing levels of distribution and dispersion. Figure 2.4–1a shows a case of poor distribution and poor dispersion, while Figure 2.4–1b shows a case where the particles are well dispersed but remain poorly distributed. Figures 2.4–1c and 2.4–1d show systems having good distribution, but differing in their dispersion. In general, it is difficult to achieve a good dispersion of CNTs due to their large surface area; however, there are techniques available to break up these aggregates. Some of these techniques include ball milling,[33,40] high shear mixing,[33,43-45] and ultrasonication.[46-49] In this dissertation, I formed a dispersion of the SWCNTs in isopropyl alcohol (IPA) that was then applied to IM7 to generate the IM7/SWCNT composites described in this thesis. Ultrasonication was used to disperse the CNTs in the IPA4.

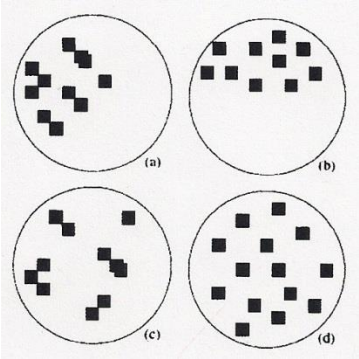

Figure 2.4–1. Illustration from Reference 33 of (a) poor distribution and poor dispersion, (b) poor distribution but good dispersion, (c) good distribution but poor dispersion and (d) good distribution and good dispersion.

Ultrasonication is one of many tools that can be used to break up CNT aggregates into finer structures for use in solution processing. The sonication of nanotubes in a solvent involves exciting the solvent at a fixed energy rate to break up the nanotube bundles through acoustic cavitation. This action causes microscopic bubbles that expand during the negative pressure and results in energy being released at the focus point yielding powerful shearing action. This procedure takes microseconds and the amounts of bubbles are minimal; however, the energy required is exceptionally high. Several investigations have been done on the effects of sonication energy, ultrasonic frequency, time, and the effects of liquid properties for production and CNT dispersions.[42-45]

A suitable method for fabricating polymer nanotube composites has been to disperse the nanotubes and polymer in an applicable solvent before evaporating the solvent to form a composite film. It should be noted that this method relies on the effective dispersion of nanotubes in the solvent and the ability to completely evaporate the solvent. Lau et al. evaluated the role of solvent for nanotube dispersion on the mechanical and thermal properties

of SWCNT bundle reinforced epoxy composites.[54] The SWCNTs were dispersed using various solvents and incorporated into an epoxy matrix with sonication. Differential scanning calorimetry (DSC) results indicated that even small traces of residual solvent in the composite processing had a great impact on the cure reaction.[54] The thermal and mechanical properties of CNTs were also found to be related to the boiling point of the solvent used.[54] Using ultrasonication in toluene, Safadi et al. also uniformly dispersed MWCNTs to incorporate them into composites without the need for any chemical pretreatment.[55] The MWCNTs in their dispersions were found to align at the different shear rates that were generated by their employed spin casting process.[55] Isopropyl alcohol was chosen for the present investigation as other researchers have used this solvent successfully to disperse their CNTs,[33-34] it is readily available, and its use poses a low safety risk in the laboratory.

2.5 PREPREG COMPOSITES

Prepregs (also known as pre-impregnation) are fiber-reinforced resins that cure under heat to form exceptionally strong yet lightweight components.[56] The role of the thermoset resin in the prepreg is to support and bond the fibers together in the composite material so to maintain their position and orientation in the final cured form.

The thermoset cure mechanism and the role of the components used to prepare a matrix are represented below. As an example, the cure can include pre-polymers with multiple epoxy groups whose reactive sites join together and form chains and crosslinks (Figure 2.5–1). In practice, the system may include a number of constituents, and the overall cure process can be complex. When this process is complete, a fully cured polymer is produced.

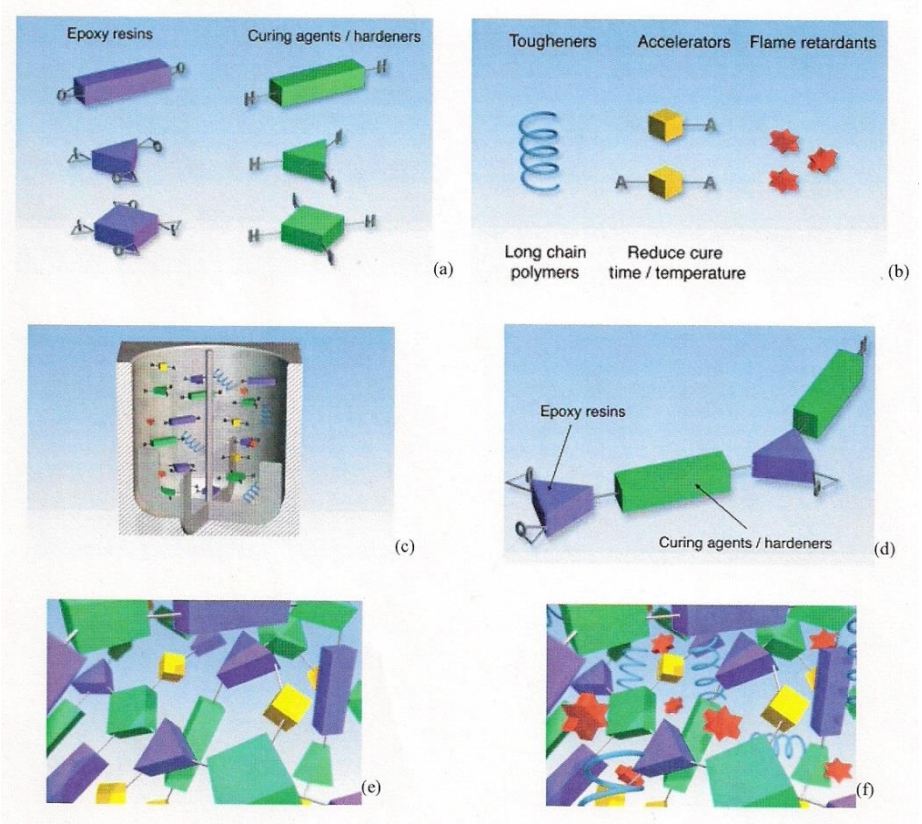

Figure 2.5–1. Curing process for a thermoset resin. (a) Reactive components. (b) Additives (may be reactive or inert). (c) Components are mixed together. (d) Chemical reaction links the components. (e) As a 3D network forms, the matrix gels and then hardens. (f) Additives localize within the 3D network. This figure was taken from Reference 56.

Special tooling is needed to lay up the prepregs into components. Tool design plays an important role in this process. As an example, Hexcel has designed a simple, stable tool (Figure 2.5–2) that can apply uniform pressures to the composite plies and maintain their position during the curing process. During the cure, the temperature is ramped up and held isothermally for a certain period of time where the composites are ramped at finite temperatures until the cure cycle is completed. This technique is called press-cured and is used to release any thermal and/or mechanical stresses in the composite. An example of a rolled prepreg composite is shown in Figure 2.5–3.

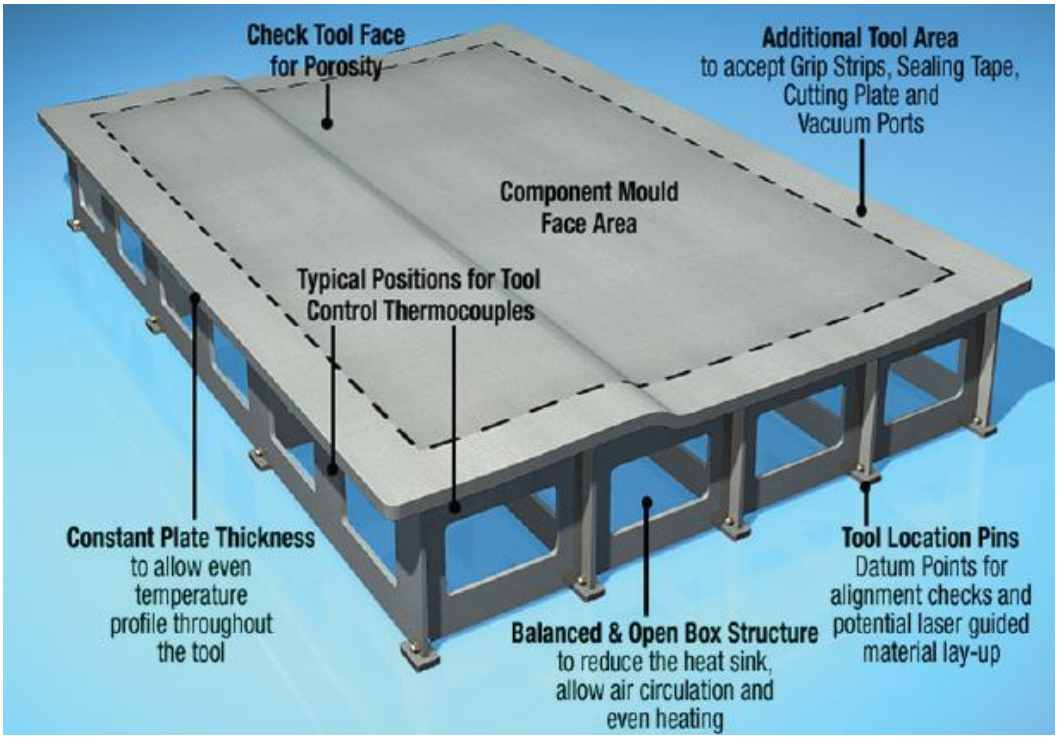

Figure 2.5–2. A tool design used at Hexcel. This figure is taken from Reference 56.

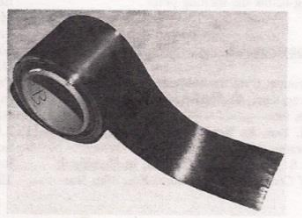

Figure 2.5–3. Photo of a spool of graphite-epoxy tape taken from Reference 5.

In this study, a hand lay-up was used. This manual/non-automated lay-up process has been used for preparing many types of fiber-reinforced prepregs (glass, carbon, kevlar) containing unidirectional and woven reinforcements of various widths.[56]

The type of prepreg composite used in this dissertation was a polyacrylonitrile (PAN) thermoset resin composite impregnated with IM7 carbon fibers that provide it with exceptional

mechanical properties.[56] This type of prepreg composite was chosen for this investigation because many structures such as airplanes to satellites make use of these types of composites. The ability to improve the thermal properties of this composite material would allow their potential replacement of metallic alloys that are used for their combination of favorable structural and thermal properties.

Within the prepreg, the IM7 fibers provide the composites with high tensile strength, modulus, and shear strength, and allow structural designers to achieve higher safety margins for stiffness and strength for critical applications.[56] A major drawback of composite fibers for broader applications is their low thermal properties as there is a trade-off between having good thermal properties and weak mechanical properties. For many heat transfer applications, improvements in the thermal properties of a composite are highly desired even with some loss in their mechanical properties. This dissertation focuses on the effects that the addition of SWCNTs have on thermal properties of an IM7 prepreg composite (specifically on IM7-8552-1).

With regard to the thermal properties of the IM7 prepreg composite, it is an anisotropic material obtained as sheets and has different thermal properties along the in-plane (3.36 W/m–K) and through-thickness (0.62 W/m–K) directions. This composite contains carbon fibers that are oriented with their long axes in directions parallel to the surface of the sheets. The higher value for the composite's in-plane thermal properties reflect that energy can be transferred along the impregnated fibers more easily than from fiber to fiber or through the surrounding material. The observed result is that heat transfer is more rapid in the directions parallel to the surfaces of the composite sheets (i.e., in-plane) than in the direction perpendicular (i.e., through-thickness) to the sheet surface. For the SWCNT-containing composites, both the in-plane and through-plane thermal conductivities are of interest;

however, only the latter were accessible experimentally by available instrumentation. As a result, the in-plane thermal conductivities for the SWCNT-containing composites were instead estimated using a model whereby the thermal conductivity values for the SWCNTs and the in-plane properties for IM7 are used along with structural information about the content and distribution for the added SWCNTs. The theoretical basis for this approach is detailed in Section 5.1. The supporting measurements of the SWCNT content and of the through-thickness thermal measurements used to infer the SWCNT distribution for these calculations are provided in Chapter 4.

CHAPTER III

EXPERIMENTAL METHODS FOR TESTING SWCNTS AND SWCNT/POLYMER NANOCOMPOSITES

3.1 RAMAN SPECTROSCOPY

Raman spectroscopy provides a useful characterization tool for carbon-based materials, showing different characteristic spectral features for sp^3, sp^2, and sp carbons, as well as for disordered sp^2 carbons, fullerenes, and CNTs.[32] All carbon forms in a structure contribute to the Raman spectra in the range of 1000 to 1700 cm^{-1}. The spectra for carbon nanotubes exhibit a two-banded feature in this region with peaks at ~1300 cm^{-1} (*D*-band) and ~1600 cm^{-1} (*G*-band).[33] The G band is a tangential shear feature resulting from graphitic carbon atoms in the nanotubes.[35] The D-band is derived from defects in the carbon network that cause elastic scattering in order to conserve momentum.[35] These D-band defects are due to phonon-defect scattering which yields two Raman peaks of slightly different energies (Figure 3.1–1).[35] Together, the relative intensities for the G and D bands allow evaluation of the amorphous components or defects present within a carbon nanotube sample for assessing sample purity. From Raman spectra, the quality of CNTs can be measured by comparing the D to G band intensity or the D to G' (~2500 cm^{-1}) intensity.[35] If the ratio between the G and D bands is greater than 9:1, the spectra indicate high purity CNTs. Changes in the D-band and G' band Raman spectra can be used for materials characterization and to monitor structural modifications to the nanotube sidewalls that come from the introduction of defects (i.e. by sonication) or by the attachment of different chemical species, (i.e., via functionalization).[34-39]

The positions of the radial breathing modes (RBMs) can indicate the presence of carbon nanotubes in a sample as the spectrum for graphite does not show these spectral absorptions.[35] The RBM absorption frequencies occur between 120 and 350 cm^{-1} for SWCNTs corresponding to diameters between 0.7 and 2 nm, where the frequency of this feature is inversely proportional to the tube diameter.[33] Good quality SWCNTs generally contain minimal defects and exhibit absorption frequencies for the RBMs that correlate to these smaller diameters. Moreover, if the SWCNTs have a high density of defects (i.e., are of bad quality), the RBM absorption frequencies will correlate to structures with larger diameters, where such sizes can suggest a low content of SWCNTs and instead the presence of larger double-walled or multi-walled CNTs.

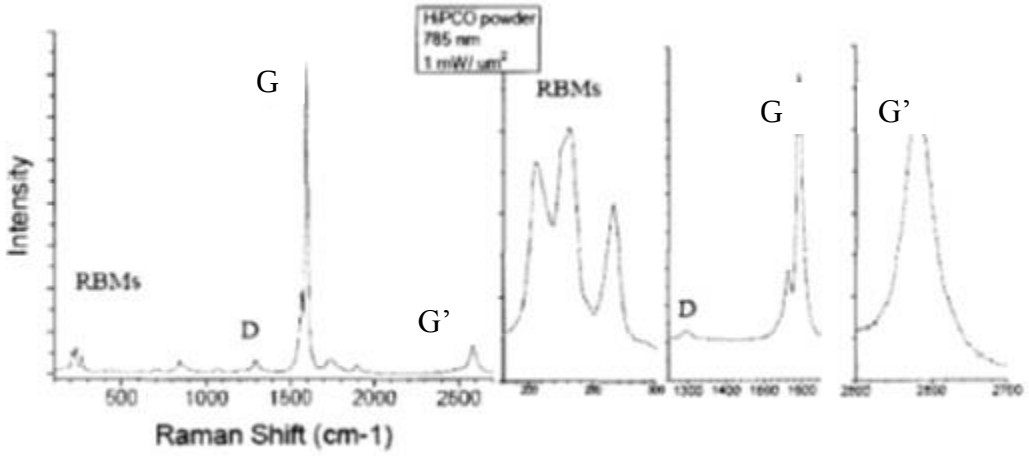

Figure 3.1–1. Raman spectra of CNTs from Reference 34.

3.2 THERMOGRAVIMETRIC ANALYSIS

Thermogravimetric analysis (TGA) is an experimental technique that measures the weight changes that occur as a specimen is heated. This method can be used to determine the thermal stability of a material as well as the presence of volatile components in a sample. TGA can be also used to measure the purity of SWCNTs, DWCNTs, and MWCNTs as these materials undergo complete loss at elevated temperatures. Figure 3.2–1 shows TGA curves for three types of unpurified SWCNTs through the same heating profile. As these scans show, the SWCNTs are burned away and those with greater impurity content leave behind more residual material and exhibit lesser changes in mass.[35]

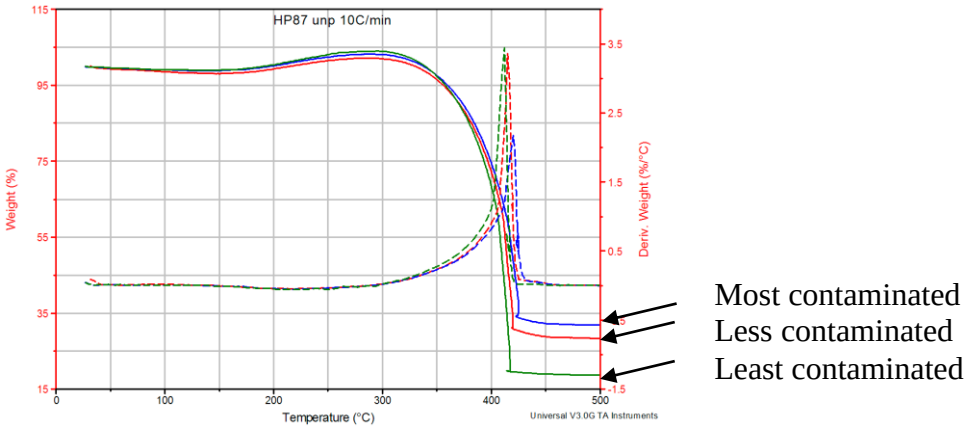

Figure 3.2–1. TGA profiles for three SWCNT materials of differing purities.[35] The heating rate was 10 °C/min in air. The lesser drops in weight correspond to the specimens that contained greater contaminant amounts. Differential traces are also included in the figure.

3.3 DIFFERENTIAL SCANNING CALORIMETRY

Differential scanning calorimetry (DSC) is the most widely used of the thermal analysis techniques.[29] DSC is a well-established measuring technique that is used broadly in many areas of research, development, and quality inspection and testing.[29] By performing DSC over a large temperature range, thermal effects can be quickly identified. The relevant temperatures and the characteristic caloric values can be determined using substance quantities of only a few mg.[29] The measured properties by DSC include heat capacities, heats of transitions, kinetic data, sample purity, and temperatures of glass transitions.[29] DSC serves in the following capabilities: identifying substances, measuring phase diagrams, and determining the degrees of crystallinity.

DSC is performed by an instrument that measures the temperature difference between the sample and a reference specimen as a function of temperature and time.[29] DSC has advantages compared to conventional calorimetry in that its dynamic mode of operation ("scanning") allows reactions or processes to be investigated that can be thermally activated, and has high sensitivity to anomalies of the temperature-time function.[29]

The specific heat (C_p) can be measured two ways by DSC. The traditional measurement of C_p, as outlined in ASTM E1269, requires three separate experiments for baseline, calibration, and sample analysis.[87] An alternative method is a modulated DSC® (MDSC) experiment, where modulation of the sample temperature permits the heat flow to be split into two components, one thermodynamic that is dependent upon the sample's C_p and the other kinetic reflecting nonreversible changes to material.[87] In a further refinement, developers have provided an approach for determining C_p in a single run by measuring the reversing heat capacity.[88] This method is more precise and reproducible and validates C_p faster in a DSC

single-run approach than the ASTM E1239 approach.[88] Add comment on which approach you will use. Which method is used for the DSC studies detailed below? Some case studies on the use of DSC for probing the thermal properties of CNT-containing materials are presented below.

Kappagantula et al. used DSC to measure the thermal transport properties of aluminum-polytetrafluoroethylene nanocomposites that contained various graphene and carbon nanotube additives.[30] Their results showed that the addition of graphene had the greatest influence on improving the composite's thermophysical properties. For instance, the thermal conductivity of the composites containing 10% graphene increased by 98%.[30] Graphene similarly enhanced the thermal diffusivity and specific heat of the Al/Teflon matrix. In contrast, on a per gram basis, the addition of nano-carbon and carbon nanotubes to the composites decreased the thermal conductivity and thermal diffusivity of the samples.[30] Kappagantula et al. offered explanations ranging from the lack of orientation of the CNTs in the polymer to a lack of uniformity for the dispersed additives in the matrix.

In another relevant study using DSC, Evseeva et al. examined the influence of the concentration of carbon nanotubes in an epoxy/CNT nanocomposite on its thermophysical properties at low temperatures.[31] They varied the concentrations of SWCNTs and MWCNTs from 0.1 to 1.0 wt% in the composites and characterized their thermal properties at temperatures from -150 to 150 °C.[31] Figure 3.3–1 shows the temperature dependence for the specific heat of various epoxy nanocomposites with different additives over the temperature range of -150 to 150 °C.[31] At temperatures below 25 °C, C_p values for the nanocomposites were roughly the same as the native epoxy resins within experimental error.[31] This lack of difference is not surprising given the low loading levels of the additives and the similar C_p values for the additives and the epoxy resins over the explored temperature range.[31]

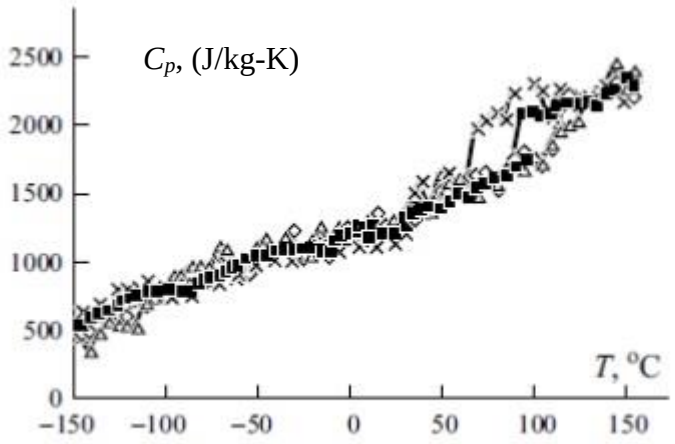

Figure 3.3–1. Specific heats (C_p) of various epoxy nanocomposites with 0.1 wt% loadings of additive as affected by temperature *T*. Additives include MWCNT (◊); SWCNT (X); an aerosol resin (Δ) and a ■ – native epoxy resin. From Reference 31.

Evseeva et al. also examined the effect of additive concentration on the thermal properties of the epoxy nanocomposites. Figure 3.3–2 shows the effect of temperature on the specific heats of various SWCNT-epoxy nanocomposites over the temperature range of -150 to 150 °C.[31] The sample differed in their loading levels of the SWCNTs. For temperatures below 25 °C, the C_p values for the nanocomposites and the epoxy resin were roughly the same within experimental error.[31] The difference observed between 50 – 120 °C maybe due to a change in the glass transition temperature of the epoxy resin by the SWCNTs. With the addition of fillers (nanocomposites) to the epoxy, the epoxy morphology will change resulting in changes to the specific heat of the resin at the higher temperatures. The general trend is that the specific heats of the epoxy resins and the nanocomposites were similar as the investigated SWCNT levels were low (up to 1.0 wt%).[31]

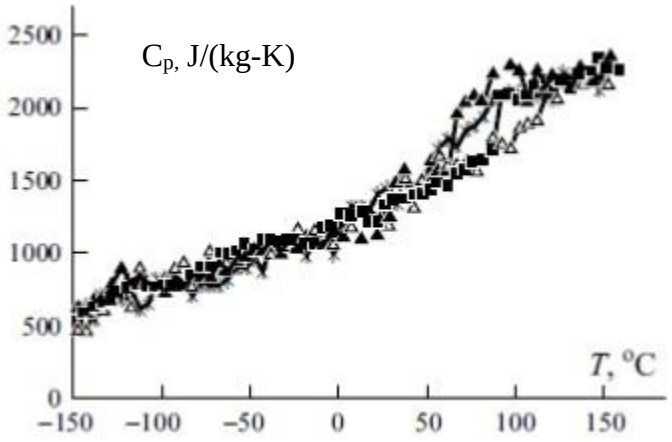

Figure 3.3–2. Specific heats (C_p) of various SWCNT-containing epoxy nanocomposites as affected by temperature T. SWCNT concentrations were 0 (■), 0.1 (▲), 0.5 (X) and 1.0 (Δ) wts%. From Reference 31.

Evseeva et al. performed a similar study on the effects of loading on C_p by adding MWCNTs to the epoxy resin. Figure 3.3–3 illustrates the temperature dependence of C_p for various MWCNT-epoxy nanocomposites over the temperature range of -150 to 150 °C.[31] As with the SWCNTs (Figure 3.3-2), the addition of MWCNTs to the epoxy resin at levels of up to 1 wt % showed no effect on C_p for temperature below ~50 °C. At higher temperature, other effects were noted reflecting changes to transition temperatures for the epoxy resin. Specifically, as the MWCNT concentrations increased, the transition temperatures of both the glass transition state, T_g, and the high-elasticity states decreased significantly.[31] This is most likely due to the fact that MWCNTs have a lower T_g than the epoxy resin; whereas, as you increase the volume fraction of the MWCNTs (adding a filler material to the resin), there will be a noticeable shift in the T_g. At 1.0 wt%, the researchers noticed the largest decrease in T_g,

where T_g for the 1.0 wt% MWCNT sample occurred at 50 °C which is 30 °C lower than for the pure epoxy resin.[31]

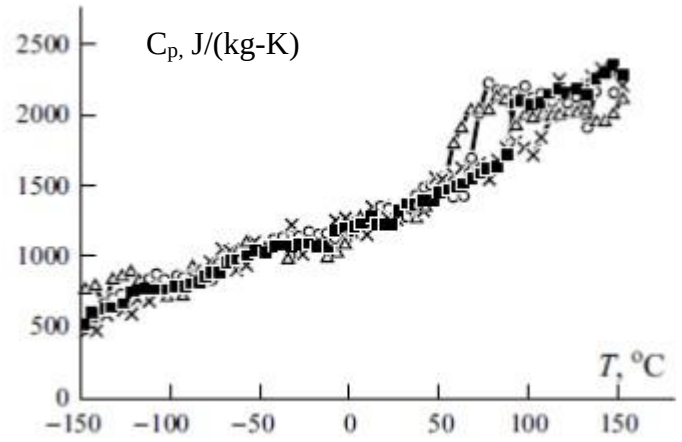

Figure 3.3–3. Specific heats (C_p) of various MWCNT-containing epoxy nanocomposites as affected by temperature T. MWCNT concentrations were 0 (■), 0.1 (X), 0.5 (○), and 1.0 (Δ) wt%. From Reference 31.

The changes to T_g by the addition of MWCNTs were greater than for the addition of SWCNTs. The MWCNTs have a higher density and a smaller surface area than the SWCNTs and these factors affect the interfacial surface between the nanofillers, the binders, and the CNTs. These interactions are greater in the SWCNT composite structure than the MWCNT composite at the same loading concentration.[31] In short, the influence of interfacial interaction is more pronounced at small filler concentrations in the composite with SWCNTs.[31] The total effect of the restricted molecular mobility in the boundary layer decreased the packing density of the macromolecules; whereas, lowering the packing density of the macromolecules in the

boundary layers of the polymer matrix and filler increased the mobility of the polymer macromolecules and overall decreased the T_g.[31]

3.4 THERMAL DIFFUSIVITY

The thermal diffusivity, α, of a material is defined as its thermal conductivity divided by the product of its density and heat capacity per unit mass ($\frac{\lambda}{\rho * C_p}$).[21] In this definition, the thermal conductivity, λ, of a material is a measure of the steady-state heat flow rate through a unit thickness of an infinite slab of homogeneous material in a direction perpendicular to its surface, as induced by a unit temperature difference.[21] This property is identified at a specific mean temperature, since it varies with temperature.[21]

The flash technique has become a standard testing method for thermal diffusivity. The original model for the flash method to measure the thermal diffusivity of a material was first introduced by Carslaw and Yeager.[22-23] Their original equation can be reduced for assumptions of a homogeneous specimen, one-dimensional conduction, an impulse input, adiabatic boundaries and isothermal conditions to yield a simple relation:[23]

$$\alpha = \frac{0.13879 \cdot L^2}{t_{1/2}} \frac{cm^2}{s} \quad (1)$$

where L is the thickness for a one-dimensional heat transfer, and $t_{1/2}$ is the time to half-maximum rise.[21]

In the flash technique, the sample as a circular disk of a known thickness (typically ranging between 1 and 6 mm) is used.[21] A laser pulse provides a short burst of energy to the

front face of the sample as shown in Figure 3.4–1.[21] A detector is used to record the initial temperature of the rear face of the sample and its changes as a function of time.[21] Typical temporal changes of ~3°C are used to determine a "half-max-time" that is used for calculating a thermal diffusivity (Figure 3.4–2).[21] It is common practice to coat the front and rear faces of the specimens with a conducting layer of graphite or silver paste to ensure that the energy pulse is absorbed at the surface.[24]

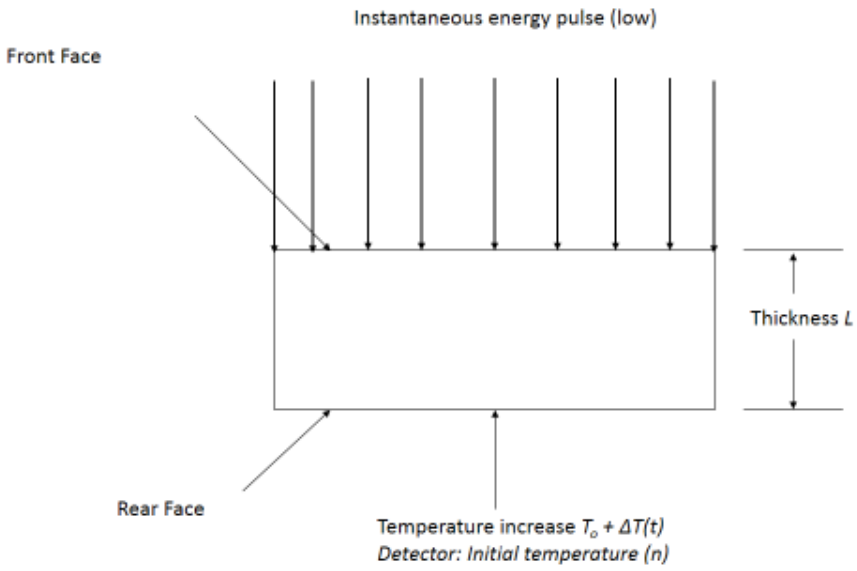

Figure 3.4–1. Specimen schematic of the flash method. Taken from Reference 21.

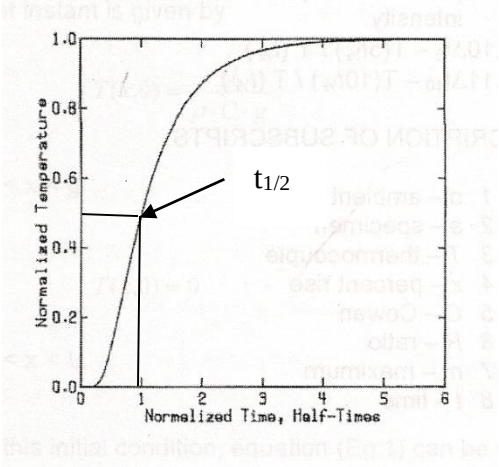

Figure 3.4–2. Characteristic thermogram for the flash method from Reference 21.

For materials that are highly conductive and unavailable as thick samples, an in-plane (parallel to the contact surface) method is used. Here, energy is deposited at one spot of a specimen to generate a changing temperature profile along the surface.[25] This method can yield complex heat flow patterns in the sample that can lead to uncertainties of about ~10% in such measurements.[25] To provide better control, the pulse is deposited in a ring-shaped area on one side of a sample and the measurement is made on the opposite side at the center of the ring.[25] Here, the heat flow penetrates the thickness of the sample and must progress radially in a cylindrical volume towards the center of the specimen.[25] Due to quasi-focusing of the heat wave on the center point, the signal is stronger than from a linear heat path.[25] Further, the heat flows away from the outer perimeter of the ring and acts as a shield for the area of interest from outside effects.[25] In-plane techniques are often done at room temperature to minimize the development of further complexities to the heat flow patterns by external influences.

Various in-plane and through-thickness techniques have been used to determine the thermal diffusivity of many highly conductive nanocomposite materials. Veca et al. fabricated graphite into nano-sized carbon structures that were used as fillers in polymeric epoxy

nanocomposites to achieve ultrahigh thermal conductivites.[26] For their samples, they used sequential alcohol and oxidative acid treatments and characterized the nanocomposites with transmission electron microscopy, Raman spectroscopy, and x-ray diffraction. The thermal diffusivity for films of blank epoxy was 0.12 mm^2/s.[26-28] For comparison, by varying the volume fractions of the carbon nanosheets in the polymeric nanocomposite, they produced films that exhibited in-plane thermal diffusivities of as high as 20 - 35 mm^2/s by incorporating approximately 40% CNTs to their epoxy.[26]

Krapez et al. performed related in-plane and through-thickness measurements on non-homogeneous slabs of carbon/carbon-silicon carbide (C/C-SiC) tensile composite materials.[27] When they applied a thermal pulse, they measured the ratio of the Fourier transform of the temperature at two different spatial frequencies and obtained an exponential function that could be characterized in the parallel or perpendicular directions. They also observed that when the C/C-SiC stresses increased, the in-plane thermal diffusivity decreased linearly. Their results correlate with the fact that for certain ceramic matrix composite materials, the density of small cracks progressively increases with stress until failure.

Zamel et al. investigated the in-plane thermal diffusivity of carbon paper with the addition of Teflon.[28] For their samples, Teflon loadings were chosen to comprehensively understand the effects of temperature on thermal conductivity. The materials were investigated for use as polymer electrolyte membranes within fuel cells and must operate under various thermal conditions. For all specimens, they observed that their thermal properties decreased with increasing temperature. Further, the addition of as little as 0.5 wt% Teflon to the carbon paper resulted in a decrease in the thermal conductivity of the specimens. With the added Teflon, the thermal conductivity for these samples decreased from 12.5 ± 0.9 W/m-K for the virgin material to 10.6 ± 0.7 W/m–K for the 0.5 wt% material.

For CNTs, their in-plane and through-thickness thermal diffusivities change little with temperature. In research done by Mäklin et al., they performed thermal diffusivity experiments on aligned multi-walled carbon nanotubes using the previously mentioned flash method.[80] In their work, they measured the thermal diffusivities of as-grown and annealed MWCNTs between 25 and 200 °C. The CNTs exhibit lower thermal diffusivities for their annealed MWCNTs than for their as-grown MWCNTs (Figure 3.4–3), and showed slightly lower thermal diffusivities at higher temperatures. With annealing, the thermal diffusivity values decreased to about half of their values measured before annealing (from ~0.45 to ~0.22 cm^2/s). Notably, the thermal diffusivities of both the as-grown and annealed MWCNTs were lower than for aluminum alloy (~0.6 cm^2/s) and copper (~1.1 – 0.9 cm^2/s) samples tested over the explored temperature range. In short, their study showed that the thermal diffusivities for MWCNTs can be influence by processing conditions; however, their thermal diffusivity values are relatively constant throughout their explored temperature range.

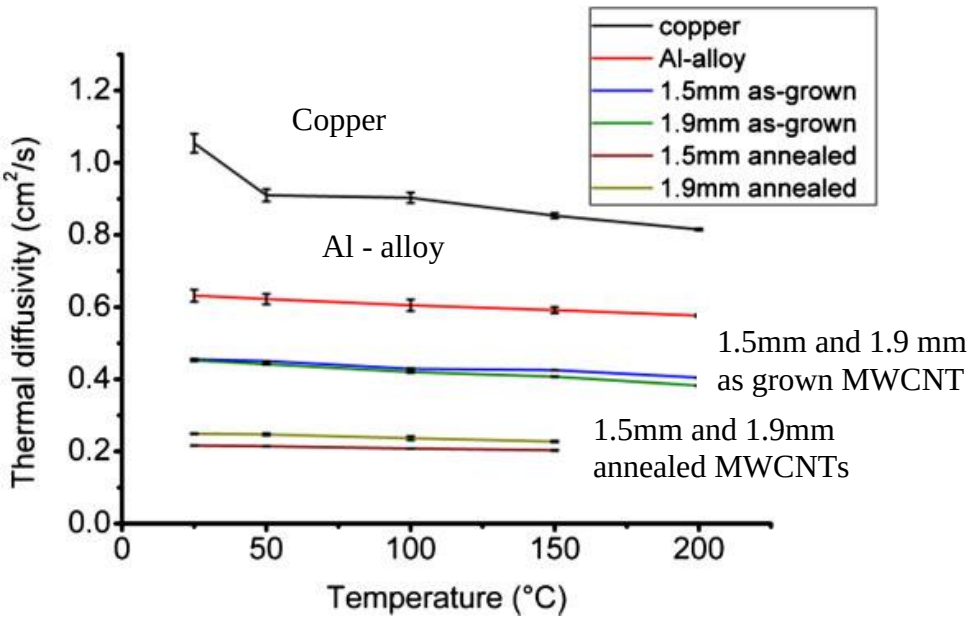

Figure 3.4–3. Thermal diffusivities of as-grown MWCNTs, annealed MWCNTs, and reference copper and aluminum alloy specimens between 25 and 200 °C from Reference 80.

The thermal conductivity of a SWCNT sample can depend on the degree to which the direction of measurement matches the orientation of the SWCNTs. As an example, Figure 3.4-4 from Han et al. shows the difference that SWCNT alignment has on thermal conductivity.[81] In their work, these authors measured the thermal conductivities of free-standing networks of aligned and randomly oriented SWCNTs from 10 to 400 K. For the aligned networks, the thermal measurements were made in the direction of SWCNT orientation. For both the aligned and randomly oriented samples, thermal conductivity increased with increasing temperatures; however, they observed that the thermal conductivities for the aligned SWCNTs were ~10 times greater than for randomly oriented SWCNTs (Figure 3.4–4) at all temperatures. These higher conductivity values highlight the level of improved thermal transfer that can be gained by controlling the local microstructure of the SWCNT additives. For comparison, the samples presented in this dissertation contained layers of non-aligned SWCNTs within the

IM7/SWCNT composites. While the added SWCNTs produced improvements in thermal conductivity to the IM7, additional gains beyond those observed in this work are likely possible by aligning the SWCNTs in a direction of interest within these samples. Such experiments could be a direction for future work.

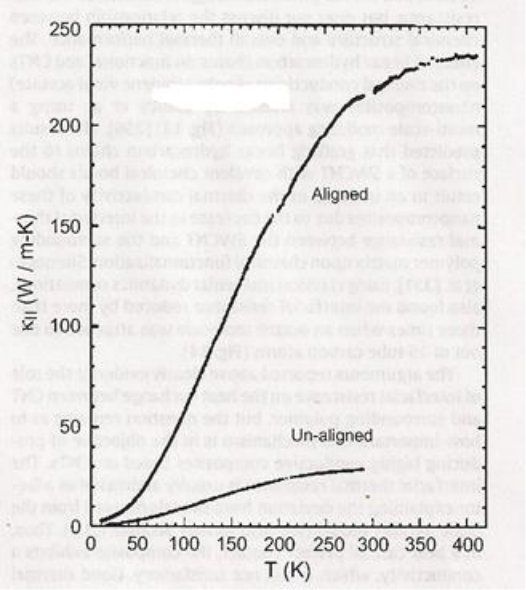

Figure 3.4–4. In-plane thermal conductivities of 5 μm "thick" annealed samples of aligned and un-aligned SWCNTs measured by Han et al.[81]

The effect of the mixing SWCNTs into a pre-preg composite was investigated by Yoo et al. In their work, they air-sprayed SWCNT that had been functionalized with carboxylic acids on their surface onto IM7-977 prepreg composites.[82] The employed IM7-977 resin system is a PAN thermoset resins that is related to the IM7-8552-1 pre-preg used in this dissertation, but having a lower density (1310 kg/m^3), different woven patterns, and requiring different conditions for curing.[86] In using their air-spraying method, Yoo et al. found that the

SWCNTs formed thin bands between the carbon fiber layers and did not infiltrate deep into the composite plies due to the low resin flow during cure.[82] Table 3.4–2 provides the C_p, through-thickness thermal diffusivity, and thermal conductivity data for their 0, 1, and 2 wt% SWCNT specimens. From these results, Yoo et al. concluded that there was no significant increase in the through-thickness thermal conductivity measurement by the addition of SWCNTs at these loadings. However, in my experiments, an increase in the thermal conductivity of ~20 to 30% is demonstrated using my spray method by using higher loadings. The C_p of CNTs used Yoo's experiments were similar to those (within experimental error) for the SWCNTs added to my samples. In contrast to the work by Yoo et al., my approach using a related air spraying method was able to improve the through-thickness thermal conductivity of hybrid composites by achieving higher SWCNTs loadings.

Table 3.4–1. capacities, through-thickness thermal diffusivities, and through-thickness thermal conductivities of SWCNT/IM7-977 prepreg composites from reference 82.

SWCNT wt%	C_p (J/kg-K)	Thermal Diffusivity (mm^2/s)	Thermal Conductivity (W/m-K)
0	942	0.476	0.701
1.0	942	0.469	0.682
2.0	942	0.488	0.704

3.5 MODELING OF THE THERMAL PROPERTIES OF CARBON NANOTUBE-POLYMER COMPOSITES

Many researchers have attempted to model the thermal properties of composites and CNT/polymer composites. Zhou et al. were able to measure and model the enhancements to the thermal conductivity of natural flake graphite/polymer (NFG/polymer) composite sheets caused by adding carbon black, CNTs, and graphene as nano-fillers.[58] Zhou et al. reported an improvement of thermal conductivities of up to 24% by the addition of CNTs at 10 wt% and of 31% by the addition of graphene at 10 wt%. They were able to model this improvement based on a bridging mechanism of the thermal contacts between the composite and the additives.

Lee et al. modeled the thermal conductivities of short fiber composites in the in-plane (parallel) and through-thickness (perpendicular) directions with the use of models designed by Benveniste and Miloh and Eshelby.[59] Their model consisted of changing the short fiber composites to shapes such as spheres and continuous fibers by changing the confocality variable. The confocality variable is a special variable that allowed the authors to change the theoretical parameters from small composite fibers into spheres. Making modifications to this parameter, they were able to correlate their predictions to experimental results in the literature on the effects of fiber aspect ratio and fiber volume fractions on thermal conductivity.

Wang et al. modeled the enhancement of the thermal conductivity in carbon fiber-in-polymer composites using a three-dimensional numerical method.[60] Their model agreed well with experimental data from the literature. They claimed that their method does not depend on determining empirical parameters (e.g. temperature, steady state heat flux, cross-sectional area, length of the carbon fibers and the thermal conductivity) on a case-by-case basis. Instead,

users of this method can design and optimize their properties with respect to the fiber aspect ratio, orientation angle, and volume fraction on the thermal conductivity of polymer composites.

Grujicic et al. modeled the experimental data for carbon-CNT constituent materials using a three-dimensional stationary heat-transfer finite element analysis that computed the average in-plane (parallel) and through-thickness (perpendicular) thermal conductivities in carbon-carbon composites.[61] At room temperature, their predictions correlated well with the results from literature experimental results where variations in fiber aspect ratio and fiber volume fractions affected thermal conductivity. They also claimed that at high temperatures, their model predicts the extent that contributions to the gas-phase conduction and radiation within the microstructural defects can increase the in-plane (parallel) thermal conductivity in composites.

In the research detailed in this dissertation, I performed a 3D finite element analysis of a layered composite structure with thermal properties as specified from the experimental results. The model consisted of hex elements (6-sided blocks, i.e. cubes) that each locally had properties consistent with the hybrid composites that were fabricated. In these structures, the carbon nanotube layers were assumed to have isotropic properties while the IM7 layers had non-isotropic properties to account for the differences in conductivity in the lateral (parallel) and through-thickness (perpendicular) directions. In Chapter 5, the simulations had heat loads applied to opposing sides of the composite to examine the temperature distributions and flow of heat through the structure. The results from this simulation are compared to the related case lacking the addition of the SWCNTs.

In addition to the above mentioned finite element analysis, a model was developed to describe the competing influences of the components in the composite using a combination of

series (through-thickness) and parallel (in-plane) resistances for the SWCNT and the IM7 composite regions in a ply. The predictions of this model are tested in Chapter 5 against the experimental results presented in Chapter 4.

CHAPTER IV

PROPERTIES OF CARBON NANOTUBE-POLYMER COMPOSITES

4.1 SWCNT CHARACTERIZATION

SWCNTs were obtained and used as received from US Research Nanomaterials, Inc. (Houston TX). The SWCNT were characterized by thermogravimetric analysis (TGA), Raman spectroscopy, and differential scanning calorimetry (DSC) to confirm their integrity before use in composites.

TGA is an analytical technique used to determine a material's thermal stability and its volatile content by monitoring the weight change that occurs as a specimen is heated. TGA can be used to test the purity of SWCNTs. As shown in Figure 4.1–1, the SWCNTs obtained from US Research Nanomaterials, Inc. exhibited a TGA profile that was consistent with that reported by Chiang et al. for highly pure SWCNT specimens.[62,85] In preparing their SWCNTs, Chiang et al. used a high pressure carbon monoxide (HIPco) process that produced ~1 nm diameter size nanotubes.[85] The SWCNTs obtained from US Research Nanomaterials, Inc. showed a temperature range between 400 °C – 600 °C where weight loss occurred, similar to that observed by Chiang et al. for their SWCNTs (Figure 4.1–1). Based on the similarity in their TGA behavior, I concluded that the SWCNTs obtained from US Research Nanomaterials were of high quality and appropriate purity for my composite experiments.

(a)

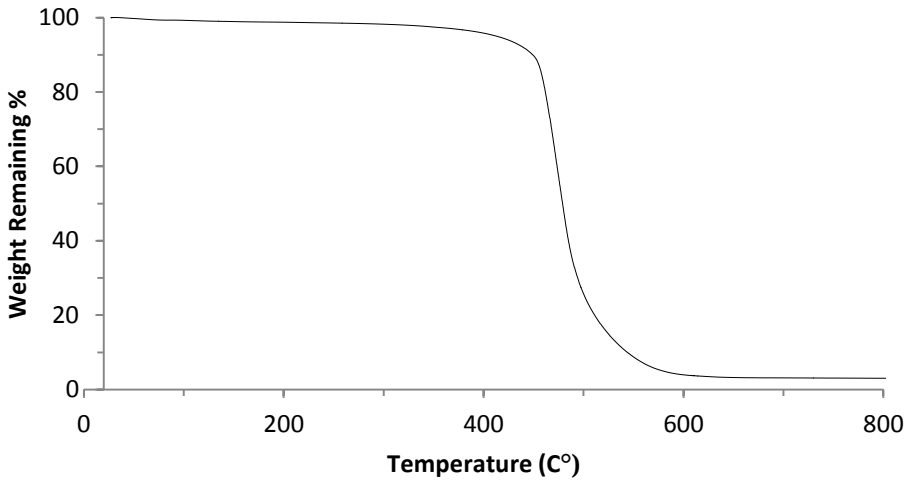

(b)

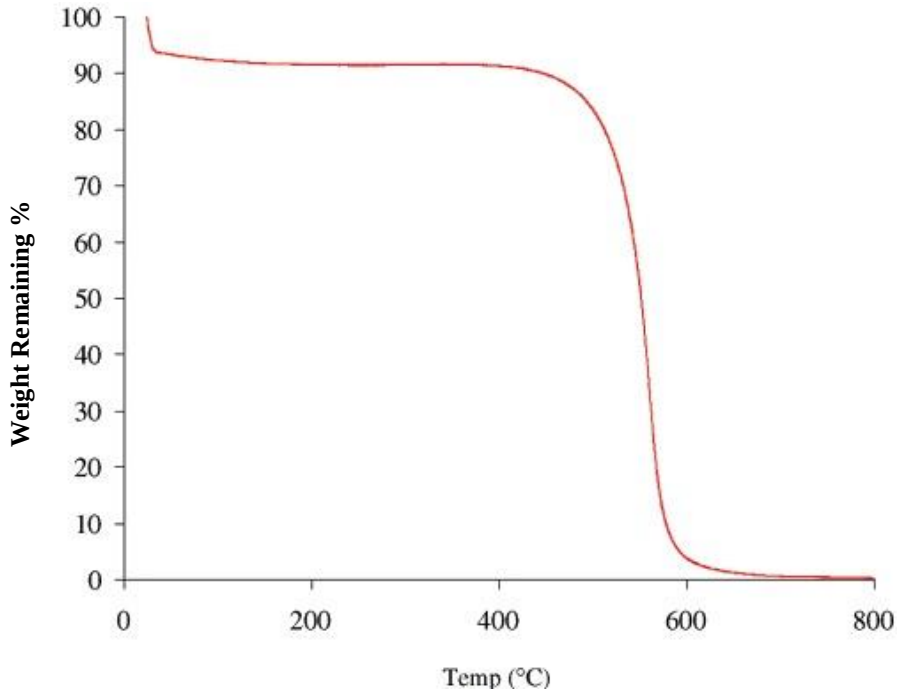

Figure 4.1–1. (a) TGA of US Research Nanomaterials, Inc. SWCNTs. (b) TGA reported by Chiang et al. of SWCNTs prepared using a high pressure carbon monoxide disproportionation (HiPco) process. SWCNTs were heated in air to 800 °C at 5 °C/min .[85]

Raman spectroscopy is a non-destructive method commonly used to investigate CNTs.[53,63-78] Figure 4.1–2 shows a Raman spectrum obtained from the SWCNTs used in this

work. This spectrum shows intensities for the radial breathing modes (RBMs), and the D, G, and G' bands at 200, 1300, 1500, and 3000 cm^{-1}, respectively, that are consistent with the diameter of the nanotubes being between 1.0 and 2.5 nm.[33] For comparison, a Raman spectrum of purified SWCNTs from work by Parás-Peña is shown in Figure 4.1–3.[33] Based on the similarities in the intensity patterns and positions for peaks in the Raman spectra in Figures 4.1–2 and 4.1–3, I concluded that the SWCNTs used in this work had properties consistent with those in the literature.

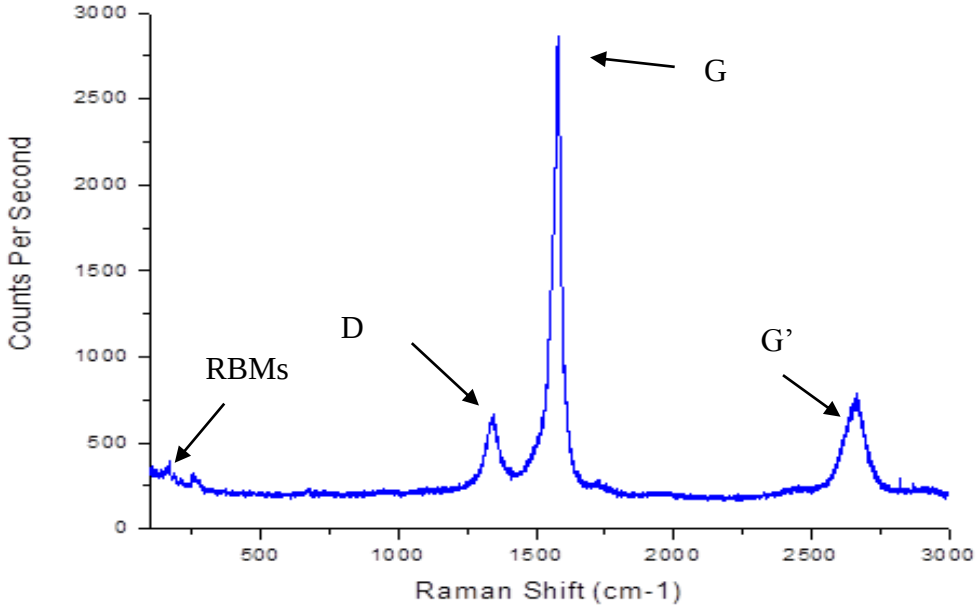

Figure 4.1–2. Raman spectrum of the SWCNTs used in this work.

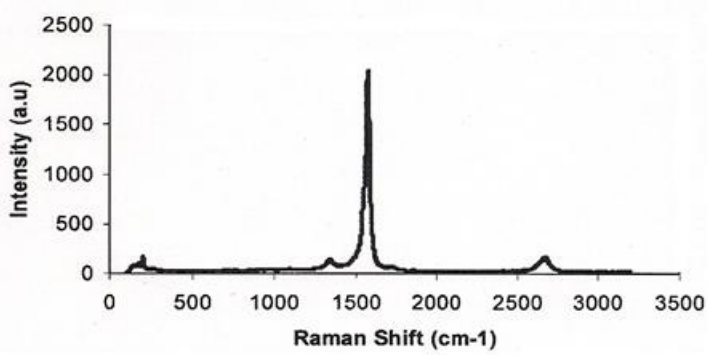

Figure 4.1–3. Raman spectrum of purified SWCNTs obtained by Parás-Peña[33] that is provided for comparison.

4.2 FORMATION OF SWCNT COATINGS ON IM7 PREPREG COMPOSITES

IM7-8552-1 (which throughout this thesis I refer to simply as IM7 for brevity) was obtained as a 12" in wide, 80 pound roll from Hexcel Corporation (Decatur, AL) that was used as received. The IM7 roll was stored in a freezer at -18 °C when not in use to avoid deterioration. Prior to sample preparation, the IM7 prepreg was thawed for 8 hours at room temperature in a sealed polyethylene bag to avoid moisture contamination. The IM7 composite was cut from a roll of material into 12" x 9.5" squares. The plies were a nominal 5 mil (0.005 in) in thickness with a surface roughness of 0.0002 in. Surface roughness denotes that there is a small scale of irregularity (here ~ 4%) in the surface flatness.[57] The mass for each specimen was measured, and the uncoated plies had an average mass of 3.3 mg with a standard deviation of 0.3 mg.

SWCNT dispersions were prepared in isopropyl alcohol (IPA) using a Fisher Scientific 550 Sonic Dismembrator (Figure 4.2–1) that was operated at a fixed energy of 70 kJ with a sonication time of 1 hour that consisted of alternating 10 second on-periods and 10 second off-

periods of sonication. The SWCNT concentrations in the IPA were 0.007, 0.009, 0.02, 0.04, 0.06, 0.08 and 0.1 wt%. The resulting dispersions showed good stability as evidenced by a test where samples of the prepared SWCNT dispersions were left to settle in a test tube for 72 hours and then characterized. It was determined by visual inspection that the SWCNTs stayed in suspension quite well over this length of time. As the spraying of the dispersion onto the IM7 could be completed within 30 minutes of ultrasonication, the compositions of the dispersions could be considered as unchanging during the deposition process.

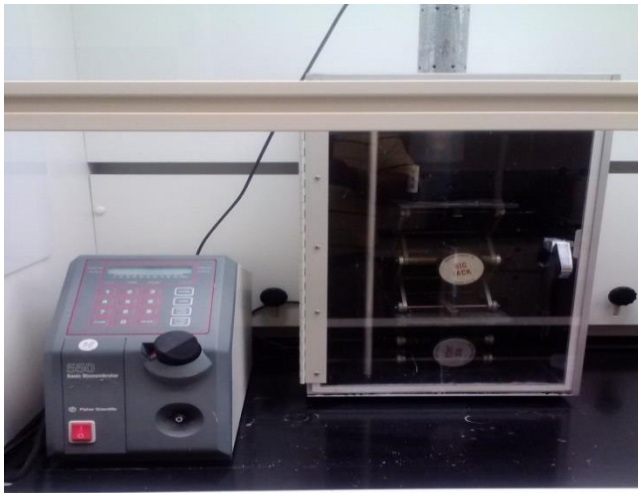
(a)

(b)

Figure 4.2–1. (a) Fisher Scientific 550 Sonic Dismembrator. (b) 0.007 wt% SWCNT dispersion in isopropyl alcohol after sonication.

A goal for the spraying process was that it cast uniform films of the SWCNTs on the IM7 sheets. Regrettably, the morphology of the IM7 and the challenge in distinguishing the coatings from the underlying substrate prevented the use of techniques such as atomic force microscopy (AFM) and profilometry for estimating the thickness, coating uniformity, and consistency of these thin films. As an alternative, I used AFM to characterize a CNT coating

on a substrate (glass) that could allow such morphological information to be obtained. This experiment was pursued with an expectation that similar coatings might form on both IM7 and glass.

In contrast to the appearance of the SWCNT coatings on IM7 (that appeared smooth and uniform as could be discerned by eye), the SWCNT coatings on glass were visually less dispersed (Figure 4.2–2). In this figure, the SWCNTs appear to have coalesced around each other and to not separate well enough to produce a smooth coat on the glass substrate.

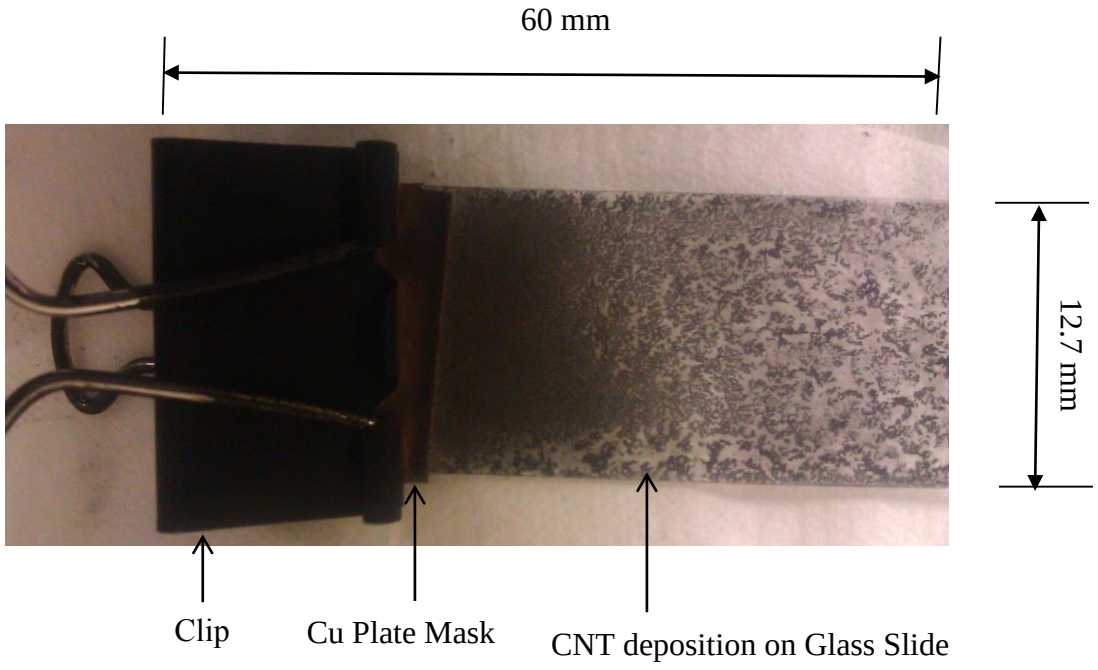

Figure 4.2–2. Optical image of a SWCNT film produced by spraying a 0.1 wt% SWCNT solution in IPA onto a 1” x 3” glass slide.

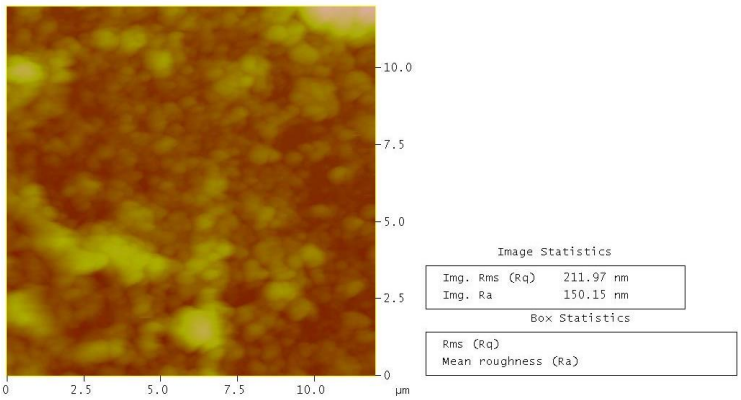

Figure 4.2–3. AFM of a SWCNT film produced from spraying a 0.1 wt% SWCNT solution in IPA onto a glass slide.

I coated the IM7 plies with a thin layer of the SWCNT dispersions in IPA in a spray booth that I constructed in a fume hood. This spray area included a spray stand that held multiple samples of IM7 composite plies (Figure 4.3–4) so that many samples could be obtained in a single run. The plies were suspended vertically and sprayed by a gravity spray gun (Speedaire® Gravity Feed Spray Gun Model 4XP65J as shown in Figure 4.3–5) using argon gas at a pressure of 50 psi. An inert gas was used to avoid oxidation of the SWCNTs during the spray process. Roughly 500 mL of solution was placed in the gravity-fed cup. The spray was conducted manually with a slow pass (~2 seconds per ply) across the IM7 plies. The air control knob was turned to low and the fluid control knob was turned to medium. These conditions delivered the CNT dispersion at the rate of 6 mL/s.


(a)

(b)

Figure 4.2–4. (a) Spray booth. (b) Arrangement of 12” x 9.5” IM7 composite in the fume hood prior to spraying.

Figure 4.2–5. Speedaire® Gravity Feed Spray Gun Model 4XP65J.

The spray gun was held ~ 20 cm away from the work surface. The stroke was started ~10 cm to one side away from the first ply and concluded ~10 cm to the other side past the last ply with a single pass. The length of time it took for the sprayed CNT solutions to dry on the IM7 samples was a few seconds. IPA solutions with varying SWCNT content were used as a way to generate IM7/SWCNT composites with differing SWCNT compositions; however, when applying the SWCNT solution onto the IM7, small amounts of solution dripped off the

composite plies. As a result, the SWCNT composition of the coated IM7 plies couldn't be directly controlled by varying the solution compositions. Measurements of the CNT composition on the plies that are included in Section 4.4 show the general trend that IM7 samples sprayed with IPA dispersions with higher SWCNT content yield greater SWCNT amounts in the as-prepared composite.

4.3 SWCNT-IM7 COMPOSITE LAYUP AND MACHINING

In this study, the IM7 prepreg was processed using a vacuum bag oven process described by Hexcel, Inc.[56] Vacuum bag processing is suited to preparing monolithic components of varying thickness and in large sandwich structures. The technique involves the placing and sealing of a flexible bag over a composite layup and evacuating the air from under the bag. This process is shown in Figure 4.3–1. The consumables needed for this process are listed in Table 4.3–1.

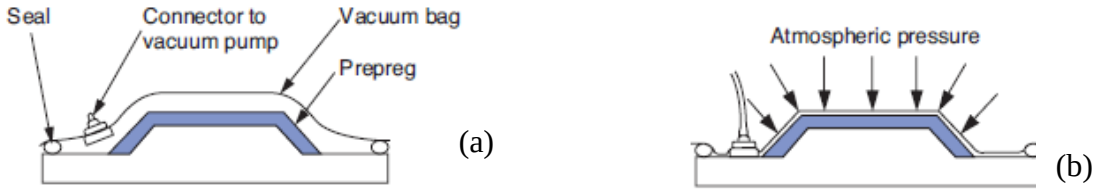

Figure 4.3–1. (a) Sealing flexible bag over layup. (b) Applying vacuum to the system. This figure is taken from Reference 56.

Table 4.3–1. Consumables for vacuum bag processing. This table is from Reference 56.

Release Agent	Allows release of the cured prepreg component from the tool.
Peel Ply	Allows free passage of volatiles and excess matrix during the cure. Can be removed easily after cure to provide a bondable or paintable surface.
Bleeder Fabric	Usually made of felt or glass fabric and absorbs the excess matrix. The matrix flow can be regulated by the quantity of bleeder, to produce composites of known fiber volume.
Release Film	Prevents further flow of matrix and can be slightly porous (with pin pricks) to allow only air and volatiles to pull into the breather layer above.
Breather Fabric	Provides the means to apply the vacuum and remove air and volatiles from the whole assembly. Thicker breathers are needed when high autoclave pressures are used.
Edge Dam	Contains resin flow and component shape.
Vacuum Bag/ Sealant Tape	Provides a sealed bag to allow air removal to form a vacuum in the bag.

The removal of the air forces the bag down onto the layup with a consolidation pressure of up to 1 atmosphere. This process is illustrated in Figure 4.3-1b. The completed assembly, with vacuum still applied, was placed inside an oven or on a heated mold with good air circulation and the composite was produced after a relatively short cure cycle.[56]

The hybrid composite specimens were laid up unidirectionally into 12- and 16-ply structures as shown in Figure 4.3–2. I selected this design so that the composite specimens had sufficient thicknesses for measurements of their thermal properties:

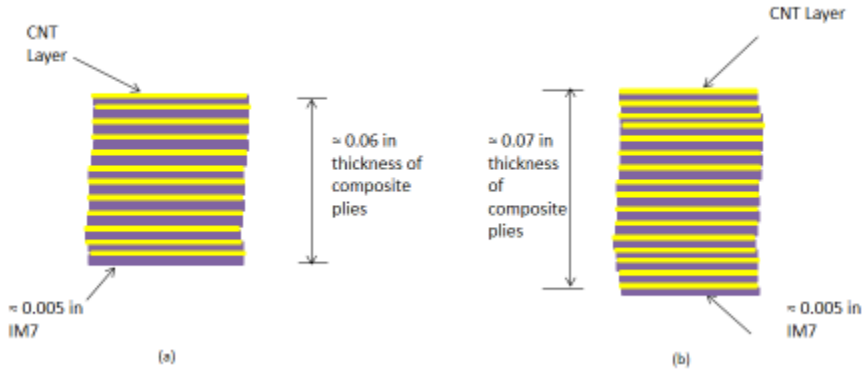

Figure 4.3–2. (a) 12-ply composite layup. (b) 16-ply composite layup.

To prepare a 12-ply specimen, a single ply was laid down on the debulking tool where the ply was compressed to the vacuum table for 5 minutes. Then 6 individual plies were placed on top each other and compressed on the vacuum table for another 5 minutes. Finally, another 5 individual plies were placed on top of the 7 plies and compressed on the vacuum table for 24 hours resulting in a 12-ply layup. To complete a 16-ply specimen, the same process was followed but the layup scheme was: 1-ply, 6-plies, 6-plies, and 3-plies. Laying plies down in such a stepwise process is a common practice in laying up composites. Laying up more than 6-plies at a time was avoided as it can yield to delamination issues in the composite structure. When all of the plies were vacuum compressed on the debulking table, the plies were kept under vacuum overnight and placed in a curing oven press. A picture of debulked composite samples and an overview of the temperature profile used in the curing oven/press cure procedure are shown in Figure 4.3–3 and Table 4.3–2. The employed cure process was that provided by Hexcel Inc. for curing this type of resin.

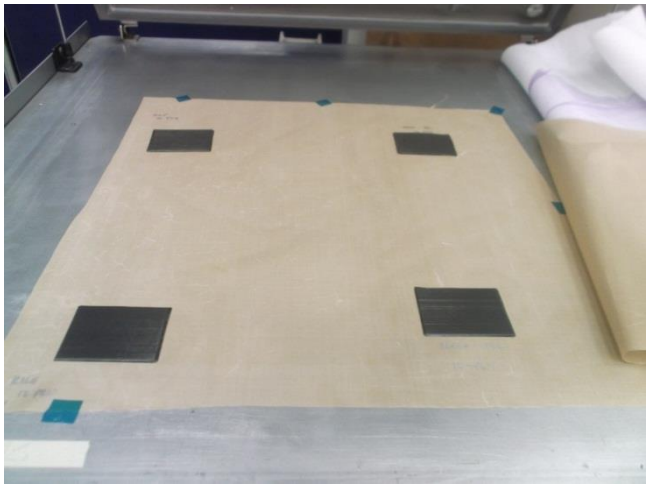

Figure 4.3–3. Composite plies on the debulking table.

Table 4.3–2. Press cure process for IM7 and IM7/SWCNT composites (taken from Reference 56).

Press Cure Cycle	
1.	Put in hot press and apply enough force to achieve 80 psi pressure on the rectangular sample.
2.	Ramp from room temperature to 350 °F at 3 °F/min.
3.	Hold at 350 °F for 2 hours.
4.	Cool to room temperature at 5 °F/min

After curing and cooling, the hybrid composites were machined into circles with ⅛”, ½”, and ⅞” diameters for DSC, thermal diffusivity, and density experiments, respectively. The 12-ply specimens were examined by differential scanning calorimetry (DSC) to determine heat capacities. The 16-ply specimens were used for density and thermal diffusivity measurements. The cut plans are shown in Figure 4.3–4.

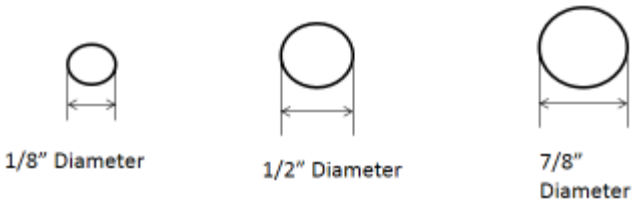

Figure 4.3–4. Summary of samples used for measurements.

4.4 DENSITY

Density (ρ) measurements of the composites were obtained for determining the mass and volume fractions of the CNTs in the composite. This process consisted of measuring the mass of IM7 and of the composites prepared at each of the eight different casting conditions. The mass for each 16-ply specimen was measured in air and then in water at a given temperature. The measurements were obtained using a Mettler Toledo Analytical Scale model number XP204S (Figure 4.4–1) and Mettler Toledo density kit (part number 1106861). The densities of the composite were determined using the equation:

$$\rho = \frac{m_A}{m_A - m_B}(\rho_B - \rho_A) + \rho_A \qquad (2)$$

where m_A = the mass of the sample in air, m_B = the mass of sample in the auxiliary liquid (water is ~ 0.99815 g/cm^3), ρ_B = the density of the auxiliary liquid, and ρ_A = the density of air (0.0012 g/cm^3).

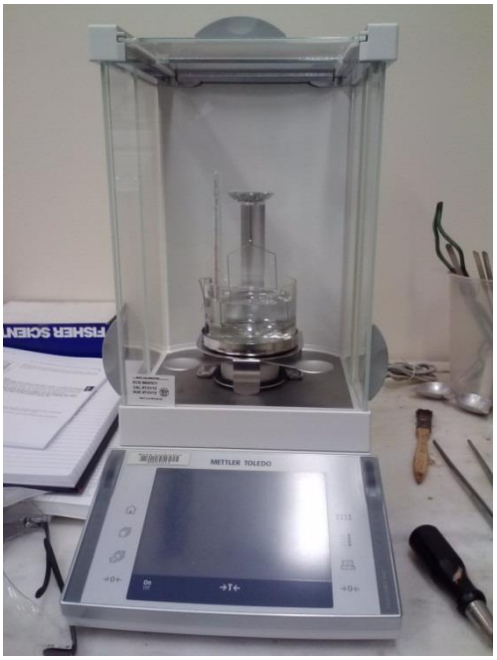

Figure 4.4–1. Mettler Toledo XP204S analytical balance.

Density measurements were performed on six ⅞”- diameter circular disks of 16-ply composite specimen values are given in Table 4.4–1 and Figure 4.4-2. For comparison, the density of SWCNT is ~1550 kg/m^3 or ~2% less than for the virgin IM7 material.[81-82] Within experimental error, the densities of the hybrid composites were the same, as to be expected given the similar densities of the IM7 (1577 kg/m^3) and the SWCNTs that comprise the specimens.

Table 4.4–1. Densities of prepared IM7/SWCNT (in kg/m^3) composites.

wt% SWCNT in IPA Spray	Density (kg/m^3)
0	1572 ± 10
0.007	1579 ± 2
0.009	1570 ± 4
0.02	1570 ± 30
0.04	1590 ± 10
0.06	1573 ± 10
0.08	1585 ± 10
0.1	1570 ± 30

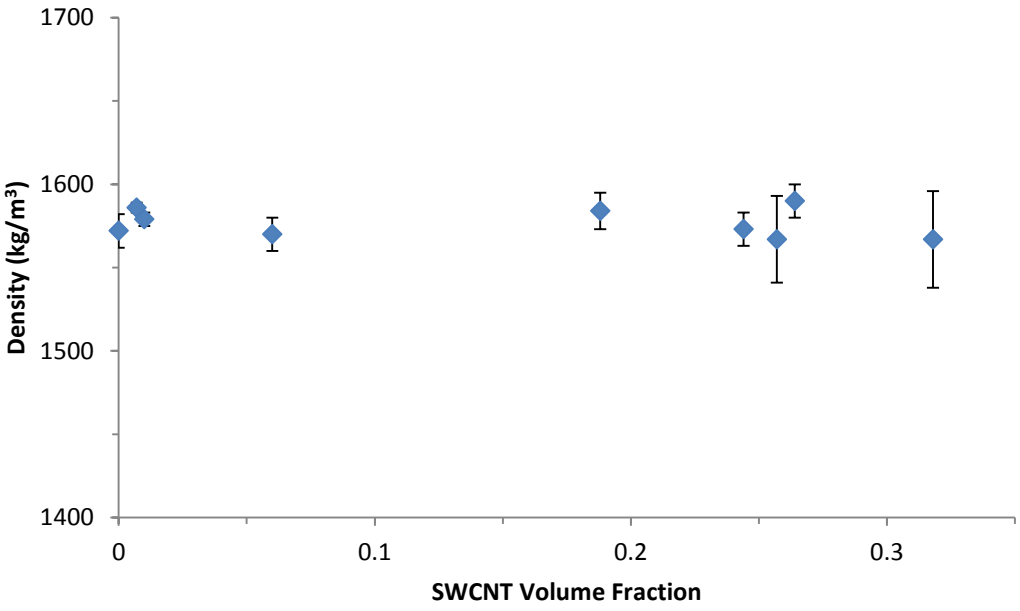

Figure 4.4–2. Densities of IM7/SWCNT and virgin IM7 composites at 300 K.

Mass and volume fractions for the CNTs in the composite were calculated for each of the preparation conditions using data obtained from the density measurements. From the mass and density measurements, the volume for each specimen was calculated. With values for the measured mass and calculated volumes for each specimen, the mass and volume fractions for

the SWCNTS in each samples were determined. These values and their mean errors are summarized in Table 4.4–2.

Table 4.4–2. Compositions of the prepared IM7/SWCNT hybrid composites.

SWCNT wt% in IPA Dispersion	**SWCNT Volume Fraction in IM7/SWCNT Composite** $\left(\frac{V_{CNT}}{V_{IM7}+V_{CNT}}\right)$	**SWCNT Mass Fraction in IM7/SWCNT Composite** $\left(\frac{M_{CNT}}{M_{IM7}+M_{CNT}}\right)$
0	0	0
0.007	0.0107± 0.0008	0.0123 ± 0.0008
0.009	0.062 ± 0.002	0.0616 ± 0.0006
0.02	0.244 ± 0.005	0.243 ± 0.004
0.04	0.188 ± 0.004	0.193 ± 0.008
0.06	0.264 ± 0.004	0.272 ± 0.008
0.08	0.257 ± 0.013	0.254 ± 0.008
0.1	0.32 ± 0.02	0.32 ± 0.02

In Table 4.4–2, the SWCNT content in the solution used to coat the IM7 did not always correlate with the mass (or volume) fraction for the SWCNTs in the resulting composites. For instance, spraying the SWCNTs/IPA solution of 0.02 wt% onto IM7 yielded a SWCNT volume fraction of 0.257 in the prepared composite, while the 0.08 wt% SWCNTs/IPA solution yielded a SWCNT volume fraction of 0.19. While the 0.08 wt% solution contained a higher concentration of SWCNTs in it, this did not correlate with there being a greater amount of SWCNTs being contained on the composite. As varying amounts of the spraying solutions dripped off the vertically held IM7 sheets as they were being applied, the lack of correlation is likely a result of this process and differences in batch-to-batch conditions.

4.5 SPECIFIC HEAT CAPACITY MEASUREMENTS

Specific heat capacity (C_p) measurements were performed on 12-ply specimens using a TA Instruments DSC Q2000 (Figure 4.5–1). A modulated quasi-isothermal method was used to perform these measurements at a hold time of 30 minutes at each temperature from 120 to 470 K, in 50 K increments.

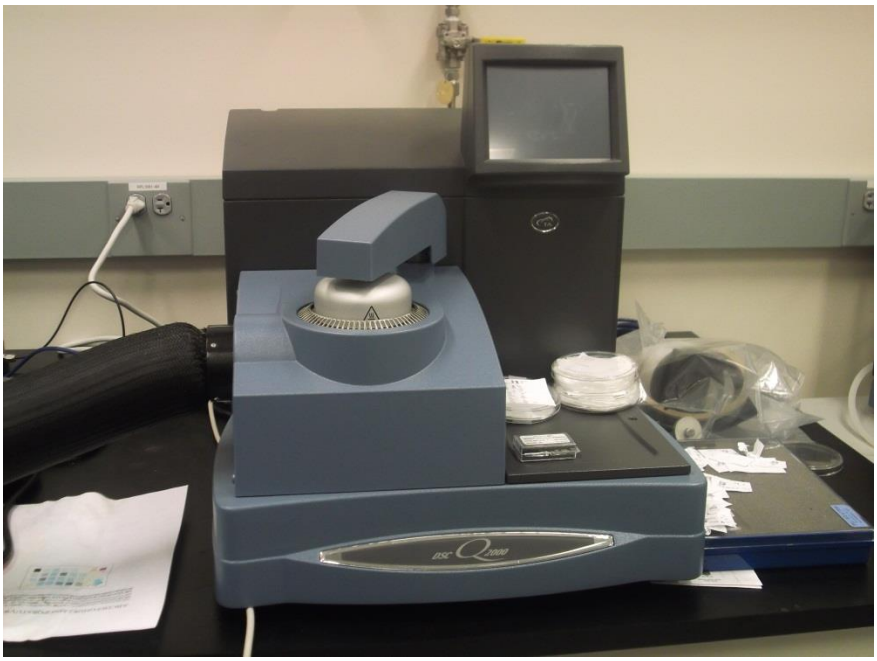

Figure 4.5–1. TA Instruments Q2000 DSC Instument.

After every three tests, a sapphire standard was run to re-calibrate the instrument as per specifications from TA Instruments. The calibration equation used for this instrument was:

$$K_{cp} = \frac{C_{p,expected}}{C_{p,observed}} \quad (3)$$

where K_{cp} was determined for each temperature. Data for the composites were corrected using the equation:

$$C_{p,corrected} = K_{cp} * C_{p,uncorrected} \quad (4)$$

The C_p measurements were performed on the specimens in random order. Figures 4.5–2 through 4.5–10 and Table 4.5–1 summarize the thermal storage of the IM7 and hybrid composites. In these results, the error bars represent standard deviation values for the means. As shown, the data would seem to suggest that the presence of the CNTs results in an increase in C_p by as much as 20 – 30% over the explored temperature range, although other factors maybe responsible for this difference.

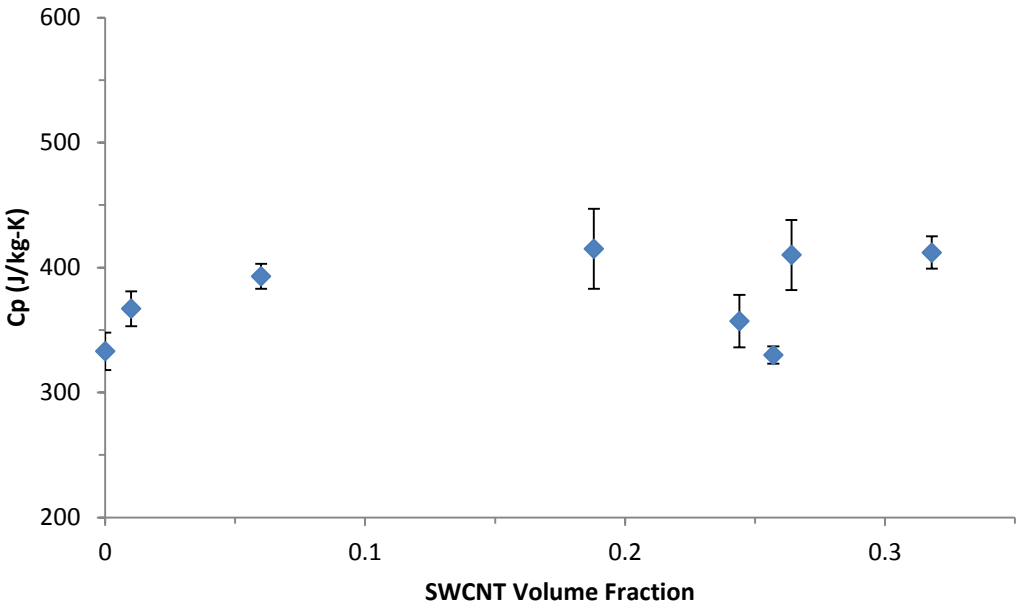

Figure 4.5–2. of IM7/SWCNT composites.

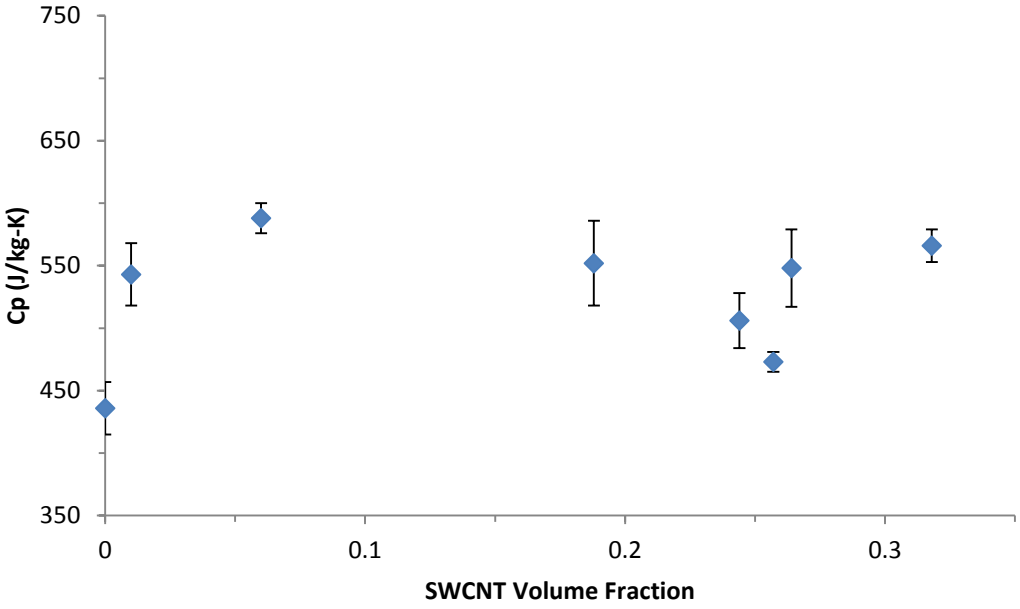

Figure 4.5–3. C_p at 170 K of IM7/SWCNT composites.

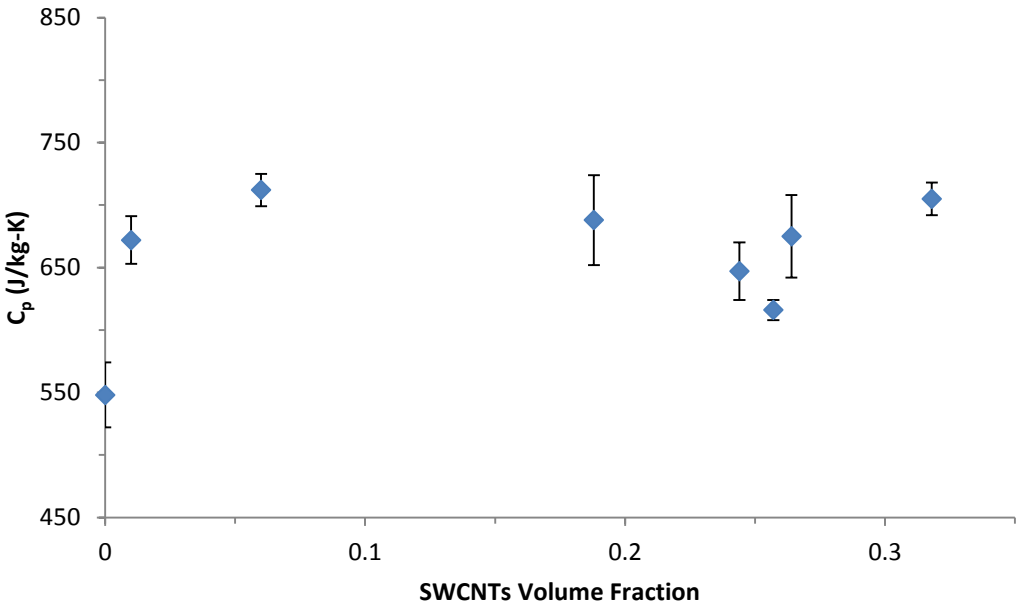

Figure 4.5–4. at 220 K of IM7/SWCNT composites.

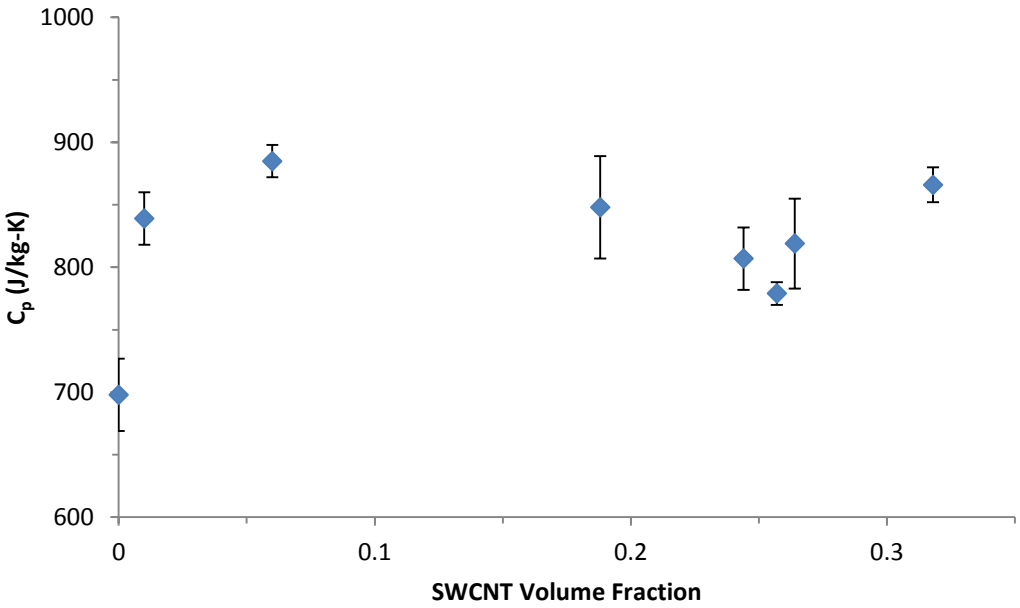

Figure 4.5–5. at 270 K of IM7/SWCNT composites.

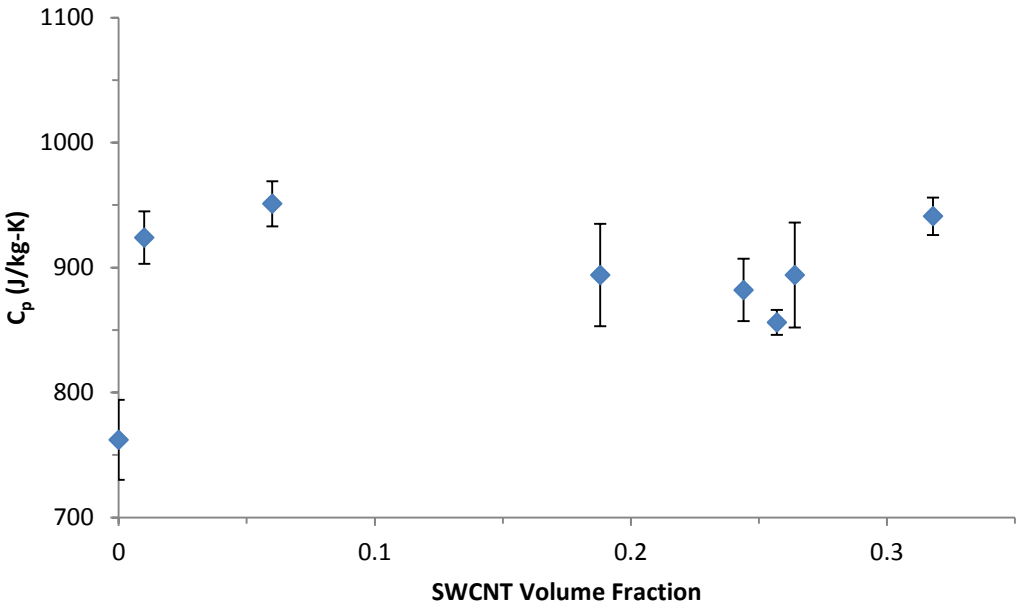

Figure 4.5–6. at 300 K of IM7/SWCNT composites.

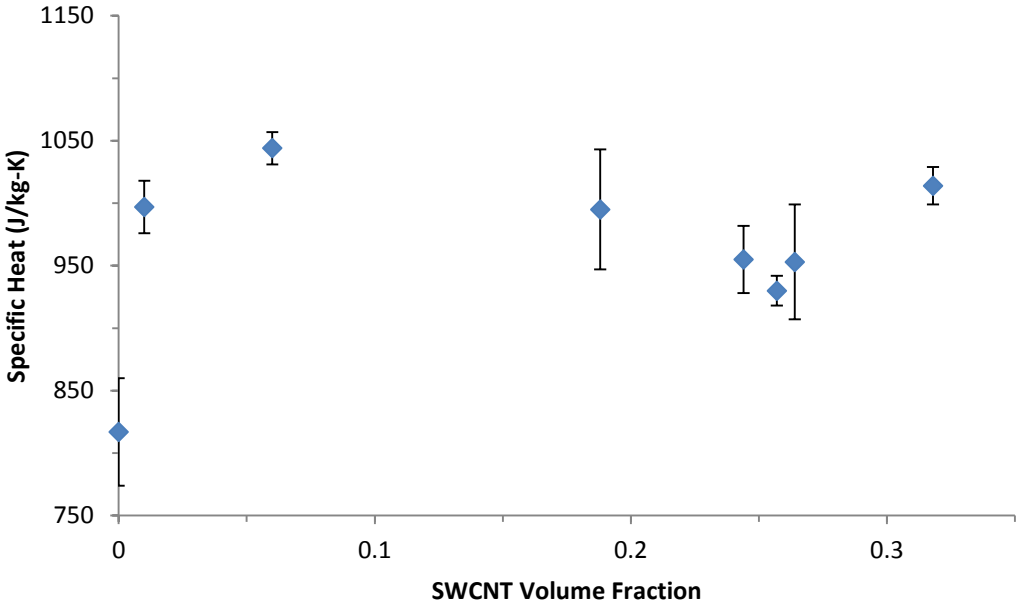

Figure 4.5–7. at 320 K of IM7/SWCNT composites.

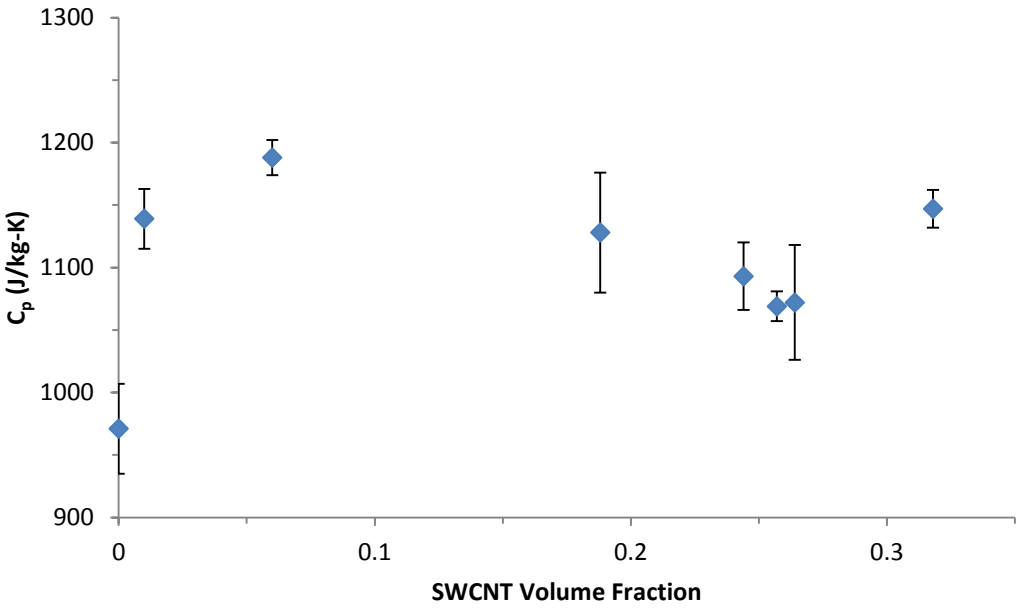

Figure 4.5–8. at 370 K of IM7/SWCNT composites.

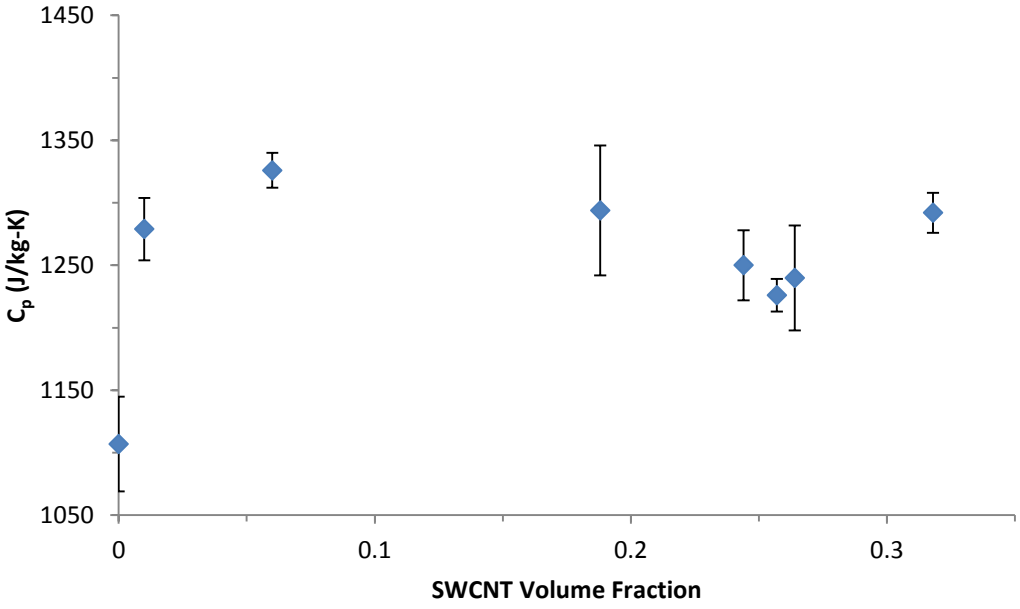

Figure 4.5–9. at 420 K of IM7/SWCNT composites.

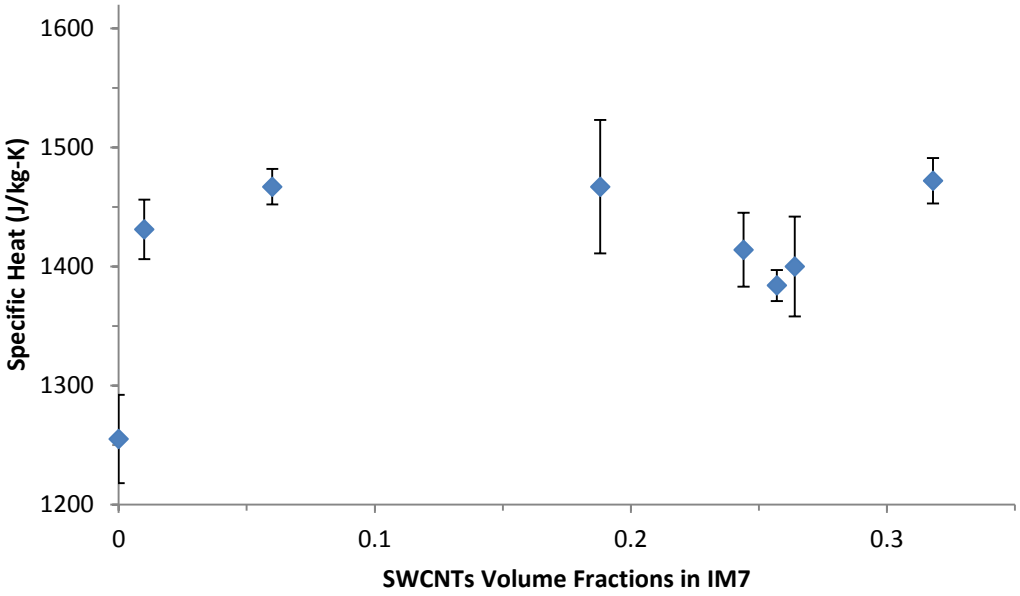

Figure 4.5–10. at 470 K of IM7/SWCNT composites.

Table 4.5–1. Specific heat capacities (in J/kg–K) of IM7/SWCNT composites as affected by temperature and CNT composition.

	SWCNT Volume Fraction							
Temperature	**Virgin**	**0.01**	**0.06**	**0.19**	**0.24**	**0.26**	**0.26**	**0.32**
120 K	333 ± 15	370 ± 15	395 ± 15	415 ± 30	360 ± 20	330 ± 10	410 ± 30	410 ± 15
170 K	435 ± 20	545 ± 25	590 ± 10	550 ± 35	505 ± 20	475 ± 10	550 ± 30	565 ± 15
220 K	550 ± 25	670 ± 20	710 ± 15	690 ± 40	650 ± 25	620 ± 10	675 ± 35	705 ± 13
270 K	700 ± 30	840 ± 20	890 ± 15	850 ± 40	810 ± 25	780 ± 10	820 ± 40	865 ± 15
300 K	760 ± 30	925 ± 20	950 ± 20	830 ± 34	800 ± 25	855 ± 10	820 ± 40	870 ± 15
320 K	820 ± 45	1000 ± 20	1045 ± 15	955 ± 45	955 ± 25	930 ± 10	955 ± 40	1015 ± 15
370 K	970 ± 35	1140 ± 25	1190 ± 15	1130 ± 50	1095 ± 25	1070 ± 10	1070 ± 50	1150 ± 15
420 K	1110 ± 40	1280 ± 25	1325 ± 15	1290 ± 50	1250 ± 30	1230 ± 15	1240 ± 40	1290 ± 15
470 K	1250 ± 40	1430 ± 25	1470 ± 15	1470 ± 60	1410± 30	1385 ± 15	1400 ± 40	1470 ± 20

It is worth noting here that IM7 has a shelf life of about one year, during which its C_p value can decrease by 20%, which is on the order of variations in C_p observed in Figures 4.5–2 through 4.5–11 at any one temperature for changes in CNT content. In these figures, the age of the IM7 was not held constant and some of the higher C_p values for the composite could be due to it being prepared from a newer supply of IM7. From physical property data provided by the IM7 supplier (Hexcel), IM7 has a C_p of approximately 960 J/kg–K at 300 K. I note for comparison that my experimental measurements of C_p on multi-ply samples of IM7 (with no incorporated SWCNTs) yielded a much lower average value of around 770 J/kg–K.

For the prepared IM7/SWCNT composites, their average C_p values at 300 K (Figure 4.5-6) were all below the reported C_p value of 960 J/kg–K for virgin IM7. Given that the differences in C_p values for the examined samples were within the uncertainties that could result from age effects and that no composite sample exhibited a C_p value greater than that expected for fresh IM7 (i.e., 960 J/g-K), the inference from Figure 4.5-2 through 4.5-10 that SWCNT incorporation led to an increase in C_p for IM7 cannot be made. In contrast, as the reported C_p values for SWCNTs (600 J/g-K) are less than those for IM7 (960 J/g-K), the expectation is that increased SWCNT content should yield lower C_p values for the composites. For the explored range of SWCNT content, the effects on C_p were not apparent and may be smaller than the experimenal uncertainty in the measured C_p values. The expected effects that SWCNT content should have on the C_p values for the composites are examined in greater detail in Chapter 5.

Figure 4.5-11 illustrates the effect of temperature on the average C_p values for the IM7/SWCNT composites. As the temperature increased, the IM7 composites regardless of SWCNT content exhibited a linear increase in C_p of ~3.0 J/kg-K between 120 and 470 K.

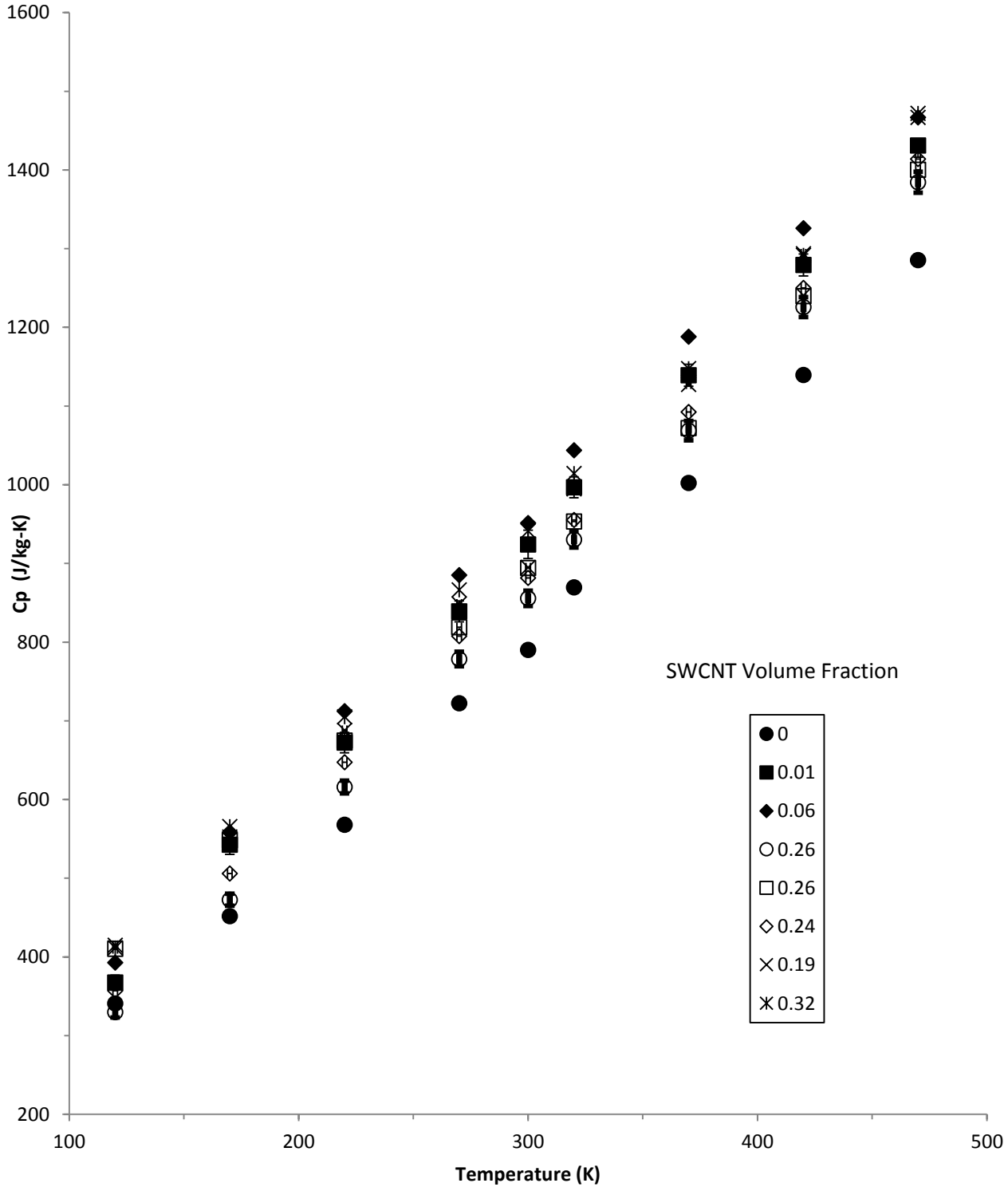

Figure 4.5–11. Effect of temperature and SWCNT content on the heat capacities of IM7/SWCNT hybrid composites. Errors in C_p values were typically ± 20 J/kg–K.

C_p measurements were also done on the SWCNTs used in this work over the explored temperature range. One of the goals of this thesis is to provide a model for the thermal properties of the composite as a function of temperature and CNT composition. As such, values of C_p for the SWCNTs were needed for this model as well as to allow comparison with the literature values for the component materials.

Figure 4–5.12 shows the measured C_p values on the SWCNTs from 120 K to 470 K. At many of the temperatures (specifically those between 120 K – 200 K and 320 K – 470 K), the measured C_p values on the employed SWCNTs were similar to those reported in the literature for SWCNTs within experimental error.[79] At temperatures around 300 K, the C_p values exhibited the unexpected behavior of displaying a decrease with increasing temperatures. This dip in Figure 4.5-12 reflects an exothermic transition that compromises the C_p values obtained around 300 K. Such transitions with CNTs are well known as Hone et al.[79] have reported a similar thermal observation when SWCNTs were analyzed in a helium environment and cooled to or warmed from low temperatures. At around 300 K, helium can absorb into the SWCNTs and the enthalpy change associated with this process results in the thermal measurements of C_p including this additional change to the SWCNTs. To avoid this effect, I looked into the possibility to reconfigure the apparatus to change environment within the employed DSC instrument, but it was not possible. As an alternative, as the measured C_p values outside the temperature range where the effects of helium absorption have an influence were similar to those reported in the literature for SWCNTs, C_p values from the literature for SWCNTs were used in developing the models detailed in Chapter 5 for the composites. The agreement with the literature for the SWCNT C_p values measured outside of 270 – 320 K provided validation for using C_p values from the literature for the SWCNTs in modeling the properties of the IM7/SWCNT composites.

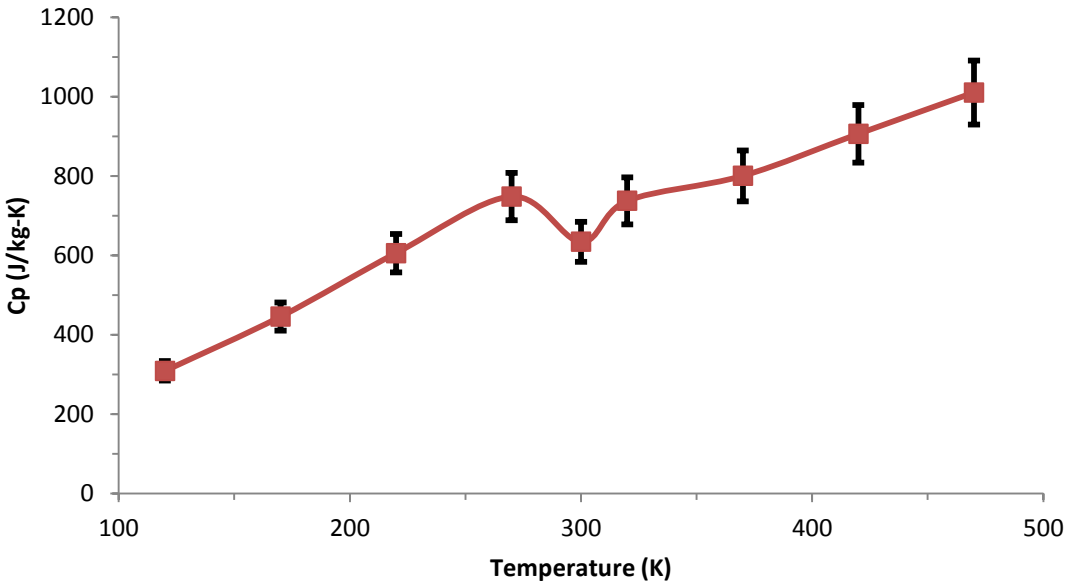

Figure 4.5–12. C_p measurements of SWCNTs under a helium environment. The line is provided as a guide to the eye. The unexpected dip around 300 K is discussed in the text.

4.6 THERMAL DIFFUSIVITY EXPERIMENTS

Through-thickness thermal diffusivity experiments were performed using a TA Instruments Flashline 5000 on IM7 and SWCNT/IM7 hybrid composites. The thermal diffusivity specimens were taken from random locations on a larger sprayed panel. The expected result was that higher through-thickness thermal diffusivities would be obtained from samples having greater fractions of SWCNTs. As shown in Figures 4.6–1 through 4.6–10 and in Table 4.6–1, the addition of SWCNTs to IM7 yielded composites with thermal diffusivities that were higher by as much as 20 to 30% over all examined temperatures as compared to the virgin material.

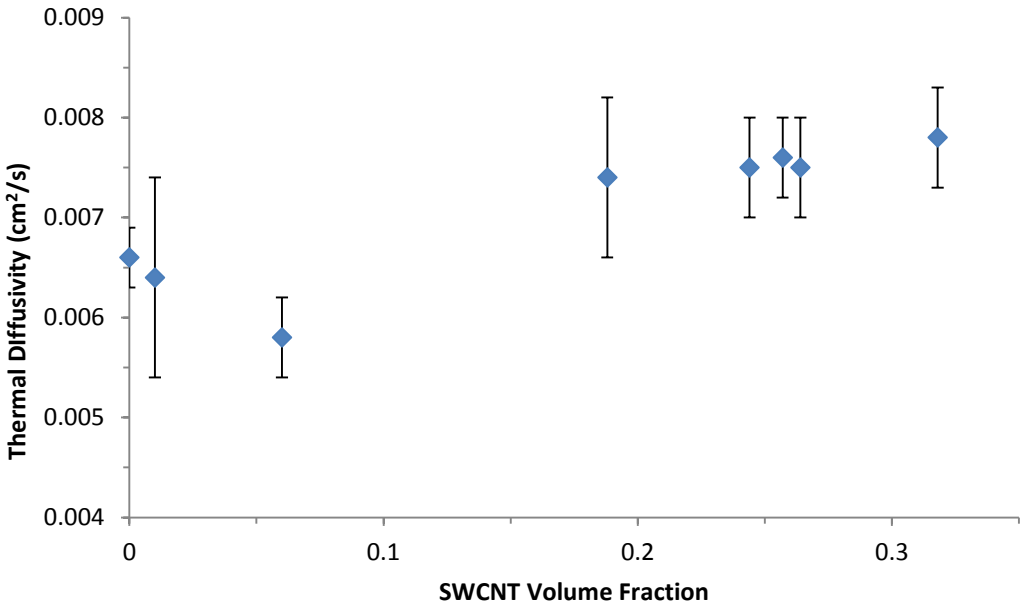

Figure 4.6–1. Through-thickness thermal diffusivity at 120 K of IM7/SWCNT composites.

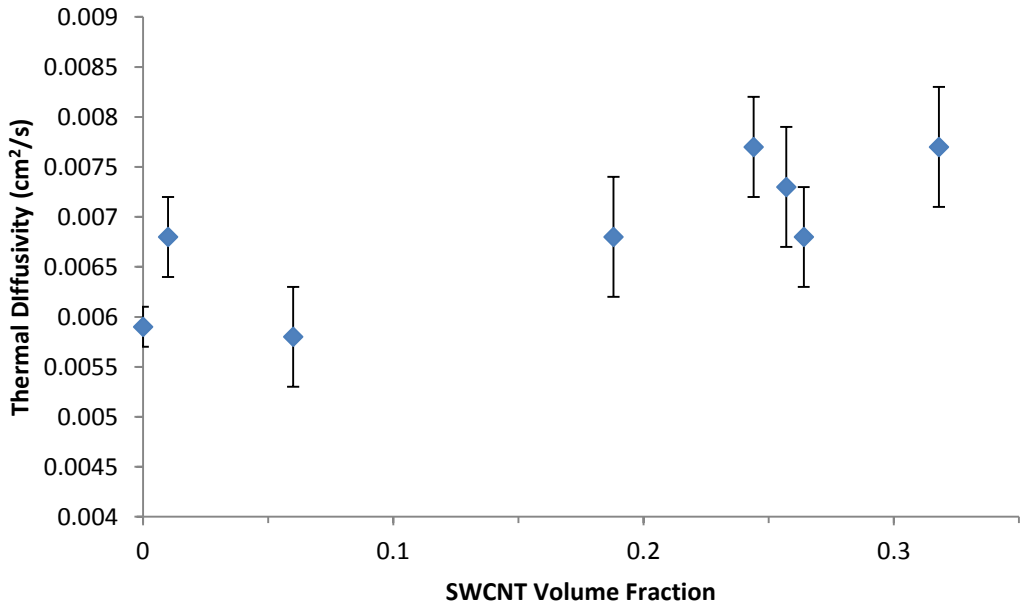

Figure 4.6–2. Through-thickness thermal diffusivity at 170 K of IM7/SWCNT composites.

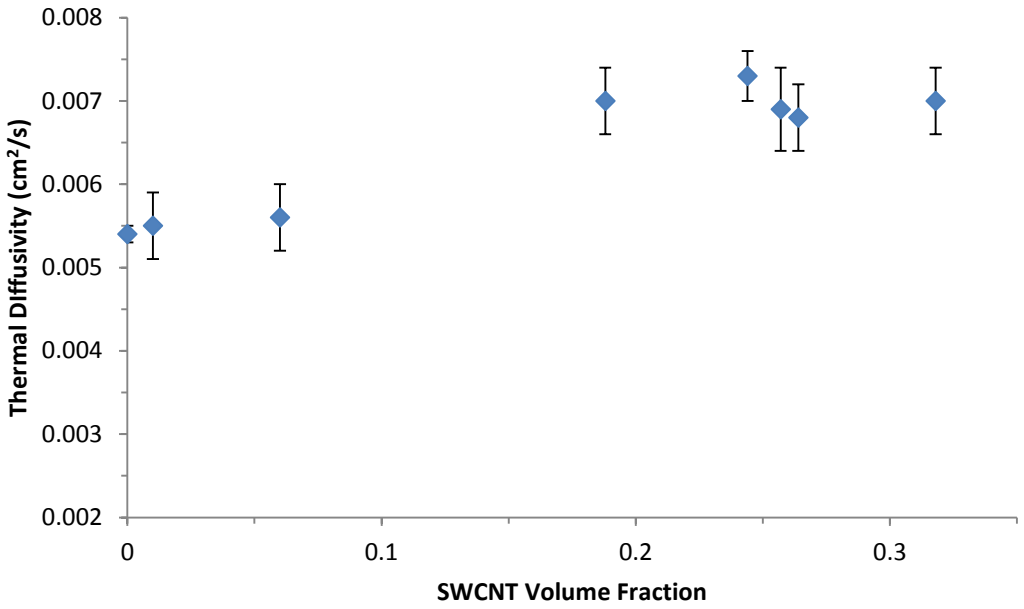

Figure 4.6–3. Through-thickness thermal diffusivity at 220 K of IM7/SWCNT composites.

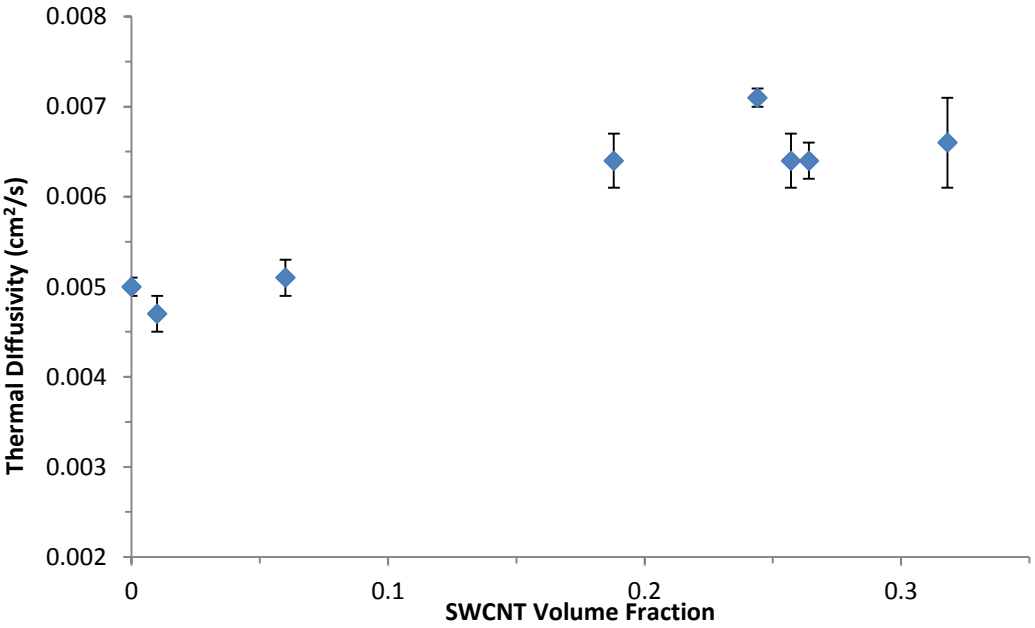

Figure 4.6–4. Through-thickness thermal diffusivity at 270 K of IM7/SWCNT composites.

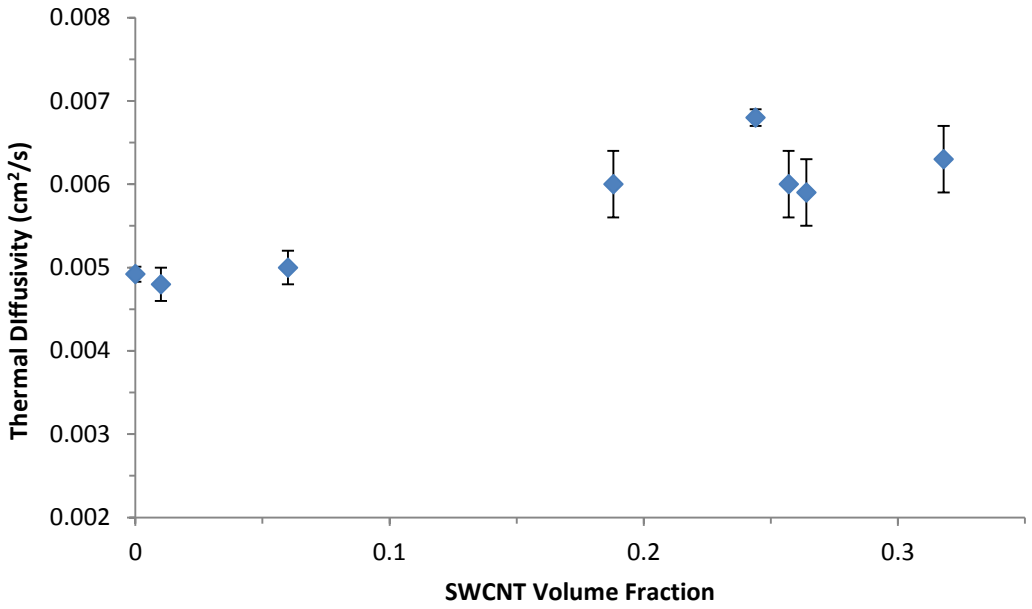

Figure 4.6–5. Through-thickness thermal diffusivity at 300 K of IM7/SWCNT composites.

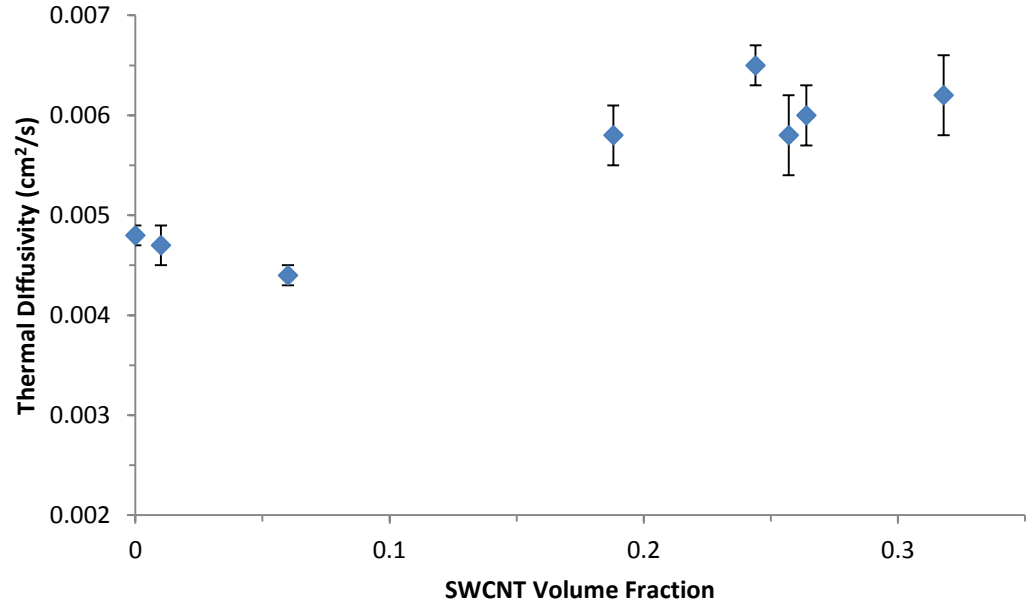

Figure 4.6–6. Through-thickness thermal diffusivity at 320 K of IM7/SWCNT composites.

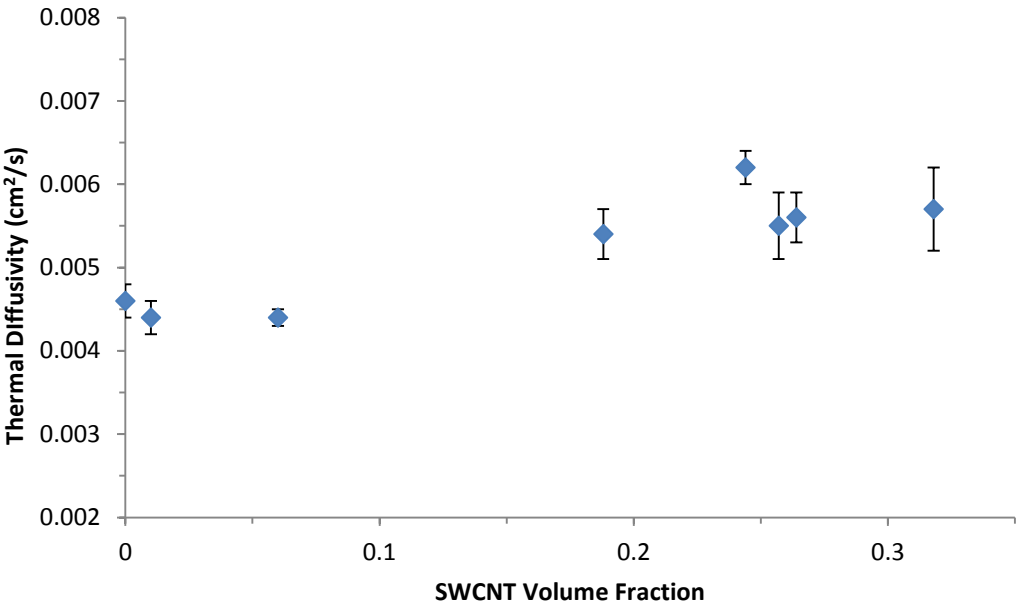

Figure 4.6–7. Through-thickness thermal diffusivity at 370 K of IM7/SWCNT composites.

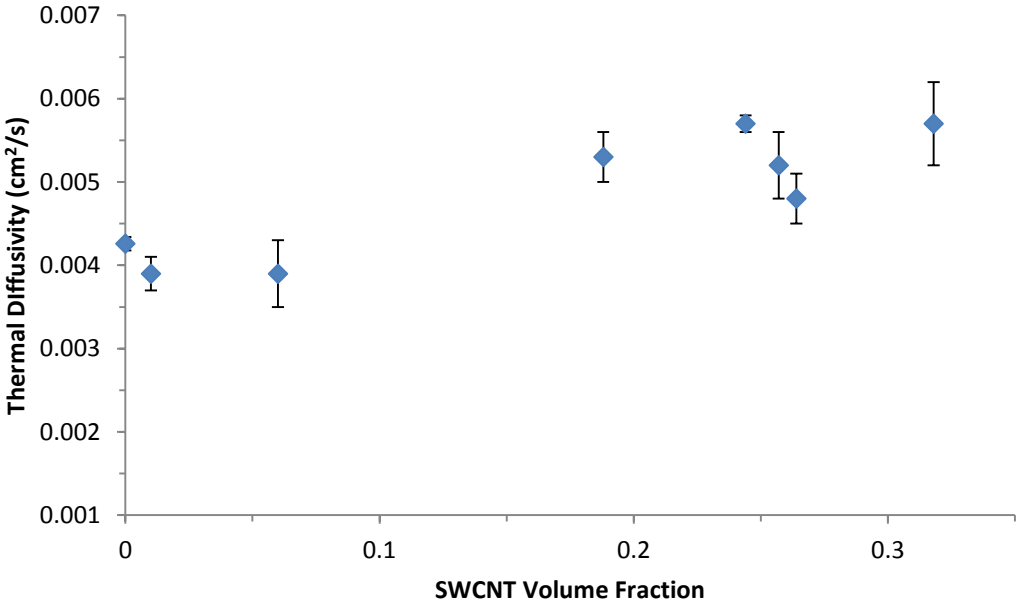

Figure 4.6–8. Through-thickness thermal diffusivity at 420 K of IM7/SWCNT composites.

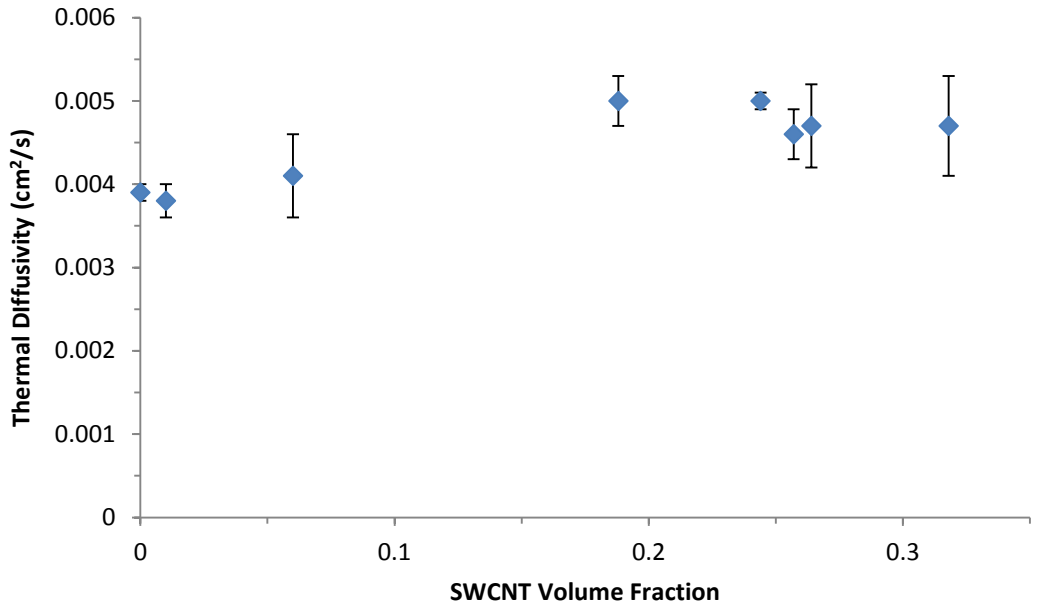

Figure 4.6–9. Through-thickness thermal diffusivity at 470 K of IM7/SWCNT composites.

Table 4.6–1. Through-thickness thermal diffusivities (in cm^2/s) of IM7/SWCNT as affected by temperature and CNT composition.

	SWCNT Volume Fraction							
Temperature	**Virgin**	**0.01**	**0.06**	**0.19**	**0.24**	**0.26**	**0.26**	**0.32**
120 K	0.0066 ± 0.0003	0.0061 ± 0.0012	0.0058 ± 0.0004	0.007 ± 0.0006	0.008 ± 0.0005	0.0076 ± 0.0004	0.0080 ± 0.0008	0.0080 ± 0.0005
170 K	0.0059 ± 0.0002	0.0068 ± 0.0004	0.0060 ± 0.0007	0.0070 ± 0.0006	0.008 ± 0.0009	0.0073 ± 0.0003	0.0070 ± 0.0006	0.0080 ± 0.0006
220 K	0.00541 ± 0.00012	0.0055 ± 0.0004	0.0056 ± 0.0004	0.0070 ± 0.0004	0.0073 ± 0.0003	0.0069 ± 0.0002	0.0068 ± 0.0004	0.0070 ± 0.0004
270 K	0.00501 ± 0.00012	0.0047 ± 0.0002	0.0051 ± 0.0002	0.0054 ± 0.0003	0.0071 ± 0.0001	0.0064 ± 0.0003	0.0064 ± 0.0002	0.0070 ± 0.0005
300 K	0.00492 ± 0.00009	0.0048 ± 0.0002	0.0050 ± 0.0002	0.0060 ± 0.0004	0.0068 ± 0.0001	0.0060 ± 0.0001	0.0059 ± 0.0004	0.0063 ± 0.0004
320 K	0.0048± 0.0001	0.0047 ± 0.0001	0.0044 ± 0.0001	0.0058 ± 0.0003	0.0065 ± 0.0002	0.0058 ± 0.0003	0.0060 ± 0.0003	0.0062 ± 0.0004
370 K	0.0046 ± 0.0002	0.0044 ± 0.0001	0.0044 ± 0.0001	0.0054 ± 0.0003	0.0062 ± 0.0002	0.0055 ± 0.0001	0.0056 ± 0.0003	0.0058 ± 0.0004
420 K	0.0043 ± 0.00008	0.0039 ± 0.0002	0.0039 ± 0.0004	0.0053 ± 0.0003	0.0057 ± 0.0001	0.0052 ± 0.0002	0.0048 ± 0.0003	0.006 ± 0.0005
470 K	0.0039 ± 0.00012	0.0038 ± 0.0008	0.005 ± 0.0005	0.0050 ± 0.0003	0.0050 ± 0.0001	0.0046 ± 0.0001	0.0050 ± 0.0003	0.005 ± 0.0006

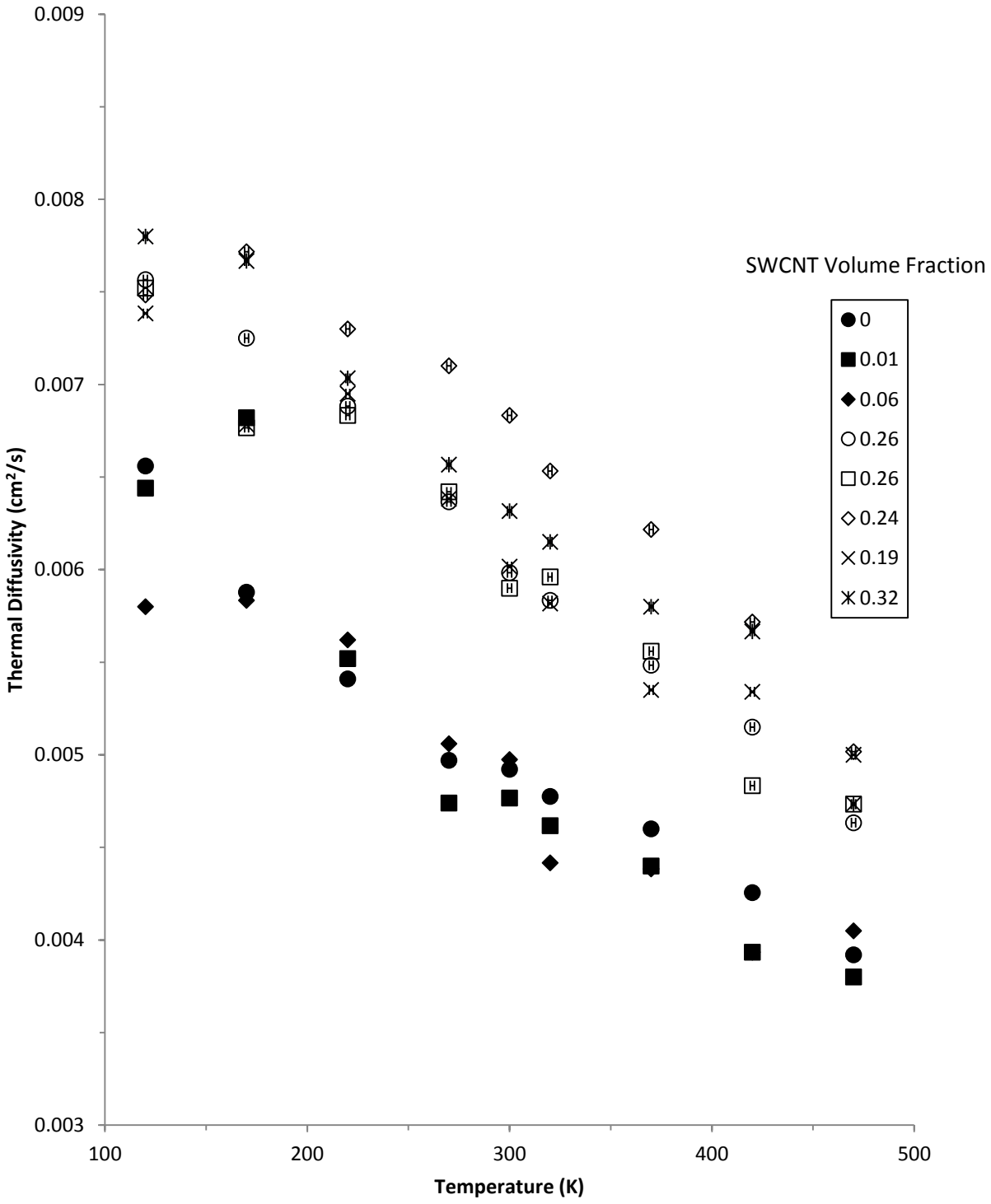

Figure 4.6–10. Effect of temperature and composition on through-thickness thermal diffusivity of hybrid IM7/SWCNT composites.

Figure 4.6-10 summarizes the effects of composition and temperature on the through-film thermal diffusivity of the composite. Overall, the IM7/SWCNT composites showed the general trend that their through-film thermal diffusivities decreased with increasing temperature. The values at 470 K were roughly 30% lower than at 120 K across all sample compositions. The data exhibit the general trend at each temperature that higher SWCNT content yields a higher through-film diffusivity, with some exceptions. For the composites prepared with a SWCNT volume fraction of 0.06, they consistently exhibited values lower than might be expected based on the results from the other samples, while the composite prepared with a SWCNT volume fraction of 0.24 generally exhibited values greater than those expected based on the results from the other samples. These deviations may reflect uncertainties in the compositions of the samples or in the measured through-film diffusivity values. The expected levels of improvement that SWCNT content has on the through-thickness thermal diffusivity values for the composites are considered in Chapter 5, after which the experimental results presented above are compared with these expectations.

In a previous section, I noted that the thermal properties of IM7, specifically its heat capacity, can change with time as it ages. For completeness, it is worth noting that the age of the IM7 sample did not appear to affect the thermal diffusivity of the composite to an observable extent. To examine this issue, a control experiment was conducted to compare the properties of older and newer IM7 samples. Within experimental error, the thermal diffusivity values for the examined samples were the same within experimental error at all measured temperatures. For instance, at 300 K, older samples of IM7 exhibited a through-film themal diffusivity value of 0.0049 ± 0.0001 cm^2/s; whereas, newer IM7 samples had a value of 0.0047 ± 0.0002 cm^2/s. From this result, the conclusion is that the addition of SWCNT to the IM7 composite yielded meaningful increases in the through-film thermal diffussivity.

The above figures provide measurements of the through-plane thermal diffusivities for the IM7/SWCNT composites. Structurally, the IM7 contains carbon fibers that are oriented in the plane of a sheet. As a result of this anisotropy, the through-plane thermal diffusivity value for virgin IM7 material is roughly one-fifth its through-thickness thermal diffusivity value (0.0045 cm^2/s versus 0.025 cm^2/s at 300 K).[56] While values for the through-thickness thermal diffusivity for IM7 can be readily obtained from direct measurements, its higher in-plane thermal diffusivity values are more difficult to measure. As a result, the available in-plane thermal diffusivity values for IM7 (for example, from Hexcel) are typically best estimates based on theoretical considerations. With the addition of the SWCNTs (with a higher thermal diffusivity than for IM7) to the composite, both the in-plane and through-plane thermal diffusivities are expected to increase. These inceases are due to the additional competing mean free paths for acoustic phonons in the SWCNT-containing composite that aid in the thermal transport through the material. Obtaining these higher in-plane diffusivity values from measurements for the SWCNT-containing IM7 composites are made more difficult by the presence of the SWCNTs. If pursued, larger amounts of IM7 and of the SWCNTs would be required for generating suitable specimens, the samples would require special machining for testing, and specialized instrumentation (that has not been developed yet) would be needed for measuring these values directly. Because of these obstacles, measurements of in-plane thermal diffusivities for the IM7/SWCNT were not pursued. Instead, the in-plane thermal diffusivity values were modeled using structural information obtained from through-thickness measurements and in-plane values for the component materials.

4.7 THERMAL CONDUCTIVITY

Thermal conductivity, λ, is defined as the product of the thermal diffusivity (α), density (ρ), and heat capacity (C_p):

$$\lambda = \alpha * \rho * C_p \tag{6}$$

Thermal conductivity is the rate of heat transfer at steady-state conditions through a plate of known area and thickness in a direction normal to its surface when its opposing faces differ in temperature by one degree Kelvin ($\lambda = \frac{Q \times L}{A \times \Delta T}$). The reciprocal of thermal conductivity is thermal resistance, which is the ability of a material to prevent the flow of heat.

For each of the 16-ply IM7/SWCNT hybrid composite specimens, their thermal conductivities were calculated using their measured values of α, C_p, and ρ presented in the earlier sections. Figures 4.7–2 through 4.7–9 and Table 4.7–1 present these results and show that the addition of the CNTs to IM7 increases yields a hybrid composite with thermal conductivities that are as much as 30% greater than for IM7. This increase in thermal conductivity was observed over the explored temperature range to different extents. For example, at lower temperatures (specifically those between 120 K– 270 K), the data in Figures 4.7–1 through 4.7–4 tend to show smaller increases in thermal conductivity by adding SWCNTs. At temperatures above 270 K (Figures 4.7–5 through 4.7–9), the thermal conductivities for IM7 and the IM7/SWCNT hybrid composites exhibit greater increases with SWCNT content.

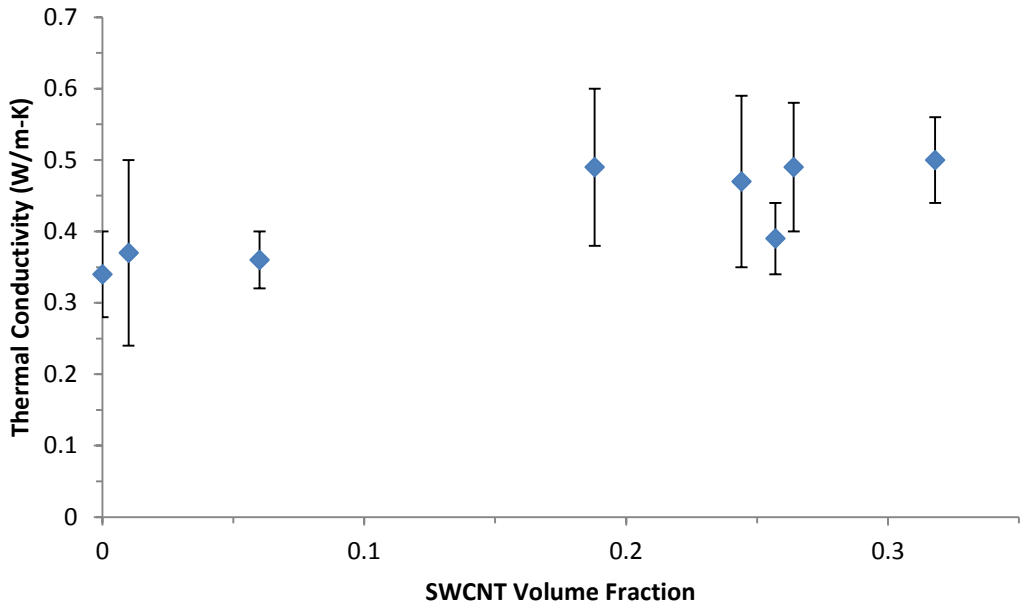

Figure 4.7–1. Through-thickness thermal conductivity at 120 K of IM7/SWCNT composites.

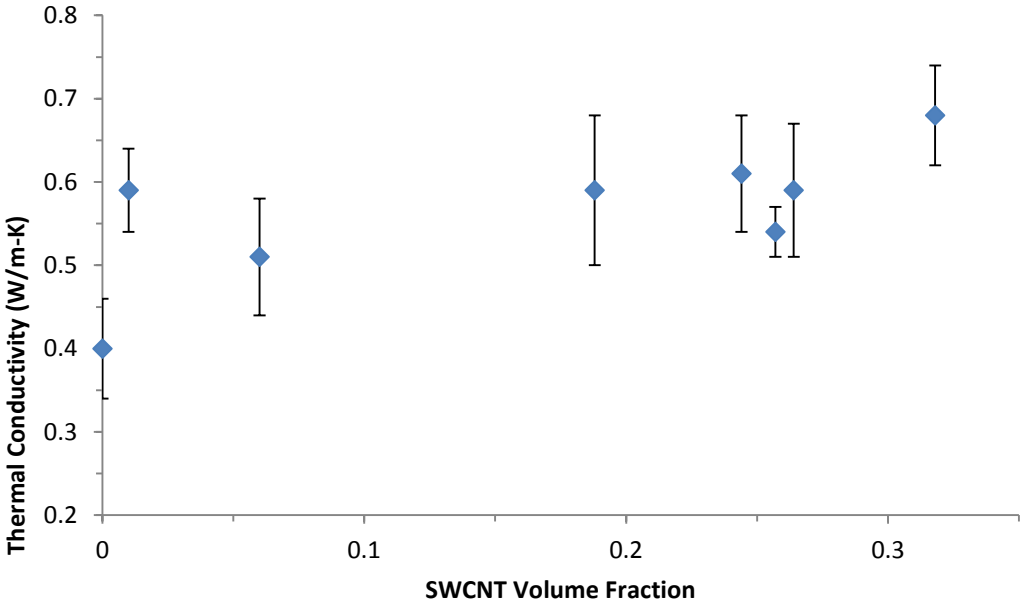

Figure 4.7–2. Through-thickness thermal conductivity at 170 K of IM7/SWCNT composites.

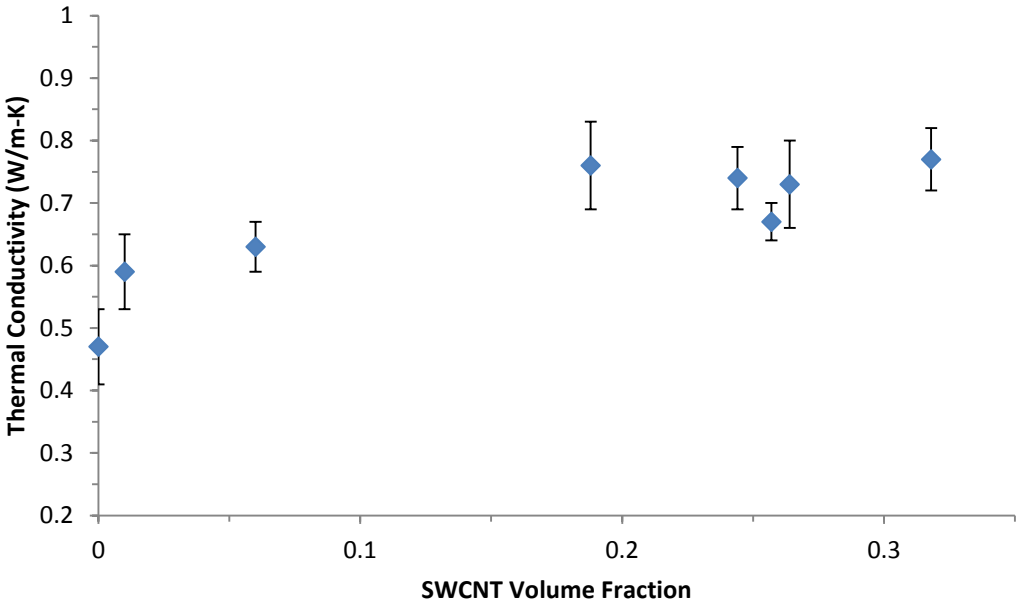

Figure 4.7–3. Through-thickness thermal conductivity at 220 K of IM7/SWCNT composites.

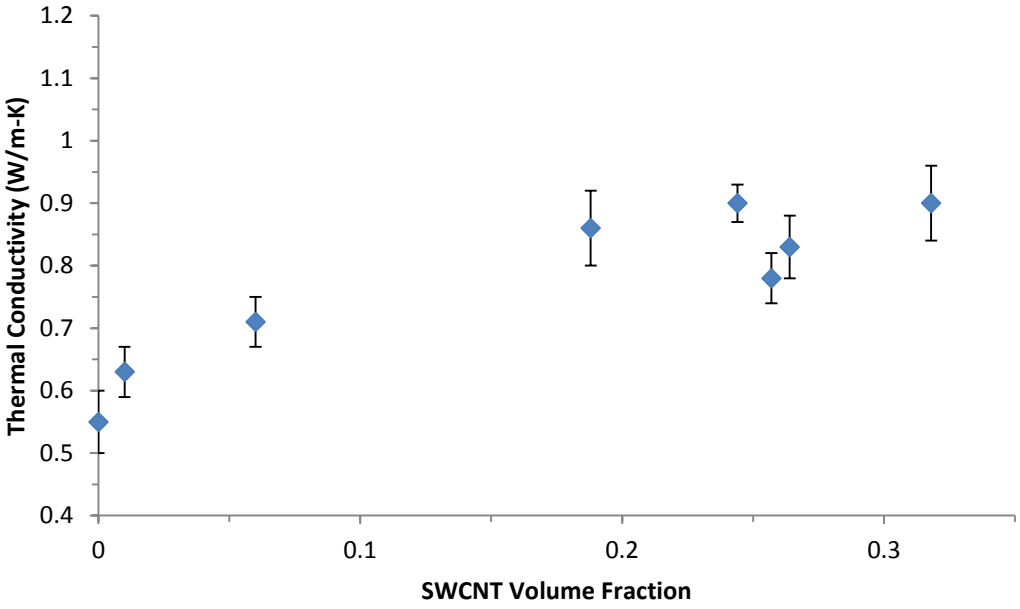

Figure 4.7–4. Through-thickness thermal conductivity at 270 K of IM7/SWCNT composites.

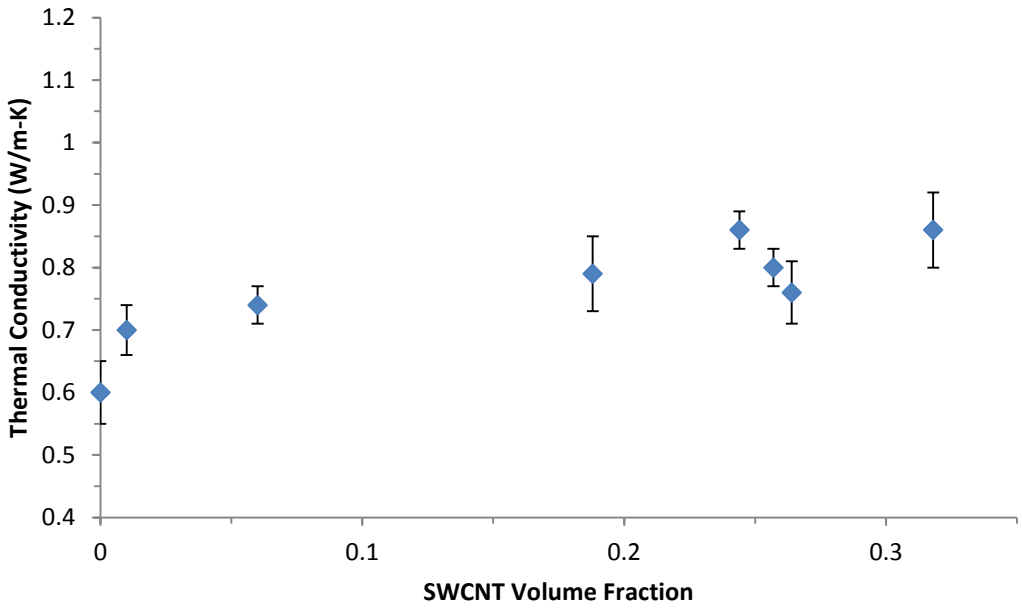

Figure 4.7–5. Through-thickness thermal conductivity at 300 K of IM7/SWCNT composites.

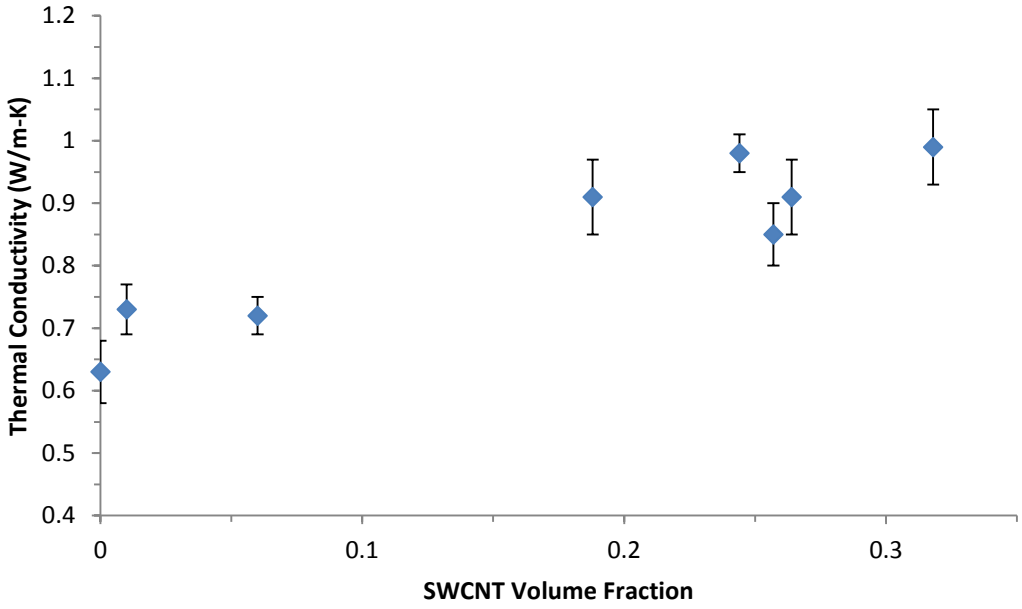

Figure 4.7–6. Through-thickness thermal conductivity at 320 K of IM7/SWCNT composites.

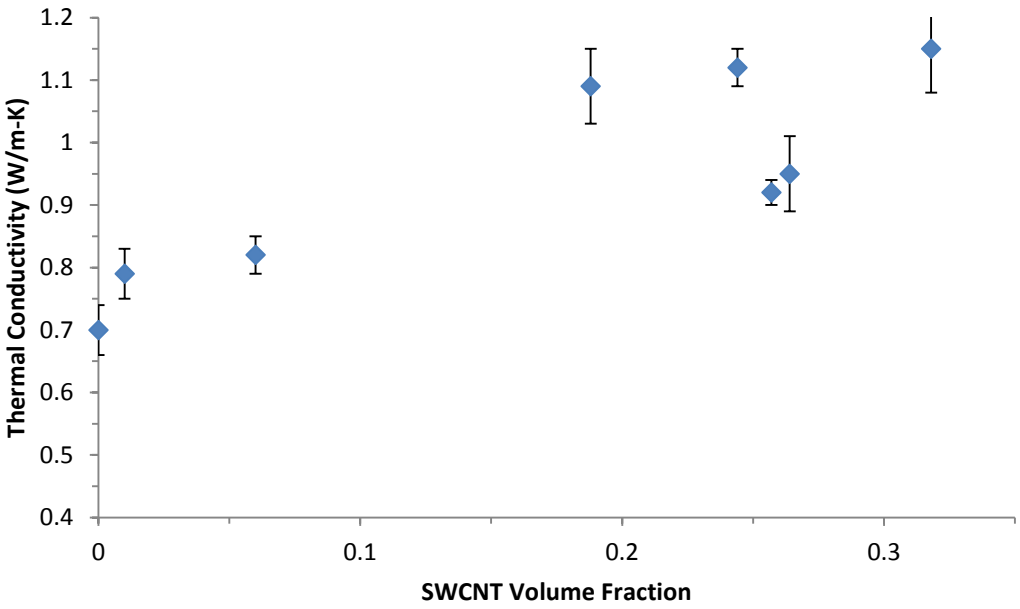

Figure 4.7–7. Through-thickness thermal conductivity at 370 K of IM7/SWCNT composites.

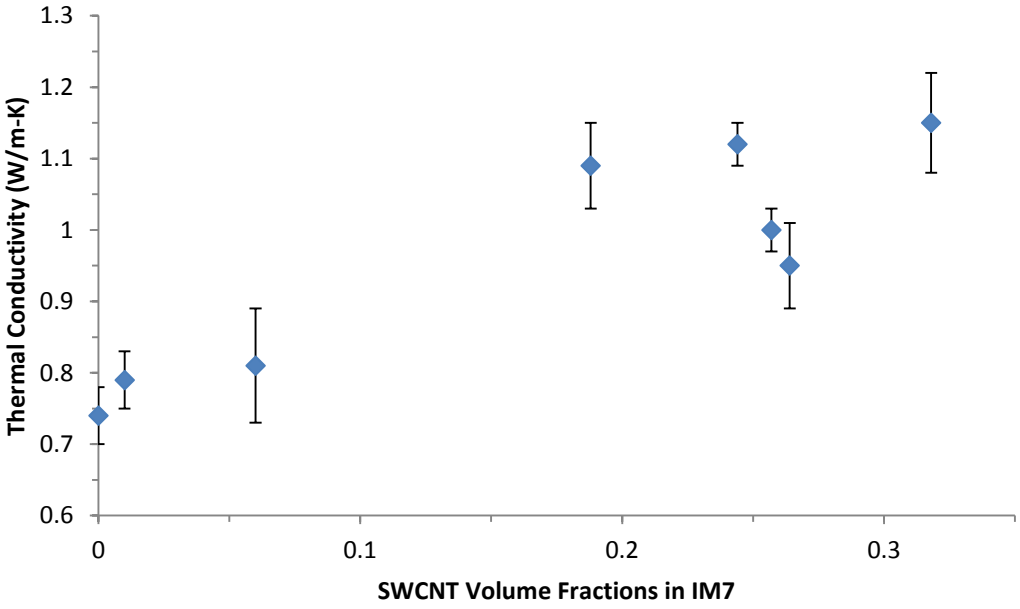

Figure 4.7–8. Through-thickness thermal conductivity at 420 K of IM7/SWCNT composites.

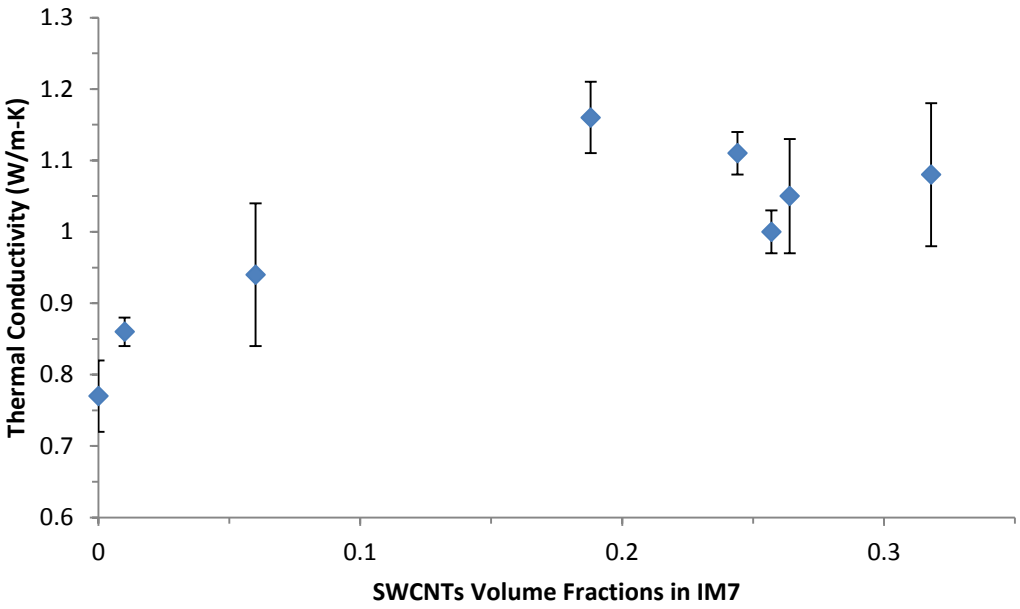

Figure 4.7–9. Through-thickness thermal conductivity at 470 K of IM7/SWCNT composites.

Table 4.7–1. Through-thickness thermal conductivities (in W/m–K) of IM7/SWCNT composites as affected by temperature and CNT content.

	SWCNT Volume Fraction							
Temperature	**Virgin**	**0.01**	**0.06**	**0.19**	**0.24**	**0.26**	**0.26**	**0.32**
120 K	0.34 ± 0.06	0.37 ± 0.13	0.36 ± 0.04	0.49 ± 0.11	0.42 ± 0.12	0.39 ± 0.05	0.49 ± 0.09	0.50 ± 0.06
170 K	0.40 ± 0.06	0.59 ± 0.05	0.51 ± 0.07	0.59 ± 0.09	0.61 ± 0.07	0.54 ± 0.04	0.59 ± 0.08	0.68 ± 0.06
220 K	0.47 ± 0.06	0.59 ± 0.06	0.63 ± 0.04	0.76 ± 0.07	0.74 ± 0.36	0.67 ± 0.03	0.73 ± 0.07	0.77 ± 0.05
270 K	0.55 ± 0.05	0.63 ± 0.04	0.71 ± 0.04	0.86 ± 0.06	0.90 ± 0.03	0.78 ± 0.05	0.83 ± 0.05	0.90 ± 0.06
300 K	0.60 ± 0.05	0.70 ± 0.04	0.74 ± 0.03	0.79 ± 0.06	0.86 ± 0.03	0.80 ± 0.02	0.76 ± 0.05	0.86 ± 0.06
320 K	0.63 ± 0.05	0.73 ± 0.04	0.72 ± 0.03	0.91 ± 0.07	0.98 ± 0.04	0.85 ± 0.06	0.91 ± 0.05	0.99 ± 0.06
370 K	0.70 ± 0.05	0.79 ± 0.04	0.82 ± 0.03	0.96 ± 0.06	1.07 ± 0.03	0.92 ± 0.03	0.95 ± 0.06	1.04 ± 0.06
420 K	0.74 ± 0.04	0.79 ± 0.04	0.81 ± 0.08	1.09 ± 0.06	1.12 ± 0.03	1.00 ± 0.03	0.95 ± 0.06	1.15 ± 0.07
470 K	0.77 ± 0.05	0.86 ± 0.02	0.94 ± 0.10	1.16 ± 0.05	1.11 ± 0.03	1.00 ± 0.03	1.05 ± 0.08	1.08 ± 0.10

Figure 4.7-10 summarizes the effects of composition and temperature on the through-film thermal conductivity of the composite. For each explored composition, the IM7/SWCNT composites showed the general trend that their through-film thermal conductivities increase with increasing temperature. The thermal conductivities at 470 K were more than twice their values at 120 K across all sample compositions. The data exhibit the general trend at each temperature that higher SWCNT content yields a a more themally conductive material, as would be expected since the SWCNTs are more thermally conductive than IM7.

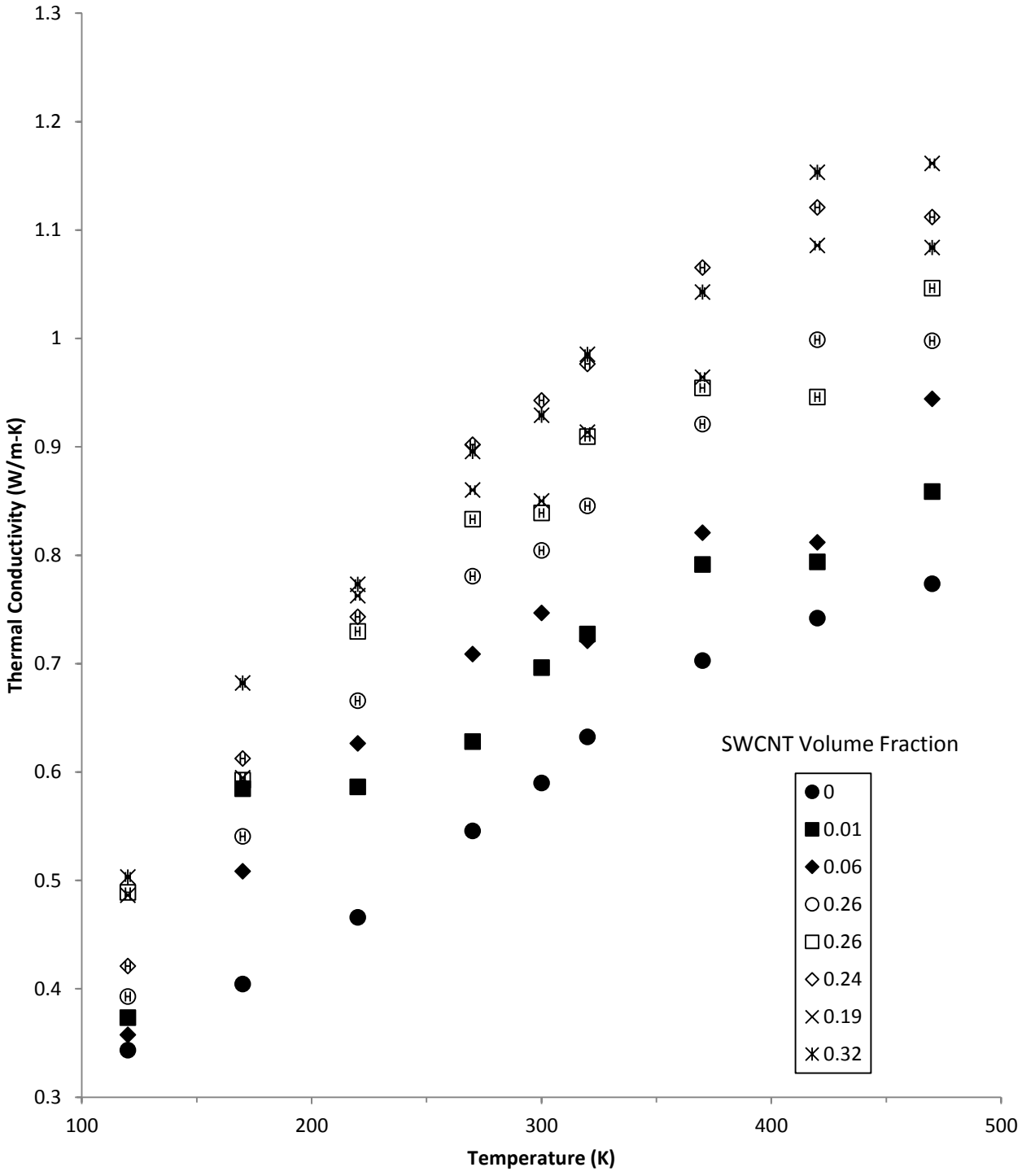

Figure 4.7–10. Effect of temperature and composition of through-thickness thermal conductivity of hybrid (IM7/SWCNT) composites.

The effects that the age of the IM7 used in the composite have on the thermal conductivity of the composite was also considered. As noted in Chapter 4.5, the C_p of IM7 can decrease during storage by as much as 20% a year of its preparation. Such temporal changes in C_p would be expected to directly affect thermal conductivities through Equation 6. As noted in Chapter 4.6, the age of the IM7 appeared to have a negligible effect on its thermal diffusivity, so the anticipated influences on thermal conductivity could be expected to be those due to changes mentioned earlier for C_p. From Table 4.7-1, the addition of SWCNTs to IM7 can produce composites with thermal conductivities that are 40 to 50% higher than those for IM7. As these increases are greater than the variations for C_p that can result from different storage conditions, the increases in thermal conductivity can be concluded to be a result of the added SWCNTs. In Chapter 5, the expected effects of SWCNT content on the through-thickness thermal conductivity values for the composites are presented along with a comparison to the experimental results.

CHAPTER V

HEAT TRANSFER MODEL FOR IM7/SWCNT COMPOSITES

5.1 RESISTANCE MODEL FOR IM7/SWCNT COMPOSITES

Two models were developed to predict the thermal transport (α and λ) properties of the hybrid composites. Each of these models considers the aggregate resistance of a ply as resulting from the resistances of distinct IM7 and SWCNT regions. The first model considers each layer of SWCNTs on the IM7 plies to be uniform and continuous (Figure 5.1–1). As shown in the figure, the thicknesses of each SWCNT layer and each IM7 ply are designated by S_2 and S_1, respectively. The relative thicknesses for the S_1 and S_2 slices define the SWCNT content in the overall structure. As the dominant component in the IM7/SWCNT composites is the IM7 layer, the thickness of the S_1 slice is greater than the thickness of the S_2 layer for all samples.

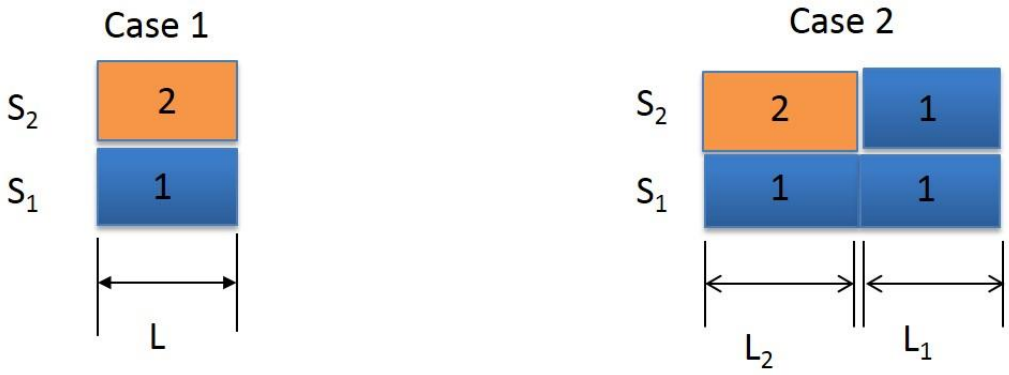

Figure 5.1–1. Two cases of discrete uniform and non-uniform layers of SWCNT on the IM7 composites; S_1 and S_2 are stacked slices through a ply of the IM7/SWCNT composite. Boxes 1 and 2 represent distinct IM7 and SWCNT regions, respectively.

In the second model, each SWCNT layer of a ply is considered to lack continuity, and the S2 layer is instead described as being composed of discrete SWCNT and IM7 regions (see Figure 5.1-1). Here, the S_2 dimension reflects the overall thickness of the SWCNT-containing layer in a ply, where the SWCNT content in this layer is defined by the relative sizes of L_2 and L_1. The presence of IM7 in the S_2 layer insures complete contact with the ply above it in the multi-ply structure, and can be viewed to reflect a condition where the SWCNTs coalesce into valleys on the IM7 surface. The volume fraction of SWCNTs in the composite is manipulated in the model by selecting values of S_2 relative to S_1 and of L_2 relative to L_1.

In analyzing the overall thermal properties for the multi-ply composites with these structures, I assumed that they could be described by a combination of series (through-thickness) and parallel (in-plane) thermal resistances for the individual SWCNT and the IM7 composite regions within a ply.

For both of these models, their overall thermal resistances were of interest for comparison with the experimental data presented in Chapter 4 where global thermal resistance values were obtained for the multi-ply samples. For samples containing relatively high SWCNT volume fractions, Case 1 may be considered as a suitable model since the SWCNT layers have a high degree of interconnectivity for allowing rapid heat transfer across a layer. At lower SWCNT volume fractions, Case 2 may be considered as a more suitable model because the SWCNTs may clump together on the virgin IM7 surface and yield discrete areas where the CNTs lack long-range continuity on the surface. The relevant equations for Cases 1 and 2 are developed below, where those for Case 2 simply to the Case 1 equations when there is no separation between the SWCNT-containing regions in a ply (i.e., when L_1 or $L_1/ L_2 = 0$).

In consideration of a global resistance value for the two cases illustrated in Figure 5.1-1, for any temperature difference present across a material, the associated heat flow can be described by:

$$Q = \frac{\lambda A \Delta T}{x} = \frac{\Delta T}{R} \tag{7}$$

where Q is the rate of heat flow, A is the cross-sectional area of the material, ΔT is the temperature difference present between the two opposing exposed cross-sectional areas of the material, x is the thickness of the material across which there is a temperature difference, λ is the thermal conductivity of the material, and R is the thermal resistance.

Case 1 can be described by two resistances in parallel if the heat flow is from side to side (in-plane) or as two resistances in series if the heat flow is from top to bottom (surface-to-surface). For Case 1, the overall resistances in the in-plane and through-plane directions can be written as:

$$R_{Case\ 1,\ in-plane} = \frac{R_{IM7} R_{SWCNT}}{R_{IM7} + R_{SWCNT}} \tag{8}$$

$$R_{Case\ 1,\ through-plane} = R_{IM7} + R_{SWCNT} \tag{9}$$

Each of the resistances for the IM7 and SWCNT regions can be related to a specific thermal conductivity λ by the equation:

$$R = \frac{x}{\lambda A} \tag{10}$$

For the in-plane configuration,

$$R_1 = R_{IM7} = \frac{L}{\lambda_1 S_1 l} \ , \tag{11}$$

and

$$R_2 = R_{SWCNT} = \frac{L}{\lambda_2 S_2 l} \tag{12}$$

where the cross-sectional area for a material is the product of its in-plane dimensions (l is the depth, and S_1 and S_2 are the lengths of regions 1 and 2, respectively), and L is the thickness of each region. Substituting the expressions for R_{IM7} and R_{SWCNT} into Equation 8 gives:

$$R_{Case\ 1,\ \ in-plane} = \frac{\frac{L}{\lambda_1 S_1 l}\frac{L}{\lambda_2 S_2 l}}{\frac{L}{\lambda_1 S_1 l}+\frac{L}{\lambda S_2 l}} = \frac{\frac{L}{\lambda_1 \lambda_2 S_1 S_2 l}}{\frac{\lambda_2 S_2 + \lambda S_1}{\lambda_1 \lambda_2 S_1 S_2}} = \frac{1}{\lambda_2 S_2 + \lambda_1 S_1}\frac{L}{l} \tag{13}$$

Relating the resistance in Equation (10) to the thermal conductivity by Equation 11 gives

$$R_{Case\ 1,\ \ in-plane} = \frac{x}{\lambda A} = \frac{L}{\lambda_{Case\ 1,\ \ in-plane}(S_1+S_2)l} \tag{14}$$

or

$$\lambda_{Case\ 1,\ \ in-plane} = \frac{\lambda_2 S_2 + \lambda_1 S_1}{S_1 + S_2} = \frac{\lambda_2 \frac{S_2}{S_1} + \lambda_1}{1 + \frac{S_2}{S_1}} = \frac{\lambda_2 f_s + \lambda_1}{1 + f_s} \quad (15)$$

where $f_s = \frac{S_2}{S_1}$ is the ratio of the volume of the SWCNTs in the composite as compared to the volume of the IM7 in the composite.

Relatedly, the through-thickness equations for the IM7 and SWCNT layers are:

$$R_1 = R_{IM7} = \frac{S_1}{L\lambda_1 l}, \quad (16)$$

and

$$R_2 = R_{SWCNTs} = \frac{S_2}{L\lambda_2 l} \quad (17)$$

Substituting these expressions for R_{IM7} and R_{SWCNT} into Equation 9 gives

$$R_{Case\ 1,\ \ through-plane} = \frac{S_1}{L\lambda_1 l} + \frac{S_2}{L\lambda_2 l} = \frac{\lambda_2 S_1 + \lambda S_2}{L\lambda_1 \lambda_2 l} \quad (18)$$

Relating the resistance in Equation (10) to the thermal conductivity by Equation 11 gives

$$R_{Case\ 1,\ \ through-plane} = \frac{x}{\lambda A} = \frac{S_1 + S_2}{\lambda_{Case\ 1,\ \ through-plane} L l} \quad (19)$$

or

$$\lambda_{Case\ 1,\ through-plane} = \frac{(S_1+S_2)\lambda_1\lambda_2}{\lambda_2 S_1+\lambda_1 S_2} = \frac{\left(1+\frac{S_2}{S_1}\right)\lambda_1\lambda_2}{\lambda_2+\lambda_1\frac{S_2}{S_1}} = \frac{(1+f_S)\lambda_2\lambda_1}{\lambda_2+\lambda_1 f_S} \quad (20)$$

The expressions in Equations 15 and 20 can be further modified to relate the thermal conductivities to the SWCNT volume fraction, *a*, in the composites. The SWCNT volume fraction, *a*, is defined as the volume of the SWCNTs in the composite divided by the total volume of the composite (SWCNT + IM7), and can be related to the ratio of the SWCNT to IM7 volumes, f_s, by:

$$a = \frac{V_{SWCNT}}{V_{IM7}+V_{SWCNT}} = \frac{S_2 Ll}{S_1 Ll+S_2 Ll} = \frac{S_2}{S_1+S_2} = \frac{\frac{S_2}{S_1}}{1+\frac{S_2}{S_1}} \quad (21)$$

or

$$a = \frac{f_S}{1+f_S} \quad (22)$$

Solving Equation 22 for f_S gives:

$$f_S = \frac{a}{1-a} \quad (23)$$

Expressing Equation 15 in terms of the SWCNT volume fractions, the in-plane (parallel) thermal conductivity for Case 1 is:

$$\lambda_{Case\ 1,\ in-plane} = \frac{\lambda_2 f_s + \lambda_1}{1+f_s} = \frac{\lambda_2 \frac{a}{1-a} + \lambda_1}{1+\frac{a}{1-a}} = \frac{\frac{\lambda_2 a + \lambda_1(1-a)}{1-a}}{\frac{1-a+a}{1-a}} = \frac{\lambda_2 a + \lambda_1(1-a)}{1} = \lambda_2 a + \lambda_1(1-a) \quad (24)$$

or

$$\lambda_{Case\ 1,\ in-plane} = \lambda_{SWCNT} a + \lambda_{IM7}(1-a) \quad (25)$$

Expressing Equation 20 in terms of the SWCNT volume fractions, the through-thickness (series) thermal conductivity for Case 1 is:

$$\lambda_{Case\ 1,\ through-plane} = \frac{(1+f_s)\lambda_2\lambda_1}{\lambda_2+\lambda_1 f_s} = \frac{(1+\frac{a}{1-a})\lambda_2\lambda_1}{\lambda_2+\lambda_1\frac{a}{1-a}} = \frac{\frac{(1-a+a)\lambda_2\lambda_1}{1-a}}{\frac{\lambda_2(1-a)+\lambda_1 a}{1-a}} = \frac{\lambda_2\lambda_1}{\lambda_2(1-a)+\lambda_1 a} = \frac{\lambda_2\lambda_1}{\lambda_2 - a(\lambda_2-\lambda_1)} \quad (26)$$

or

$$\lambda_{Case\ 1,\ through-plane} = \frac{\lambda_{SWCNT}\lambda_{IM7}}{\lambda_{SWCNT} - a(\lambda_{IM7}-\lambda_{SWCNT})} \quad (27)$$

A similar method can be used to develop expressions for predicting the in-plane and through-plane thermal conductivities for a sample based on their SWCNT volume fraction. The extension of this approach to Case 2 requires the inclusion of parameters to define the spacing of the SWCNT and IM7 regions with the SWCNT-containing layer. For Case 2, the through-thickness resistance consists of a (upper) resistance, λ_{top} due to two resistances in

parallel, and a second (lower) resistance in series with each other. By analogy to Equation 15 for a parallel resistance, λ_{top} can be described by:

$$\lambda_{top} = \frac{\lambda_{SWCNT} f_L + \lambda_{IM7}}{1 + f_L} \tag{28}$$

with

$$f_L = \frac{L_2}{L_1} \tag{29}$$

Here, f_L provides a parameter that expresses the connectedness of the SWCNT regions within a layer.

For the total assembly, the overall thermal conductance through the top and bottom layers can be determined by analogy to Equation 20 for a series resistance to be,

$$\lambda_{Case\ 2,\ through-plane} = \frac{(1+f_s)\lambda_{IM7}\lambda_{top}}{\lambda_{top} + \lambda_{IM7} f_s} \tag{30}$$

Using the expression for λ_{top} from Equation 28 in Equation 30 gives

$$\lambda_{Case\ 2,\ through-plane} = \frac{(1+f_s)\lambda_{IM7}\frac{\lambda_{SWCNTs} f_L + \lambda_{IM7}}{1+f_L}}{\frac{\lambda_{SWCNTs} f_L + \lambda_{IM7}}{1+f_L} + \lambda_{IM7} f_s} = \frac{(1+f_s)\lambda_{IM7}(\lambda_{SWCNTs} f_L + \lambda_{IM7})}{\lambda_{SWCNTs} f_L + \lambda_{IM7} + \lambda_{IM7} f_s (1+f_L)} \tag{31}$$

For Case 2, the SWCNT volume fraction, *a*, is defined as the volume of the SWCNT regions divided by the total volume of the composite (SWCNT + IM7):

$$a = \frac{V_{SWCNT}}{V_{IM7}+V_{SWCNT}} = \frac{S_2L_2l}{(S_1(L_1+L_2)l+S_2L_1l)+S_2L_2l} = \frac{S_2L_2}{S_1L_1+S_1L_2+S_2L_2+S_2L_2} = \frac{S_2L_2}{(S_1+S_2)(L_1+L_2)} = \frac{\frac{S_2L_2}{S_1L_1}}{\left(1+\frac{S_2}{S_1}\right)\left(1+\frac{L_2}{L_1}\right)} \quad (32)$$

or

$$a = \frac{f_Sf_L}{(1+f_S)(1+f_L)} \quad (33)$$

using that $f_S = \frac{S_2}{S_1}$ and $f_L = \frac{L_2}{L_1}$.

For Case 2, the equation to describe the in-plane thermal conductance is easily obtained using arguments of symmetry In Figure 5.1–1, proceeding from top to bottom is similar to proceeding from left to right in terms that a parallel resistance due to SWCNT and IM7 regions is followed in series by a resistance by IM7. For Case 2 in Figure 5.1–1, switching L_1 for S_1 and L_2 for S_2 interconverts these two directionalities. As a result of this symmetry, replacing $\frac{L_2}{L_1}$ by $\frac{S_2}{S_1}$ (or f_L by f_S) and replacing $\frac{S_2}{S_1}$ by $\frac{L_2}{L_1}$ (or f_S by f_L) translates the expression in Equation 34 for through-plane thermal conductance into an expression for in-plane thermal resistance. The result of replacing f_L by f_S and replacing f_S by f_L is given below:

$$\lambda_{Case\ 2,\ \ in-plane} = \frac{(1+f_L)\lambda_{IM7}(\lambda_{SWCNT}f_S+\lambda_{IM7})}{\lambda_{SWCNT}f_S+\lambda_{IM7}+\lambda_{IM7}f_L(1+f_S)} \quad (34)$$

In short, using Equations 31 and 34 allow calculation of the influence of SWCNT content on the through-plane and in-plane λ's assuming values of f_S or f_L. From experimental

measurements, the SWCNTs added a finite thickness to each layer of the composite that could vary for different loading parameters. The IM7 prepreg composite is an anisotropic material that exhibits directionally dependent values of thermal transport along the in-plane and through-thickness directions. In essence, IM7 yields different values for thermal diffusivity (α) and thermal conductivity (λ) in both the in-plane and through-thickness directions.

5.2 THEORETICAL MODEL CALCULATIONS

In the previous section, two cases were presented for modeling the thermal transport properties of the IM7/SWCNT hybrid composites (Figure 5.1-1). Case 1 considered the structure to consist of continuous alternating layers of IM7 and SWCNTs. Case 2 considered the SWCNT layers to lack in-plane continuity. To distinguish between these two cases, microscopy was performed on cross-sectional slices of various IM7/SWCNT specimens.

Figure 5.2-1 shows optical images for three 12-ply IM7/SWCNT hybrid composite samples with different volume fractions of SWCNTs. In these images, the white circular features (diameter of ~ 5 um) are the carbon fibers within the IM7 composite, darker regions are observed for the resin within the IM7 composite regions and for the SWCNT layers, and black regions correspond to gaps between two plies. Despite the similarity in their brightness, the SWCNT layers can be differentiated from the resin by the absence of the carbon fibers from their regions.

Figure 5.2-1a shows a low magnification image for the sample containing the lowest volume fraction of SWCNTs. In this image, there are thin SWCNT layers between each of the uni-directional plies as well as the presence of small voids, which are assumed to be small pockets of air that get trapped during stacking between the layers of prepreg composite. The

boundaries between the IM7/SWCNT layers correspond to the actual hand layup scheme as illustrated in Figure 4.3-2. The nominal thicknesses of the IM7 sheets that form each layer are 5 mils (~0.005 in) according to its supplier (Hexcel Inc.), or ~120 μm, In Figure 5.2-1a, the repeat distance between SWCNT layers appears to be ~100 μm, in accord with the supplier values. The differences between these values may be due to compaction during the lay up process and curing. Although the SWCNT layer in this sample with a low SWCNT volume fraction appears irregular in its thickness, it displays a high degree of lateral connectedness, suggesting the presence of a SWCNT layer that is more continuous than as isolated domains.

(a)

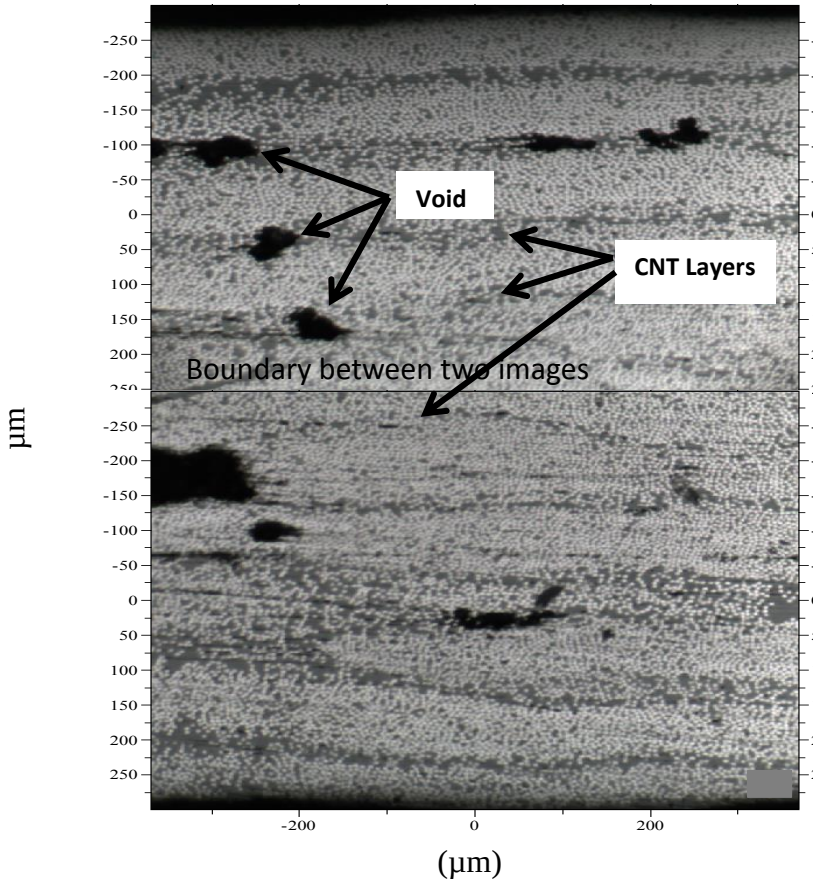

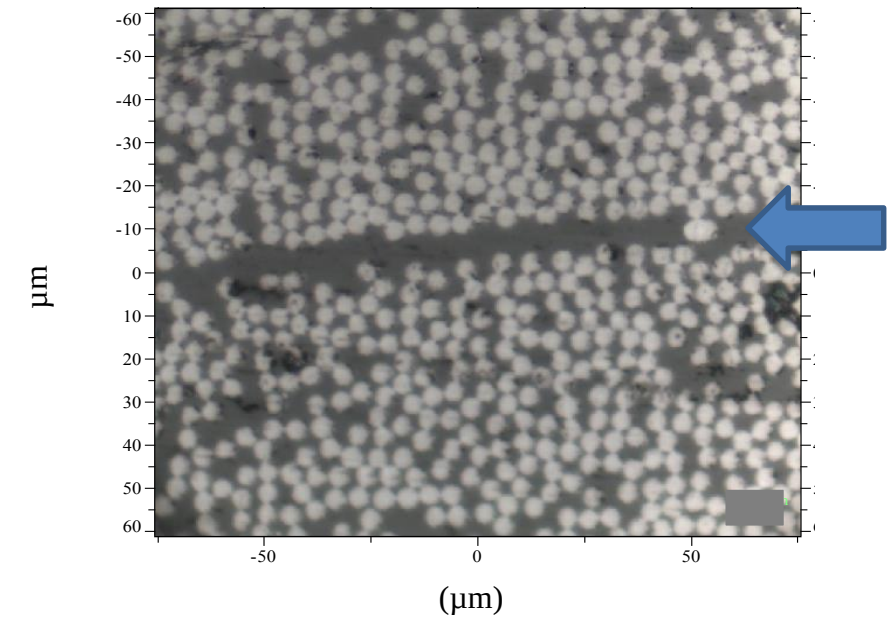

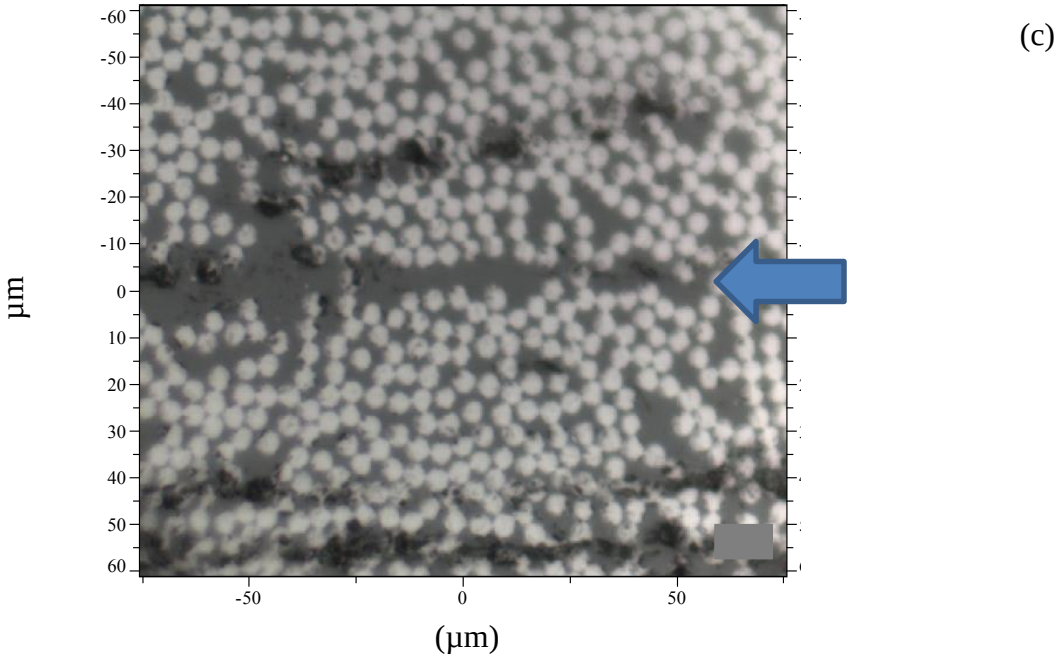

Figure 5.2–1a–c. Optical microscopy images of three 12-ply IM7/SWCNT hybrid composites (volume fractions of 0.01, 0.19 and 0.32, respectively). The images show the presence of voids and stratified SWCNT layers in the IM7/SWCNT composite.

Figures 5.2–1b and 5.2-1c show images at higher magnification for specimens containing higher volume fractions of the SWCNTs. In these samples, the SWCNT layers appear at a single band roughly 5 to 10 μm in thickness between the IM7 layers. The separation between the upper and lower layers IM7 (indicated by the arrows) show a definable separation between one ply versus another. The white circles are cross-sections of the cylindrical carbon fibers, which are approximately 5 μm in diameter and tightly packed in the epoxy matrix. These circles are only weakly visible in Figure 5.2-1a because of its lower magnification. In Figures 5.2-1b and c, the aperture was set to capture the interface between two individual plies rather than the entire 12-ply specimen as done in Figure 5.2-1a. As a result, the individual carbon fibers are more readily resolved in the latter two images. It is possible that the SWCNTs may have diffused in the PAN expoxy during curing and dispersed into the IM7 composite. This possibilit cannot be ignored as it is difficult to visibly distinguish the SWCNT particulates between the IM7 plies from the resin comprising the IM7 in the images directly. The regions lacking the white circles do provide evidence for a separation between adjacent IM7 layers as seen from the microscopy images. Further, these small bands were observed between each ply, and the images show that as the volume fraction for the SWCNT increases, the thickness of that identified as due to the SWCNT layers also increases across the composite. With regard to the two developed models in the preceding section, the images provide strong evident that Case 1 is the more suitable scenario because the SWCNTs appeared as distinct bands between the IM7 layers in the optical images.

The equations developed for the Case 1 model were used to predict the heat capacities (C_p), the thermal conductivities (λ), and the in-plane and through-thickness of the thermal diffusivities (α) for the IM7/SWCNT composites for various volume fractions for the SWCNTs in the composites. These predictions rely on property data for SWCNTs and the IM7, and

Table 5.2–1 summarizes the properties for IM7 and SWCNTs at 300 K that were used in the model. As noted earlier, the heat capacity (C_p) for IM7 can vary due to the age of the prepreg composite. For example, in my experimental data, C_p varied from 760 to 1000 J/kg-K for IM7. As such variations in C_p will affectthe overall thermal conductivities of a composite, three values for C_p (750, 860 and 1000 J/kg–K, representing old, moderately aged, and fresh IM7, respectively, as contained in Table 5.2-1) were used to provide predictions on how the properties of IM7/SWCNT composites might be expected to vary. For these predictions, the S_1 slice was kept constant at 0.005 in and the S_2 slice was modeled as having a thickness that scaled with the volume fraction of the SWCNTs in the composite sample. Using Equation 18 and the parameters in Table 5.2-1, SWCNT volume fractions as high as 0.75 were examined.

Table 5.2–1. Thermal properties of IM7 and SWCNT at 300 K.

Property	**IM7**	**SWCNTs**
ρ (kg/m^3)	1577.82	1550
C_p (J/kg-K)	750 or 860 or 1000*	600
$\alpha_{in\text{-}plane}$ (cm^2/s)	0.025	0.538
$\alpha_{through\text{-}thickness}$ (cm^2/s)	0.00451	0.538
$\lambda_{in\text{-}plane}$ (W/m-K) –	3.36	50
$\lambda_{through\text{-}thickness}$ (W/m-K)	0.58 or 0.66 or 0.77*	50

*See Page 94.

Table 5.2–2 shows experimental results for IM7/SWCNT composites at 300 K, as presented in Chapter 4. As noted previously, varying the SWCNT content in the isopropyl alcohol dispersion used to apply the SWCNTs to the IM7 plies did not lead to direct changes to the deposited thickness of SWCNTs on the surface of the prepreg composite. For this reason, the determined mass and volume fractions of SWCNTs in the IM7/SWCNT composites were used as the primary measures of SWCNT content for comparing the predicted and

experimental results. Overall, within experimental error, the values obtained from samples sprayed with the SWCNT dispersion exhibited higher C_p, and through-thickness α and λ values versus those for virgin IM7.

Table 5.2–2. Experimental results for IM7/SWCNT composites at 300 K with mean standard deviations.

SWCNT wt% in IPA Dispersion	**CNT Volume Fraction in CNT/IM7 Composite** $\left(\frac{V_{CNT}}{V_{IM7}+V_{CNT}}\right)$	**CNT Mass Fraction CNT/IM7 Composite** $\left(\frac{M_{CNT}}{M_{IM7}+M_{CNT}}\right)$	**ρ (kg/m^3)**	**C_p (J/kg-K)**	**$\alpha_{through\text{-}thickness}$ (cm^2/s)**	**$\lambda_{through\text{-}thickness}$ (W/m-K)**
Virgin	0	0	1572 ± 10	760 ± 30	0.0049 ± 0.0001	0.60 ± 0.05
0.007	0.0107± 0.0008	0.01233 ± 0.00005	1579 ± 2	925 ± 20	0.0048 ± 0.0002	0.70 ± 0.04
0.009	0.062 ± 0.002	0.0616 ± 0.0006	1570 ± 4	950 ± 20	0.0050 ± 0.0002	0.74 ± 0.03
0.02	0.244 ± 0.005	0.243 ± 0.004	1570 ± 30	855 ± 10	0.0060 ± 0.0001	0.80 ± 0.02
0.04	0.188 ± 0.004	0.193 ± 0.008	1590 ± 10	820 ± 40	0.0059 ± 0.0004	0.76 ± 0.05
0.06	0.264 ± 0.004	0.272 ± 0.008	1573 ± 10	800 ± 25	0.0068 ± 0.0001	0.86 ± 0.03
0.08	0.257 ± 0.013	0.254 ± 0.008	1585 ± 10	830 ± 34	0.0060 ± 0.0004	0.79 ± 0.06
0.1	0.32 ± 0.02	0.32 ± 0.02	1570 ± 30	870 ± 15	0.0063 ± 0.0004	0.86 ± 0.06

Figures 5.2–2 through 5.2–5 show the predicted and experimental values of ρ, C_p, through-thickness α, and through-thickness λ for the IM7/SWCNT composites. These figures consider the effects of variations in C_p values on ρ, through-thickness α, and through-thickness λ. As stated earlier, the C_p of IM7 is affected by its age, where its value decreases as the age of the thermoset increases. The cases that were modeled include the use C_p values of 750, 860, and 1000 J/kg–K, representing oldest, medium, and newest IM7 samples, respectively.

For ρ, values for the composites were modeled as a weighted sum on a thickness basis (or more correctly, on a volume basis where volume = thickness * area, and the areas cancel) given by:

$$\rho_{composite} = \frac{\rho_1 t_1 + \rho_2 t_2}{t_1 + t_2} \quad (35)$$

where ρ_1, t_1, ρ_2, and t_2 are the densities and layer thicknesses of the IM7 and SWCNTs, respectively.

For C_p, the values for the composite were modeled as a weighted sum on a mass basis (where mass = density * thickness * area, and the areas cancel) given by:

$$C_{p,composite} = \frac{\rho_1 t_1 C_{p1} + \rho_2 t_2 C_{p2}}{\rho_1 t_1 + \rho_2 t_2} \quad (36)$$

where ρ_1, t_1, C_{p1}, ρ_2, t_2, and C_{p2} are the densities, layer thicknesses, and heat capacities of the IM7 and SWCNTs, respectively.

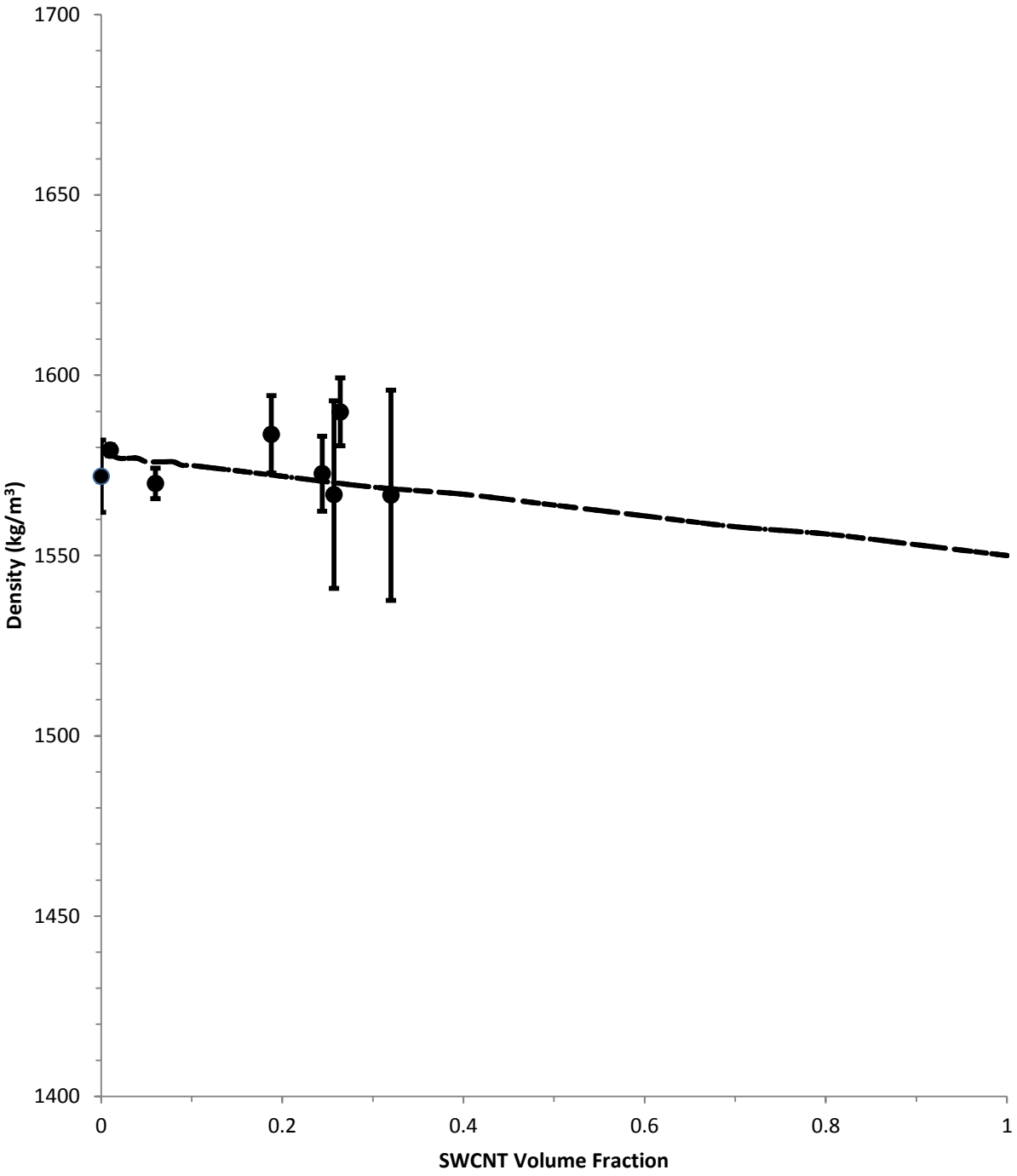

Figure 5.2–2. Predicted and experimental densities of IM7/SWCNT composites at 300 K.

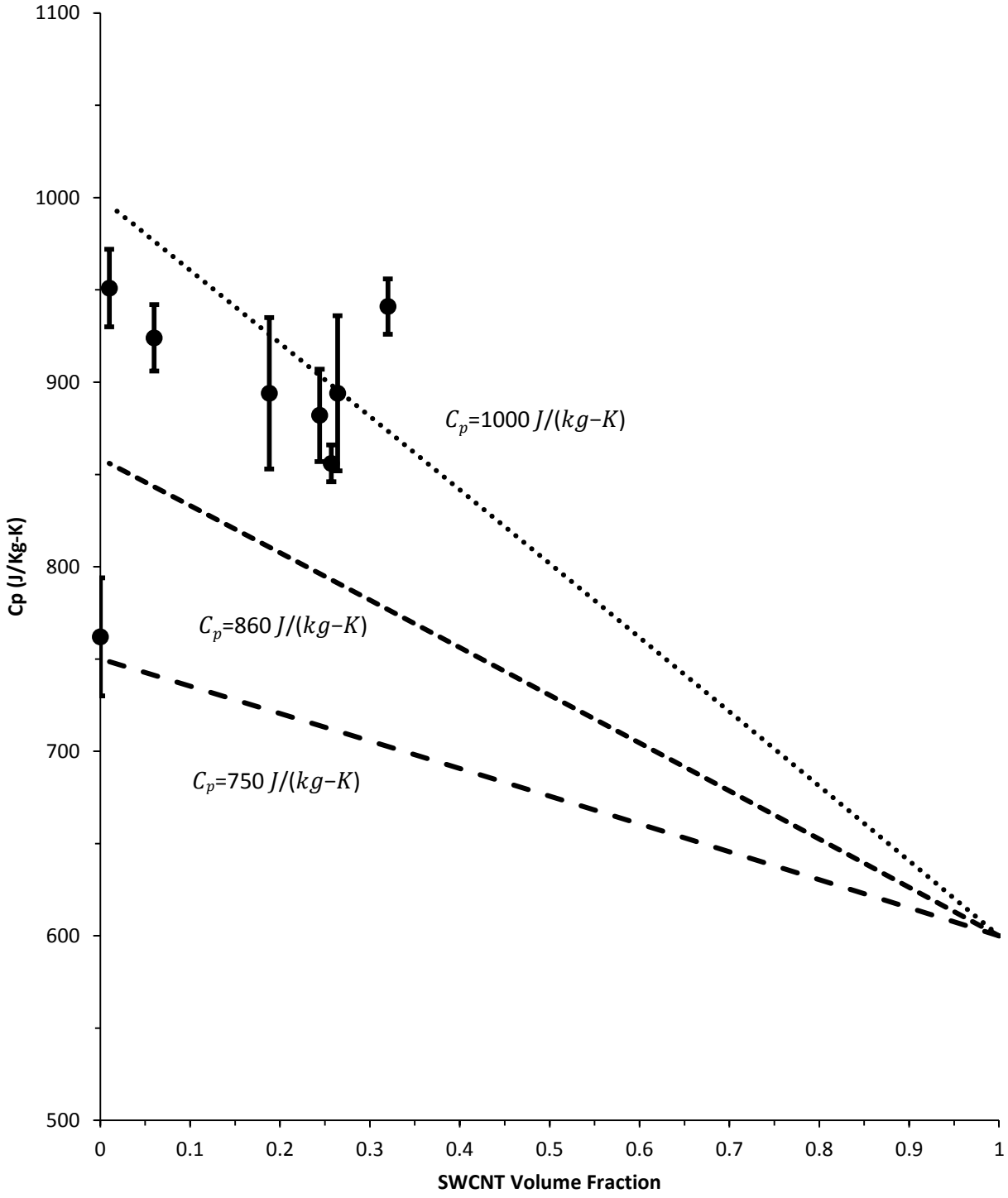

Figure 5.2–3. Predicted and experimental heat capacities (C_p) of IM7/SWCNT composites at 300 K. The predicted heat capacities are displayed as dashed lines using C_p values of 750, 860, and 1000 J/kg–K for oldest, moderately aged, and fresh IM7, respectively, at 300 K.

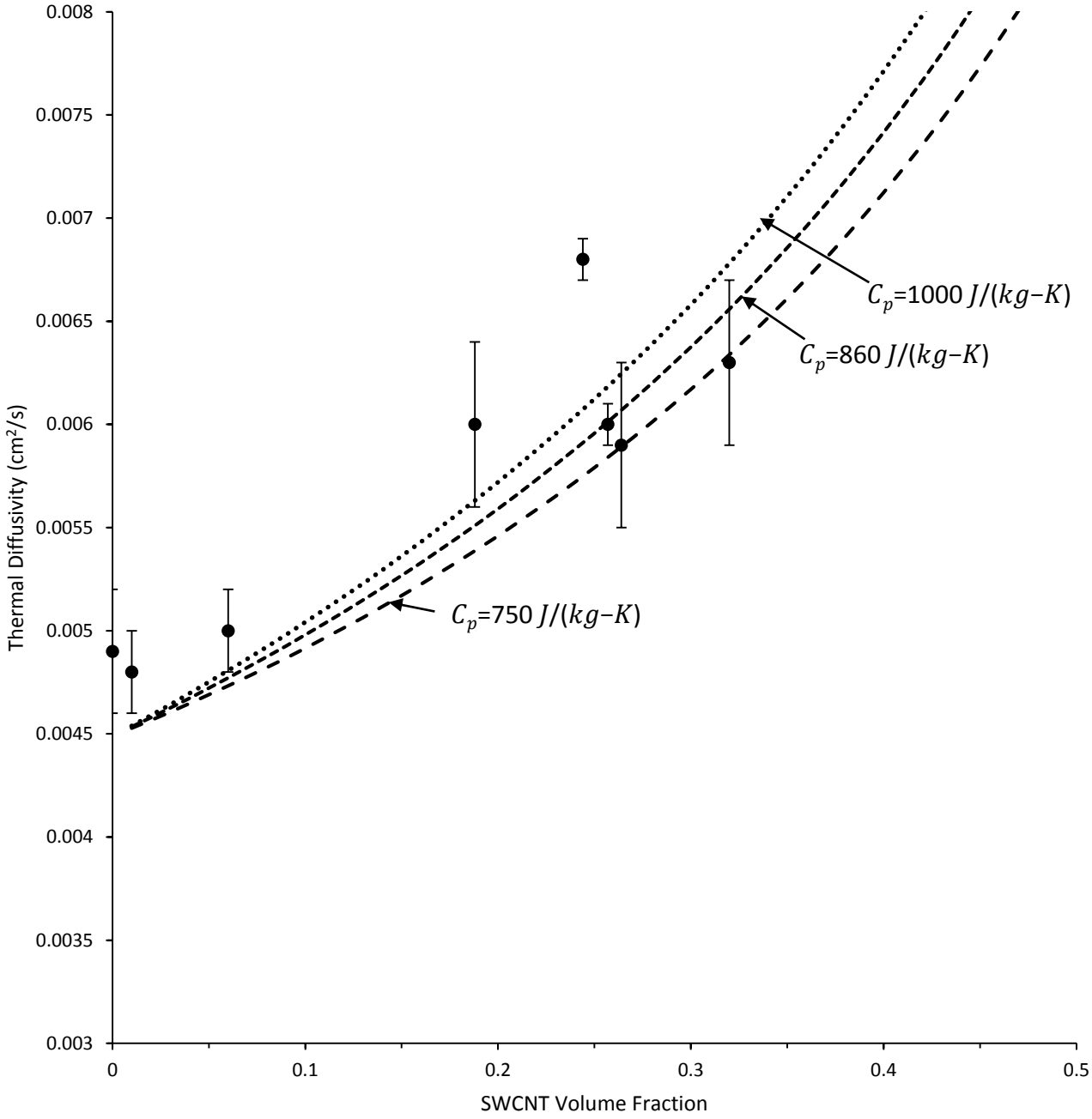

Figure 5.2–4. Predicted and experimental through-thickness thermal diffusivities of IM7/SWCNT composites at 300 K. The predicted thermal diffusivities are displayed as dashed lines using values for C_p of 750, 860, and 1000 J/kg–K for oldest, moderately aged, and fresh IM7, respectively, at 300 K.

Figure 5.2–5 shows predicted values for the through-thickness λ of the IM7/SWCNT composite at various SWCNT compositions. Three sets of predicted results are displayed, using C_p values of 750, 860 and 1000 J/kg–K for IM7 to compensate for the effects of storage on the properties of IM7. Within experimental error, the experimentally obtained data are well described within the range of predicted values for these various C_p values for IM7.

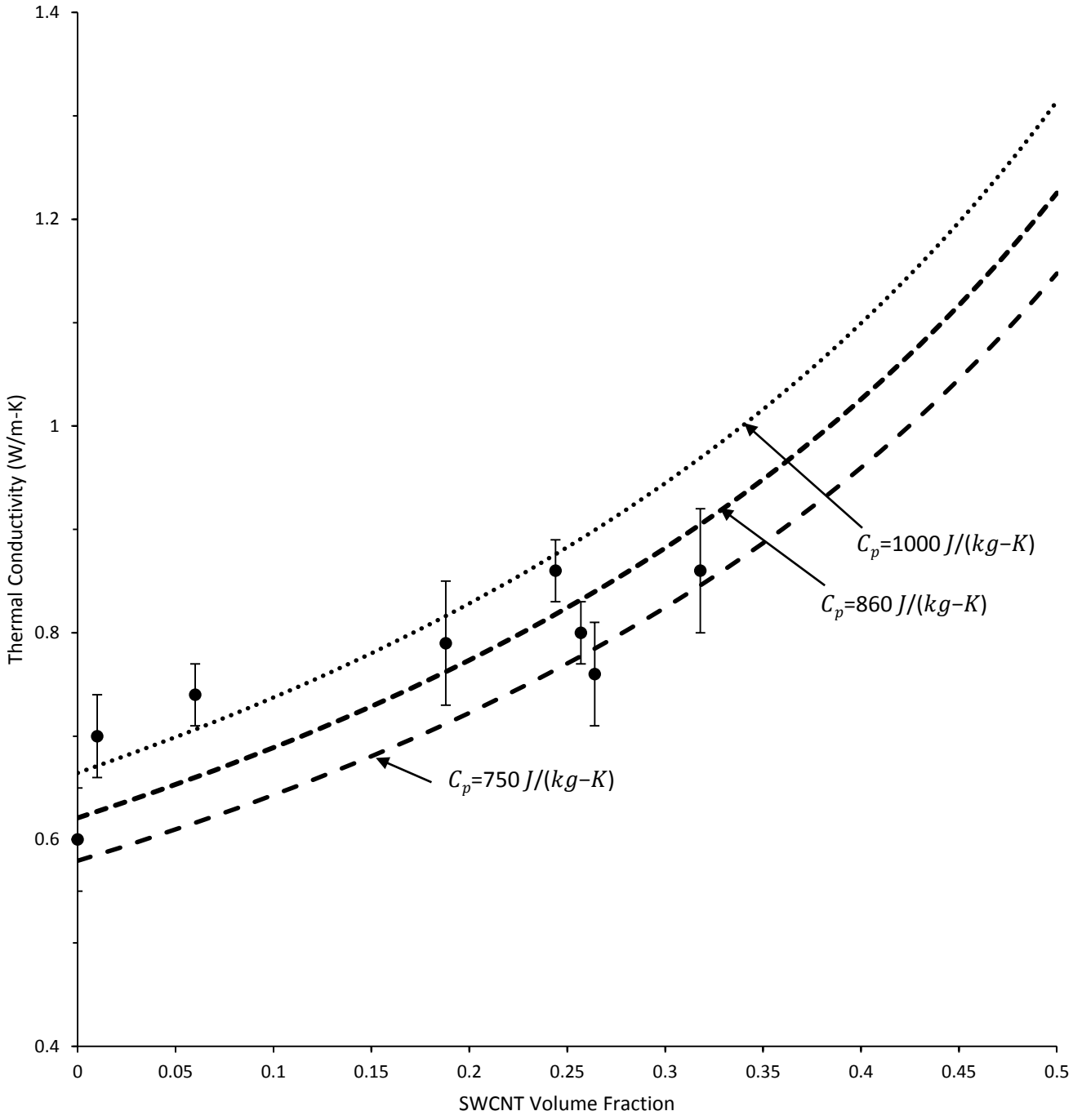

Figure 5.2–5. Predicted and experimental through-thickness thermal conductivities for IM7/SWCNT composites at 300 K. The predicted thermal conductivities are displayed as dashed lines using C_p values of 750, 860, and 1000 J/kg–K for oldest, moderately aged, and fresh IM7, respectively, at 300 K.

Figures 5.2–6 and 5.2–7 show the predicted values for the in-plane and through-thickness α and λ, respectively, again considering the range of potential C_p values for IM7 at 300 K. Experimentally, it is difficult to measure the in-plane values for IM7 as it is an anisotropic material having values in–plane that are above those readily obtained by available instruments for samples with overall thicknesses such as those prepared. Such measurements could be possible by using much thicker specimens; however, such samples are difficult to prepare in practice and were not pursued. Instead, the predictions provide estimates of the improvements in the through-thickness and in-plane thermal diffusivities and thermal conductivities that can be expected. Of these, the predictions can be validated for the through-thickness results, which provide some support for the in-plane predicted values.

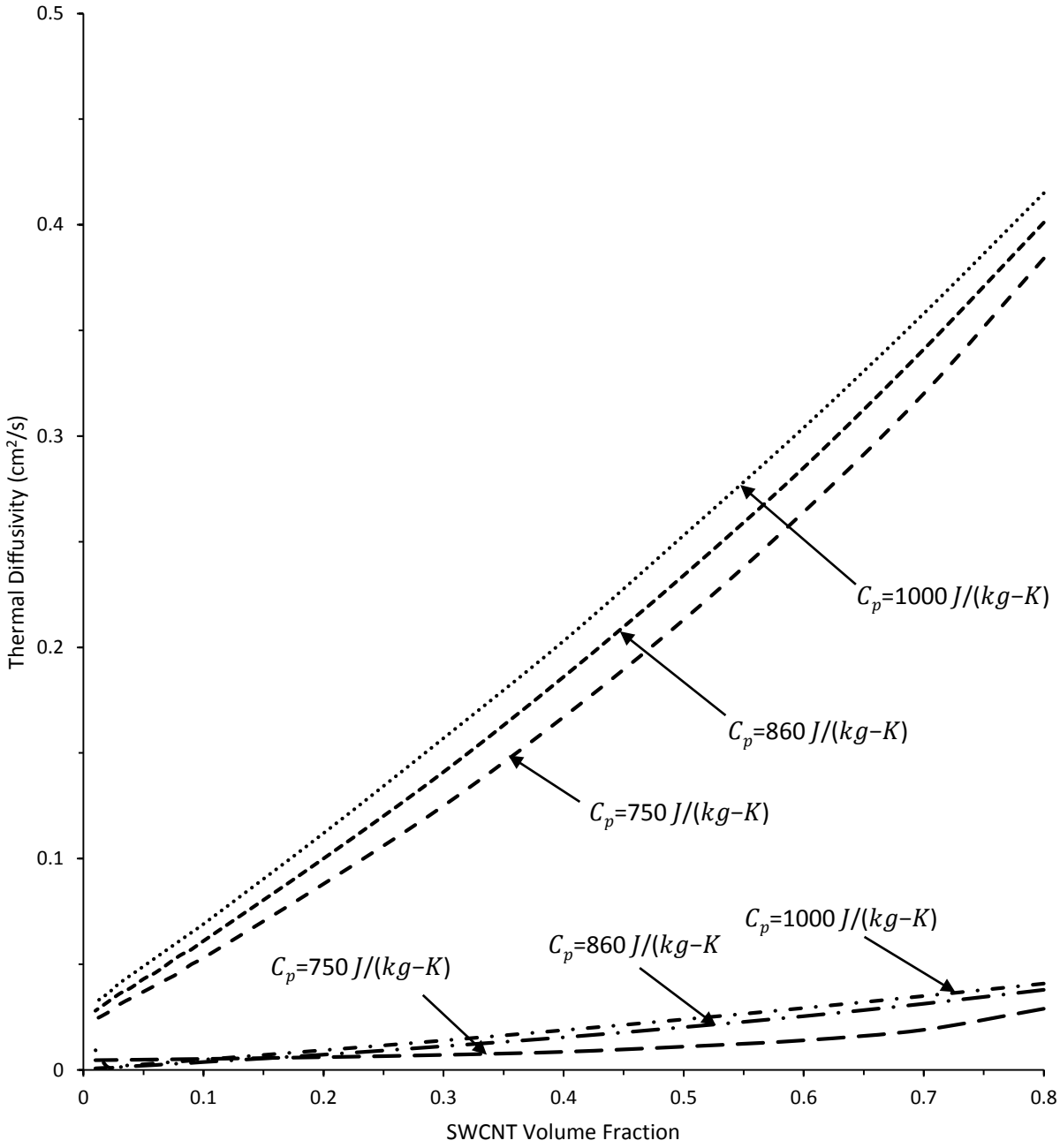

Figure 5.2–6. Predicted in-plane and through-thickness thermal diffusivities for IM7/SWCNT composites at 300 K. The predicted thermal diffusivities are displayed as dashed lines using C_p values of 750, 860, and 1000 J/kg–K for oldest, moderately aged, and fresh IM7, respectively, at 300 K. The thermal diffusivities are higher in-plane than through-thickness.

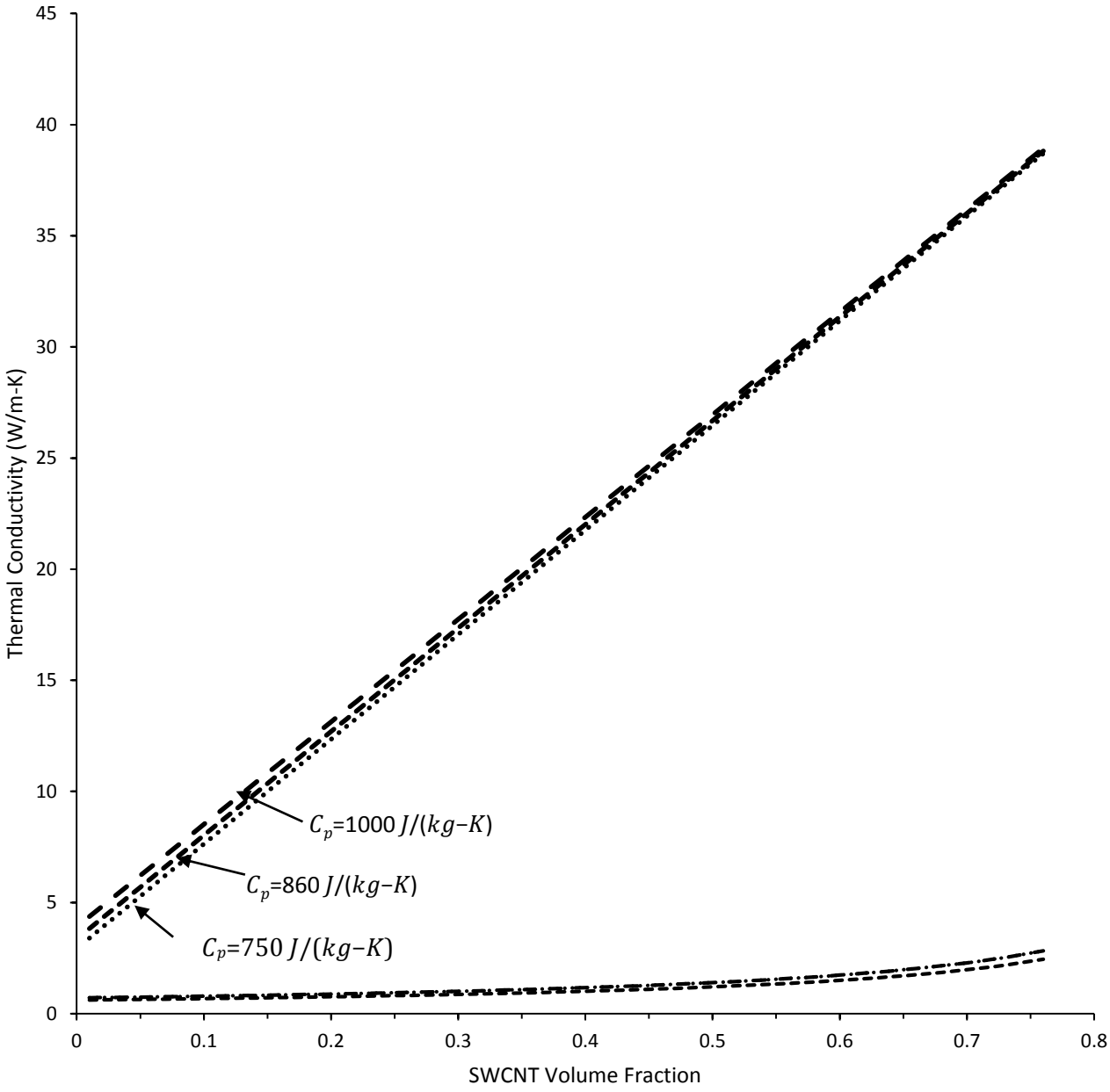

Figure 5.2–7. Predicted in-plane and through-thickness thermal conductivities for IM7/SWCNT composites at 300 K. The predicted thermal conductivities are displayed as dashed lines using C_p values of 750, 860, and 1000 J/kg–K for oldest, moderately aged, and fresh IM7, respectively, at 300 K. The thermal conductivities are higher in-plane than through-thickness.

Figures 5.2–8 through 5.2–15 compare the predicted and experimental through-thickness λ values for IM7/SWCNT composites at all explored temperatures. The predicted values for the IM7/SWCNT composites depend directly on the C_p values for IM7 and the SWCNTs at these temperatures. As values for C_p over the range of explored temperatures were not available for IM7 from the supplier (Hexcel, Inc.), I employed a best fit to the experimental C_p values obtained from virgin IM7 specimens. Using these experimental values, a linear fit to the data yielded the general expression for C_p (in J/kg-K) = 2.7376*Temperature (in degrees Kelvin) – 12.487, with an R^2 value of 0.9979. This fitting equation was adjusted to provide to provide values for C_p at 300 K corresponding to those for oldest, modestly aged, and fresh IM7 specimens. Specifically, multiplicative factors of 0.927, 1.063, and 1.236, respectively, were applied to this equation to yield values for C_p at 300 K of 750, 860, and 1000 J/kg–K, respectively. The resulting expressions for the heat capacity for IM7 with temperature were:

$$C_{p,oldest\ IM7}\ (\text{in J/kg-K}) = 2.5378*\text{Temperature (in degrees Kelvin)} - 11.575, \quad (37)$$

$$C_{p,modestly\ aged\ IM7}\ (\text{in J/kg-K}) = 2.9101*\text{Temperature (in degrees Kelvin)} - 13.274, \quad (38)$$

and

$$C_{p,fresh\ IM7}\ (\text{in J/kg-K}) = 3.3837*\text{Temperature (in degrees Kelvin)} - 15.434. \quad (39)$$

Equations 37 to 39 were used to provide estimates for the range of C_p values for IM7 in Figures 5.2–8 through 5.2–15.

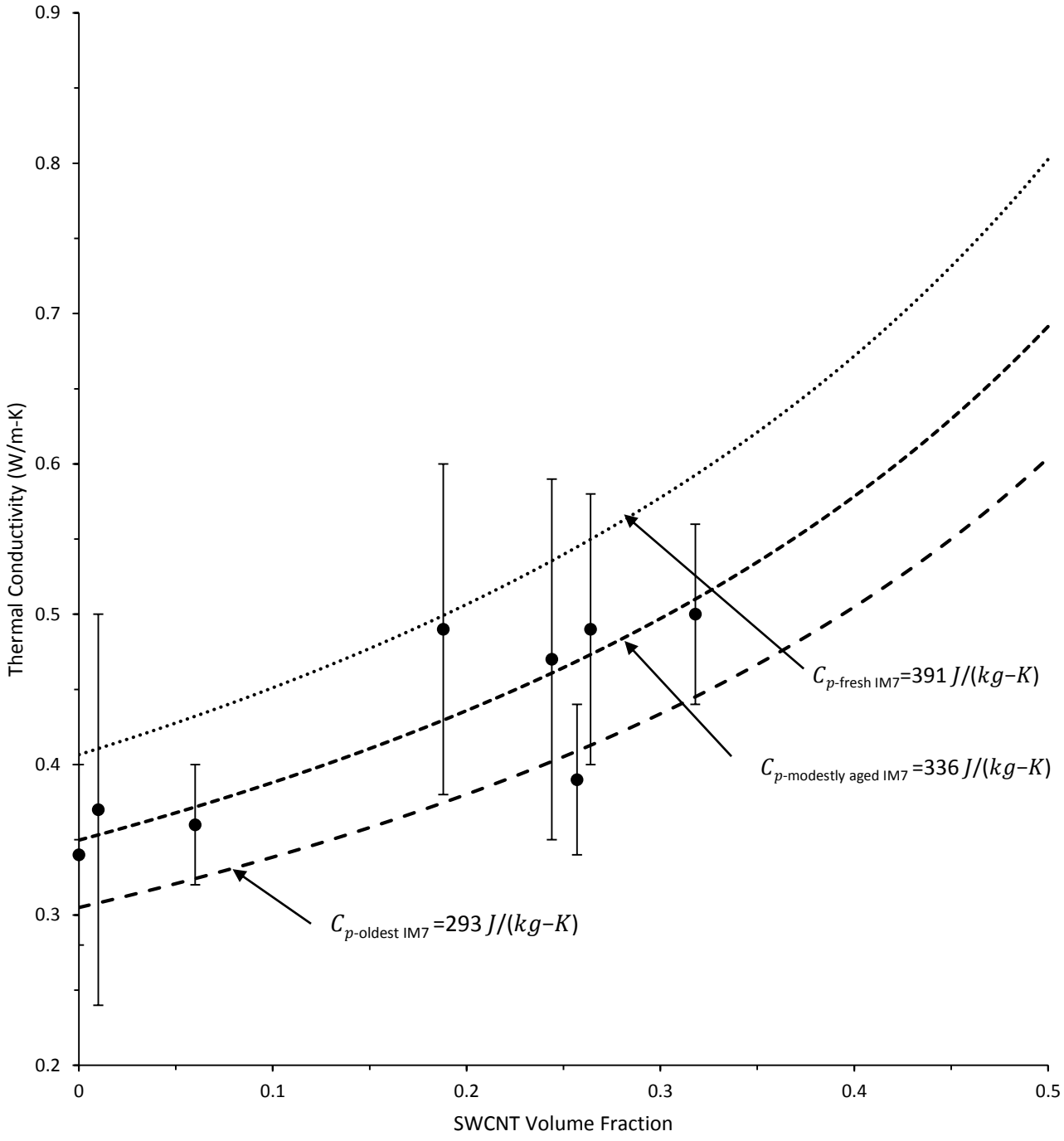

Figure 5.2–8. Predicted and experimental results of through-thickness thermal conductivities for IM7/SWCNT composites at 120 K. The predicted thermal conductivities are displayed as dashed lines using C_p values of 293, 336, and 391 J/kg–K as estimated for oldest, moderately aged, and fresh IM7, respectively, at 120 K by equations 37 to 39.

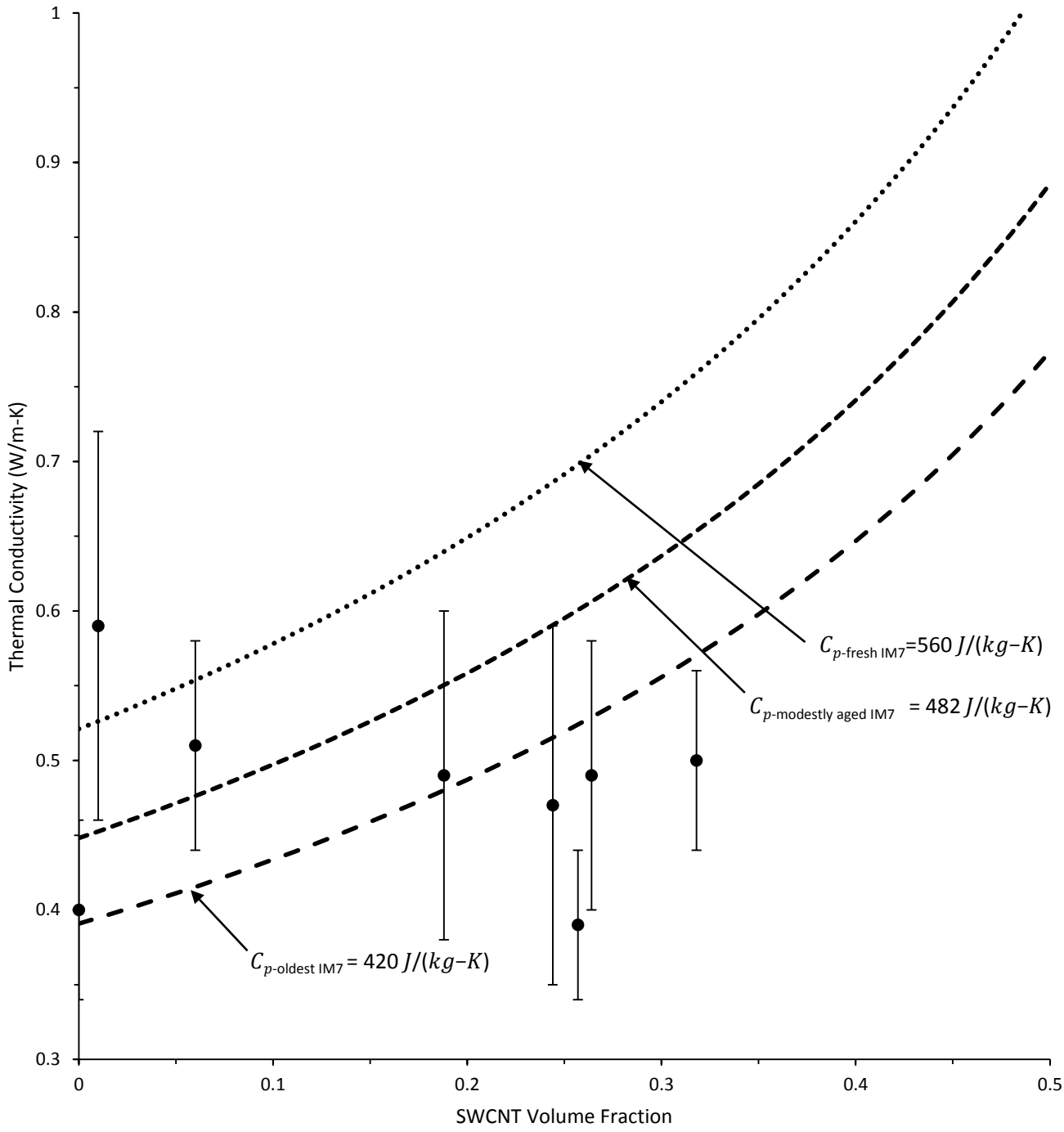

Figure 5.2–9. Predicted and experimental through-thickness thermal conductivities for IM7/SWCNT composites at 170 K. The predicted thermal conductivities are displayed as dashed lines for C_p values of 420, 482, and 560 J/kg–K as estimated for oldest, moderately aged, and fresh IM7, respectively, at 170 K by equations 37 to 39.

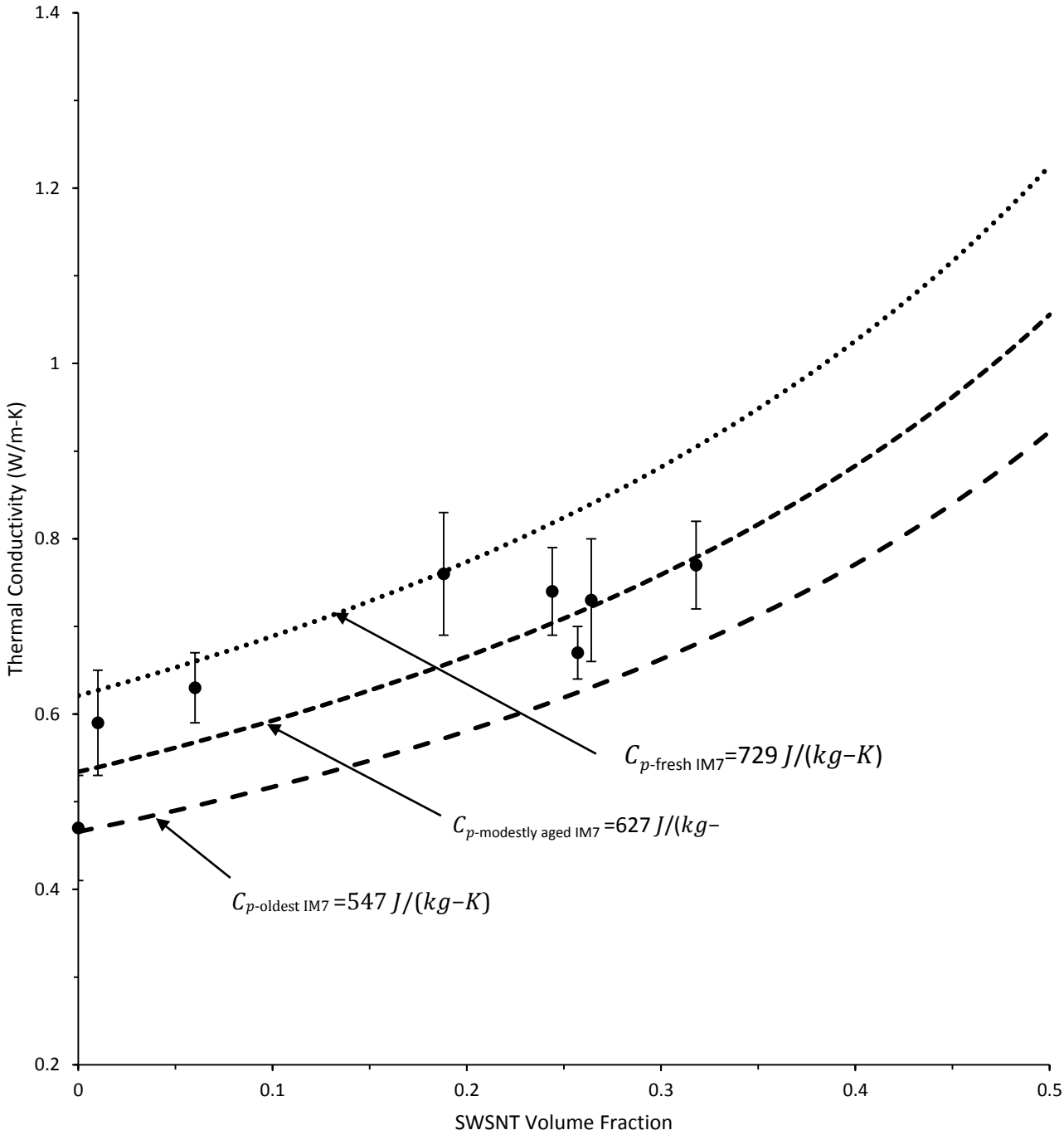

Figure 5.2–10. Predicted and experimental through-thickness thermal conductivities for IM7/SWCNT composites at 220 K. The predicted thermal conductivities are displayed as dashed lines for C_p values of 547, 627, and 729 J/kg–K as estimated for oldest, moderately aged, and fresh IM7, respectively, at 220 K by equations 37 to 39.

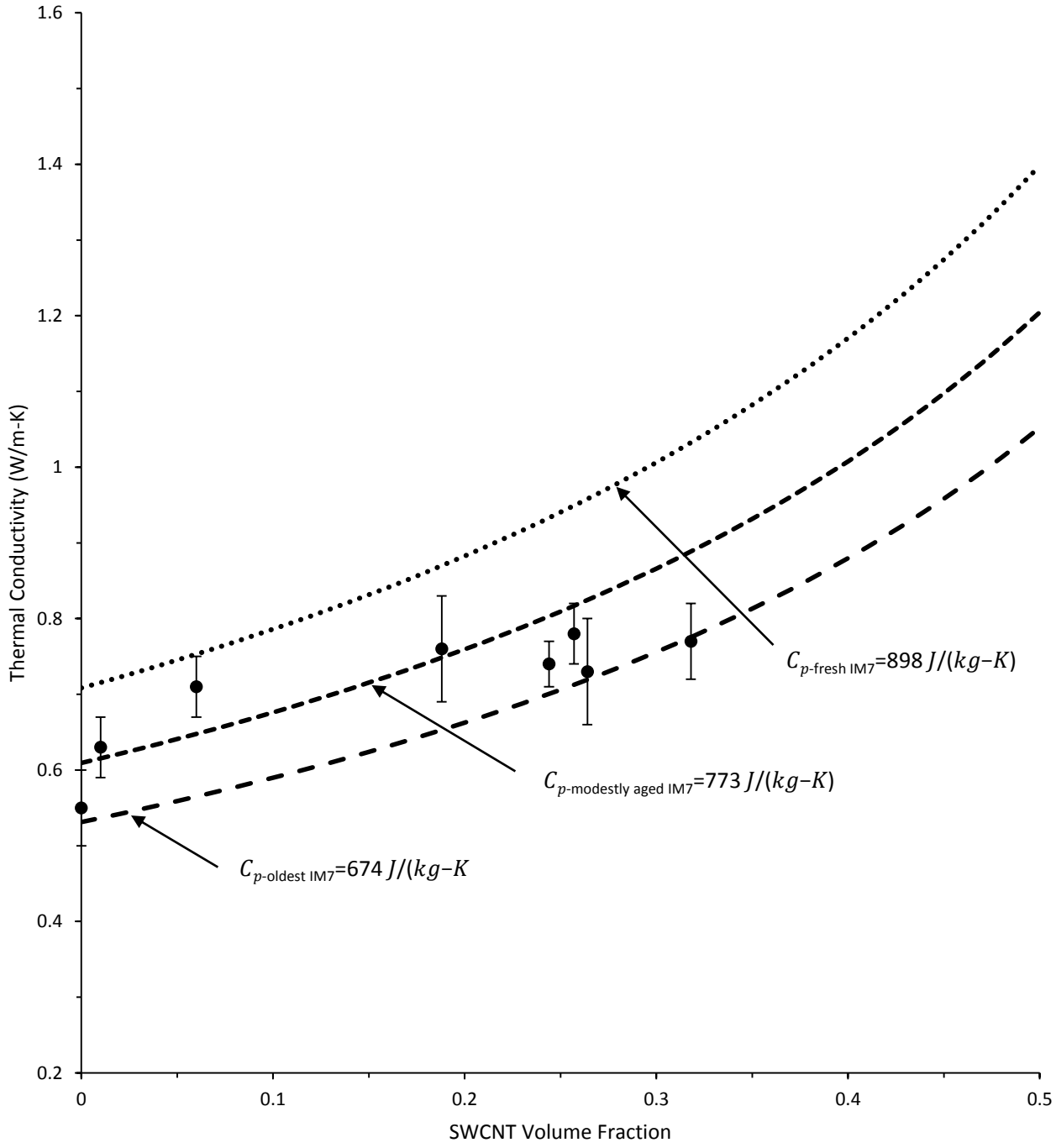

Figure 5.2–11. Predicted and experimental through-thickness thermal conductivities for IM7/SWCNT composites at 270 K. The predicted thermal conductivities are displayed as dashed lines for C_p values of 674, 773, and 898 J/kg–K as estimated for oldest, moderately aged, and fresh IM7, respectively, at 270 K by equations 37 to 39.

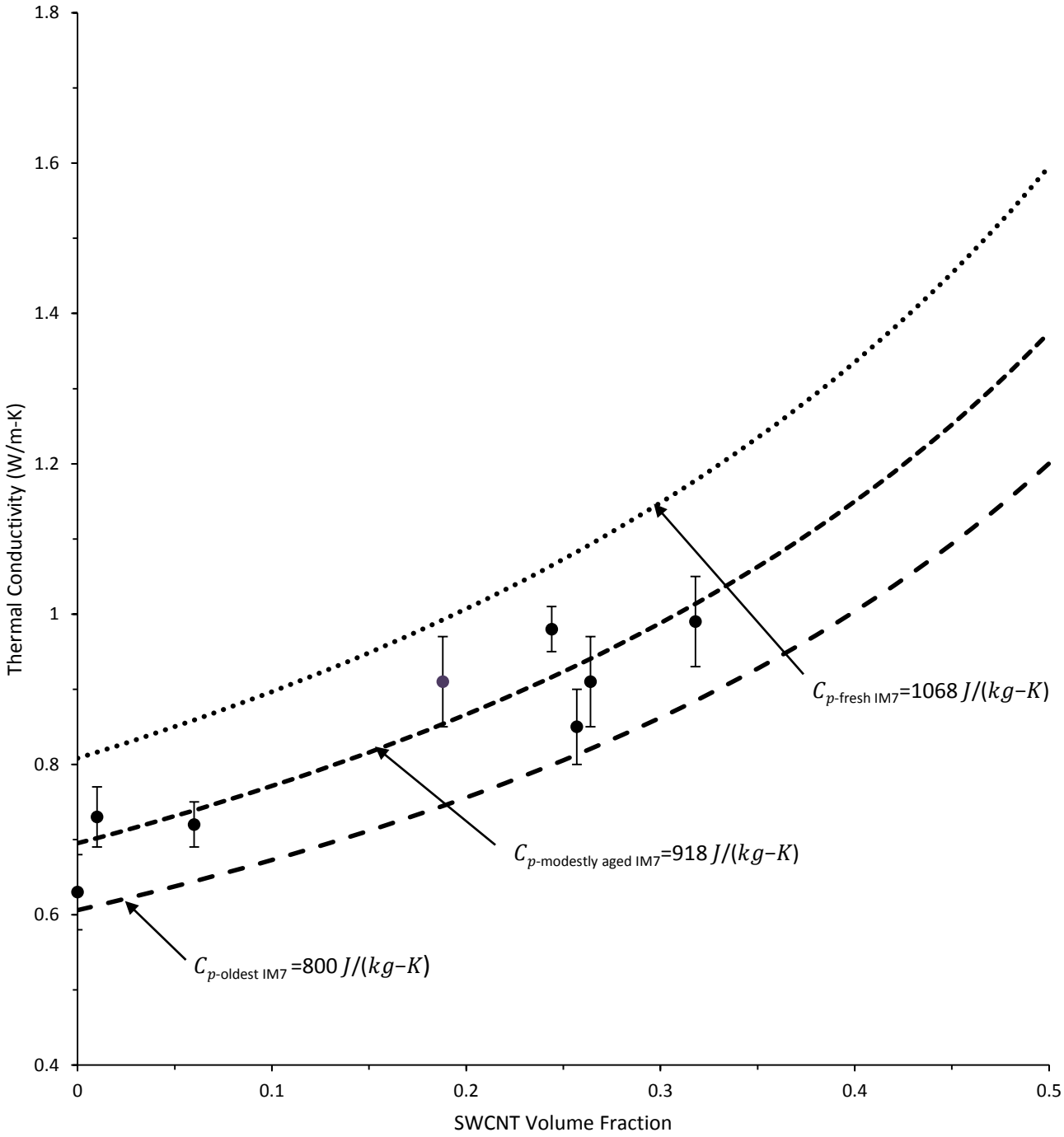

Figure 5.2–12. Predicted and experimental through-thickness thermal conductivities for IM7/SWCNT composites at 320 K. The predicted thermal conductivities are displayed as dashed lines for C_p values of 800, 918, and 1068 J/kg–K as estimated for oldest, moderately aged, and fresh IM7, respectively, at 320 K by equations 37 to 39.

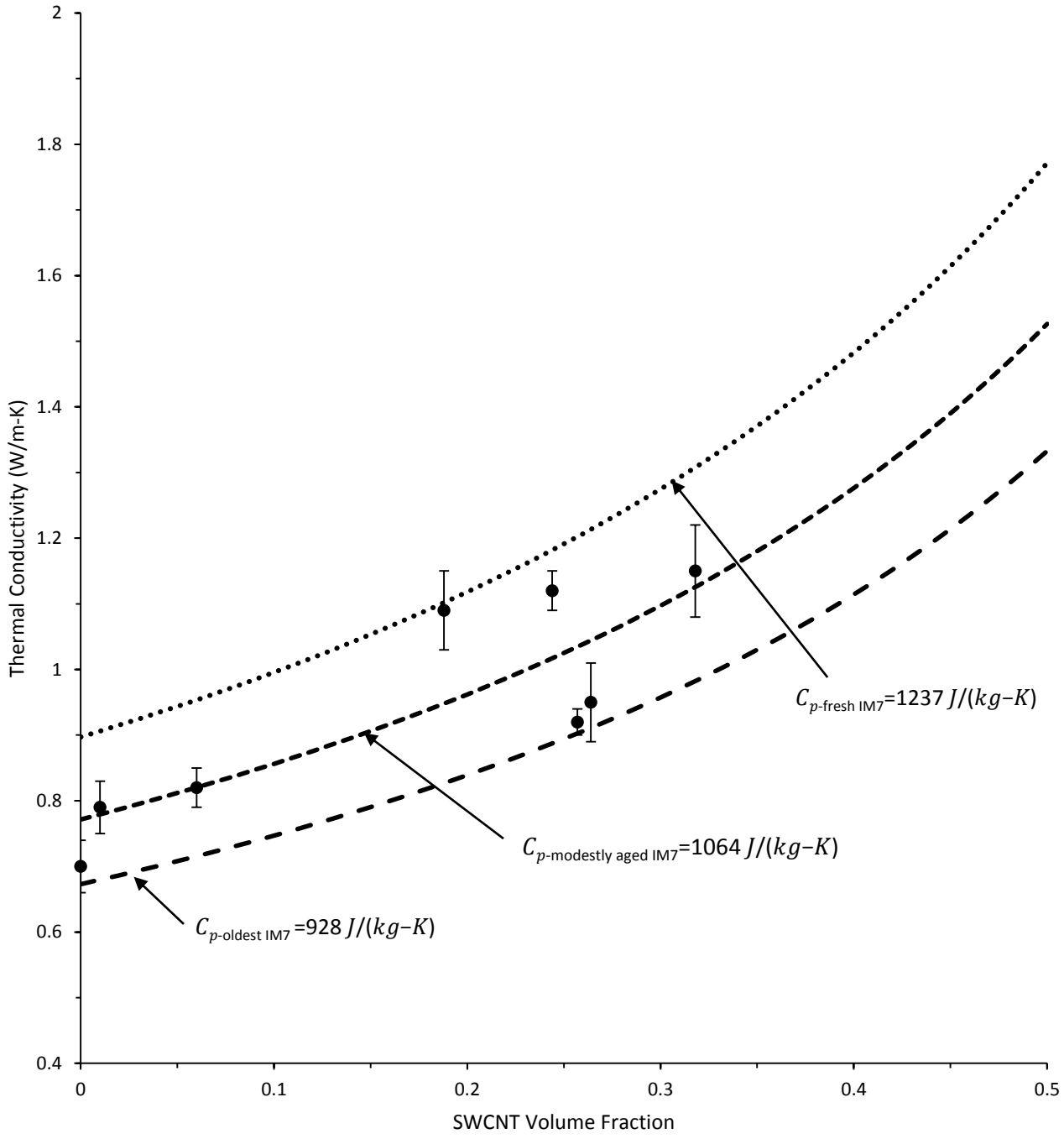

Figure 5.2–13. Predicted and experimental through-thickness thermal conductivities for IM7/SWCNT composites at 370 K. The predicted thermal conductivities are displayed as dashed lines for C_p values of 928, 1064, and 1237 J/kg–K as estimated for oldest, moderately aged, and fresh IM7, respectively, at 370 K by equations 37 to 39.

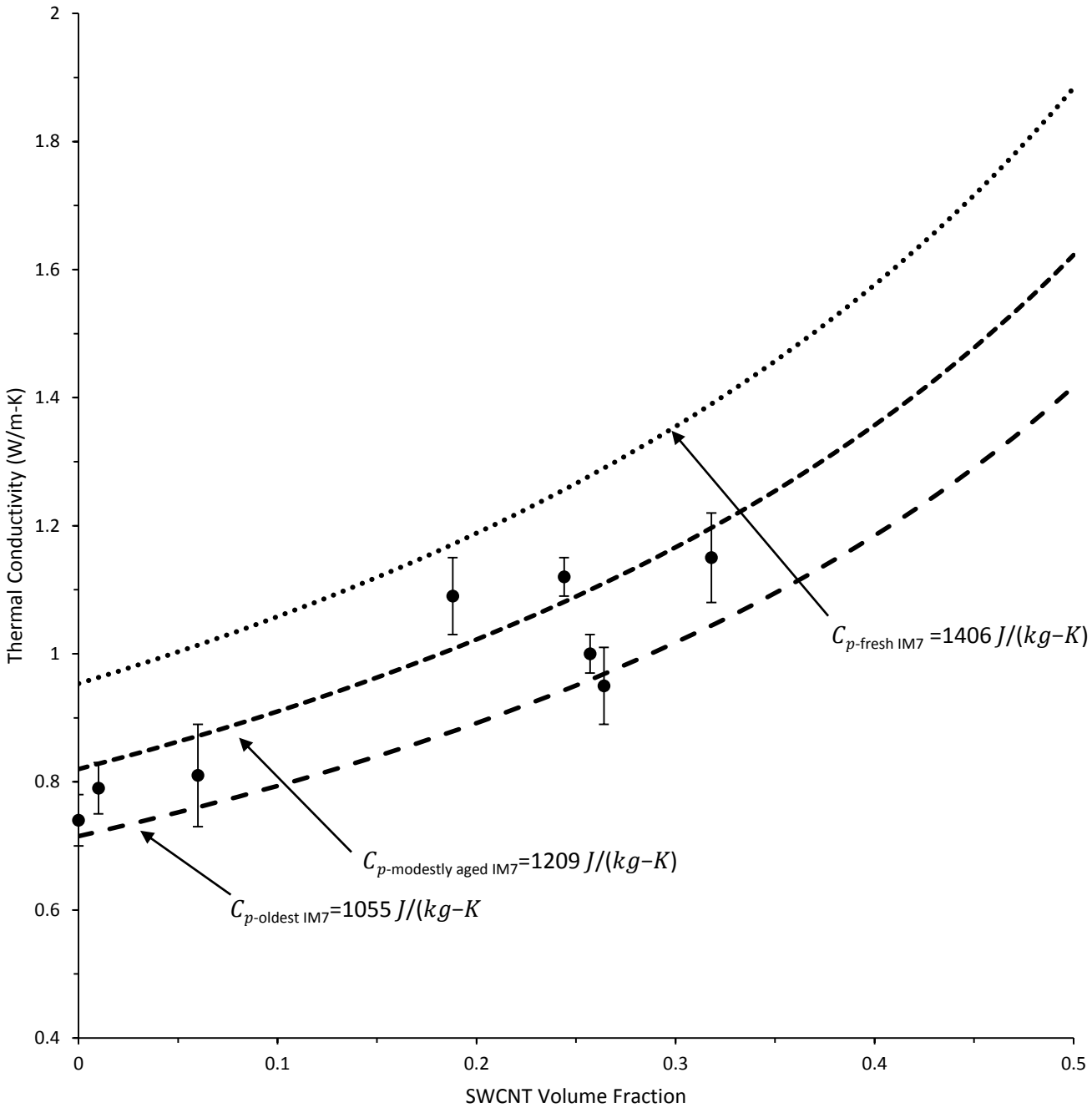

Figure 5.2–14. Predicted and experimental through-thickness thermal conductivities for IM7/SWCNT composites at 420 K. The predicted thermal conductivities are displayed as dashed lines for C_p values of 1055, 1209, and 1406 J/kg–K as estimated for oldest, moderately aged, and fresh IM7, respectively, at 420 K by equations 37 to 39.

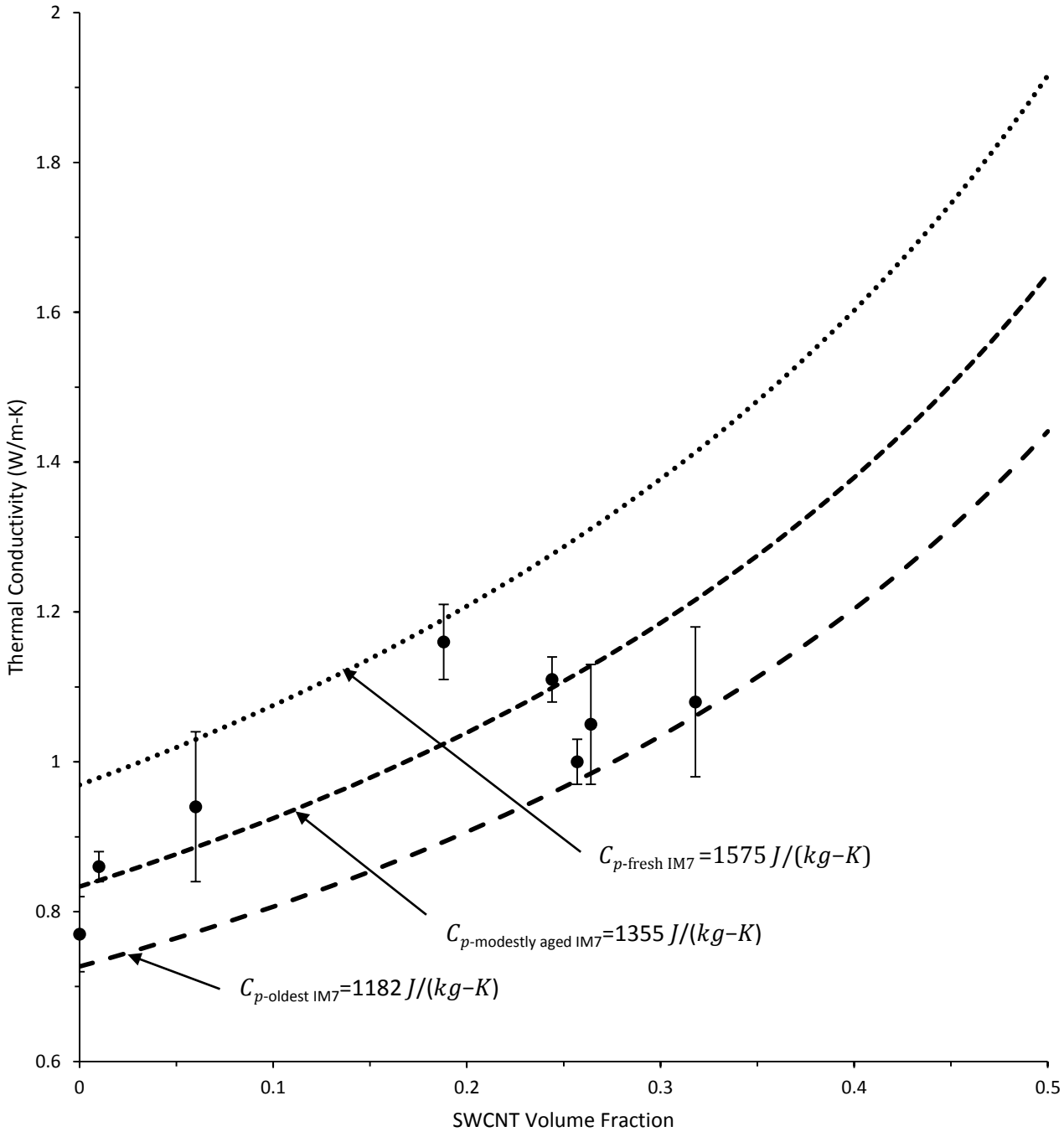

Figure 5.2–15. Predicted and experimental through-thickness thermal conductivities for IM7/SWCNT composites at 470 K. The predicted thermal conductivities are displayed as dashed lines for C_p values of 1182, 1355, and 1575 J/kg–K as estimated for oldest, moderately aged, and fresh IM7, respectively, at 470 K by equations 37 to 39.

As illustrated in Figures 5.2-8 to 5.2-15, the experimental thermal conductivity data obtained for the various IM7/SWCNT composites of different SWCNT content fit well within the ranges predicted, when the effects of aging on the heat capacity of IM7 is considered. The thermal conductivity data obtained at 170 K show the poorest agreement with the predictions, with data obtained at all the other temperatures generally falling within the predicted range. This level of agreement suggests that the predominate factors influencing the thermal conductivity of the IM7/SWCNT composites were the time-dependent properties of the IM7 and the SWCNT content in the composites.

From the above results, it is useful to focus on the properties of IM7 in the absence of SWCNTs. For my predicted through-thickness α values for IM7, polynomial trendlines could be obtained for the cases of oldest, moderately aged, and fresh IM7 as:

$$\alpha_{\text{oldest IM7}} = -9.257\text{x}10^{-9}T^3 + 9.521\text{x}10^{-6}T^2 + 3.619\text{x}10^{-4}T + 9.748\text{x}10^{-1} \quad (40)$$

$$\alpha_{\text{moderately aged IM7}} = -7.961\text{x}10^{-9}T^3 + 4.966\text{x}10^{-6}T^2 + 7.712\text{x}10^{-4}T + 2.043\text{x}10^{-1} \quad (41)$$

$$\alpha_{\text{fresh IM7}} = -6.943\text{x}10^{-9}T^3 + 4.331\text{x}10^{-6}T^2 + 6.725\text{x}10^{-4}T + 1.781\text{x}10^{-1} \quad (42)$$

where α is in W/m-K and T is temperature in degrees Kelvin. The through-thickness α values can be ascertained by requiring that the ratio of in-plane and out-of-plane thermal diffusivities remain constant (0.538 cm^2/s). In short, the thermal diffusivity of SWCNTs is assumed to be temperature independent.

The predicted values for through-thickness λ values for virgin IM7 samples over the entire explored temperature range are illustrated in Figure 5.2–16. The three predicted results (dotted, dashed and semi-dashed lines) represent the through-thickness λ at three C_p values relevant to IM7 as it ages (fresh, moderately aged, oldest, respectively). The solid lines present polynomial trend lines for each data set and that have similar R^2 values of 0.9987. The overall trend from the data is that as the C_p of IM7 has a higher value, the overall thermal conductivity of the prepreg composite also does. As shown in previous plots in this section, the addition of SWCNTs dispersed onto IM7 provides additional increases in the thermal conductivity to the resulting composite.

As stated earlier, acquiring values for in-plane measurements require specimens to have higher through-thickness thermal diffusivities of > 0.4 cm^2/s. From the theoretical models, the values of the through-thickness thermal diffusivity of IM7/SWCNT composite plies are averaging 0.025 cm^2/s which is too low by a factor of 10. Based on current literature and available technology, experimental methods to measure the in-plane thermal diffusivities and in-plane thermal conductivities of the prepared samples by direct means are not possible.

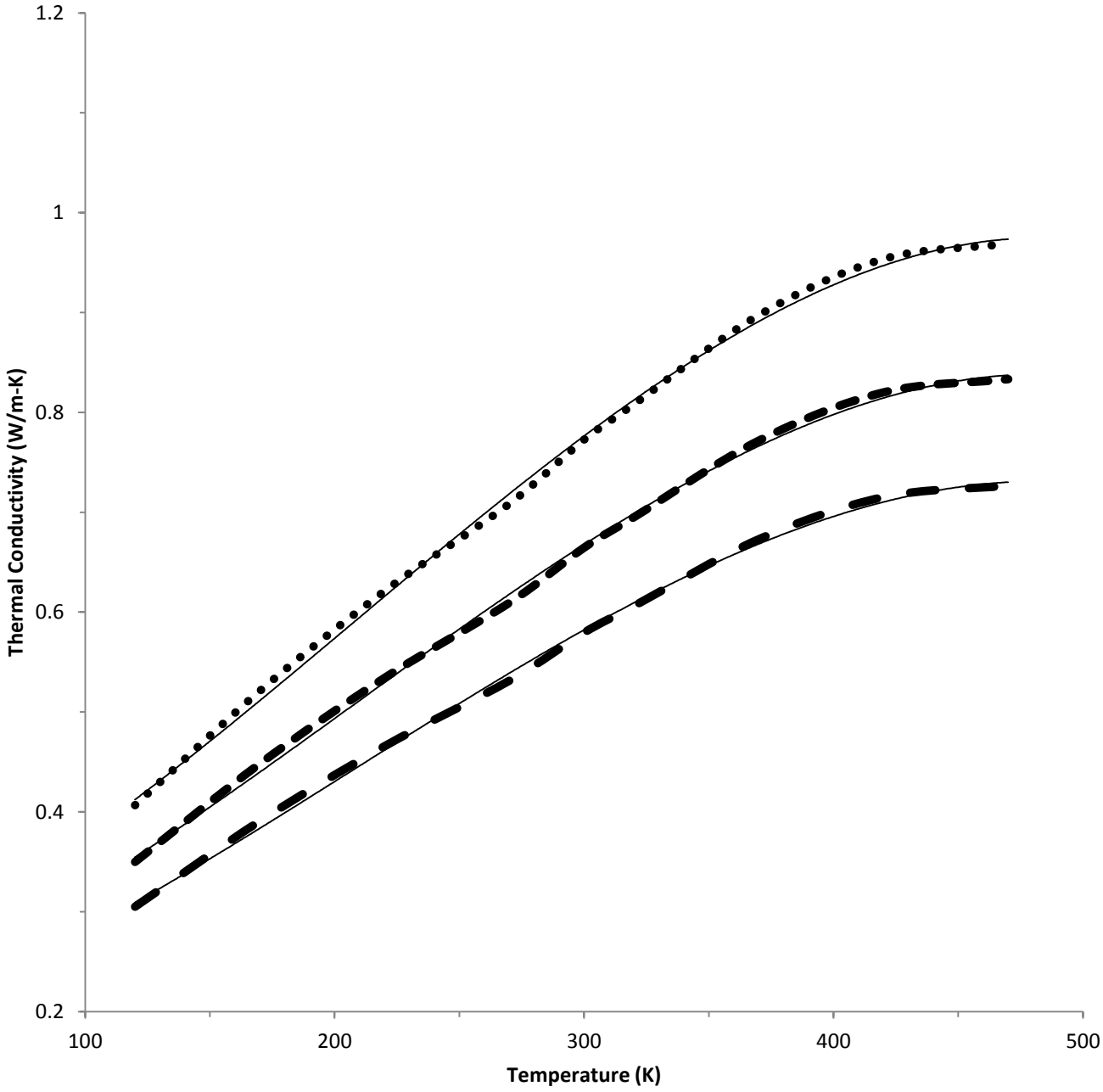

Figure 5.2–16. Predicted through-thickness thermal conductivities for virgin IM7 from 120 to 470 K. The predictions use estimated C_p values for oldest, moderately aged, and fresh IM7 samples (equations 37 to 39), as illustrated with semi-dashed, dashed, and dotted lines, respectively. Solid lines display fitting equations 40 to 42 on the plot.

5.3 FINITE ELEMENT MODELING

In this section, I report finite element modeling results for a thermal radiator having thermal properties for a IM7/SWCNT hybrid composite. These results are compared with those for similarly configured thermal radiators constructed from virgin IM7 and from Al 6016-T6, an aluminum alloy commonly used in heat transfer aerospace applications. For this section, the primary goal was to extend my experimental results to a case where such materials could find use in an aerospace application (e.g., a thermal radiator). Figures 5.3–1 and 5.3–2 show finite element modeling results for thermal radiators configured with a virgin IM7 panel on one side and the other constructed of the aluminum alloy or an IM7/SWCNT composite on the other side. The IM7/SWCNT composite considered in the finite element modeling was one having a SWCNT volume fraction of 0.32. This material exhibited the highest thermal transfer properties in my experiments.

The finite element model was constructed using Thermal Desktop^{TM} software created by the Advanced Concepts Team at NASA/Marshall Space Flight Center. Thermal Desktop^{TM} is a modeling program that operates by performing heat balances at different individual nodes of the structure. The Thermal Desktop^{TM} software was used to examine a thermal radiator as heat flows into it laterally and the heat is transferred into space from each node. The modeled thermal radiator consisted of a central cylindrical heat pipe (5 cm in diameter, and 1.0 m in length) that radiated heat at 300 K. The central heat pipe was connected to two panels, one on each side, each having dimensions of 0.5 m by 1.0 m and 3 mm in thickness (see Figures 5.3-1 and 5.3-2). The surface emissivity for the panels was 0.8, and the temperature of the panels could range from 3 to 300 K. In the simulation, the orientation of the panels faced toward the zenith where there would be no other solar or planetary inputs.

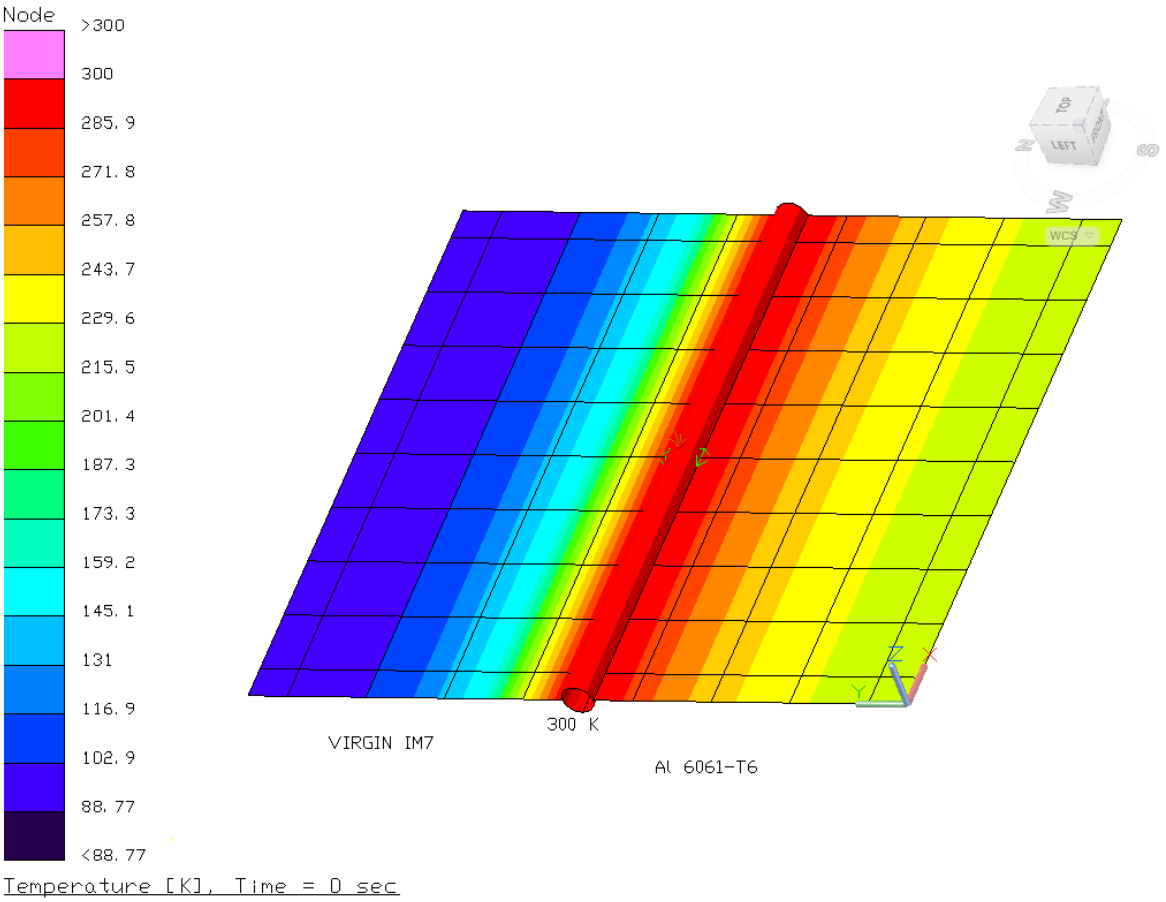

Figure 5.3–1. Finite element modeling results for a thermal radiator consisting of a central heat pipe at 300 K, and attached panels composed of virgin IM7 (on the left) and Al 6061-T6 (on the right). Heat from the radiator is transferred into space. Physical dimensions are provided in the text.

In the model, the virgin IM7 composite was assumed to have a through-thickness λ of 0.66 W/m–K at 300 K. This value was multiplied by 6 to obtain an in-plane λ of 3.96 W/m–K at 300 K that was used in the model. The factor of 6 was selected in estimating the in-plane value for λ, based on suggestions from Hexcel Inc. for their IM7 product. I again note that these values had to be estimated as the in-plane thermal conductivity for these materials are

not available from direct measurements. For the heat capacity of IM7, its value can change with aging. As such, the model used a value of 860 J/kg-K that represented the average expected over the lifetime of the thermal radiator. The C_p value of 860 J/kg–K represented a midpoint value between that for fresh IM7 (1000 J/kg–K as reported by its supplier, Hexcel Inc.) and that when IM7 has been in use for several years (~750 J/kg–K).

Figure 5.3–1 compares the thermal gradients across a thermal radiator where one side of the central pipe is connected to a sheet of virgin IM7 and the other side comprises a sheet of aluminum alloy 6061-T6. In the figure, the colors represent the temperature of the composite plies at specific locations as designated in the legend. In the modeled thermal radiator, the two sheets shared a common boundary condition at their junction with the cylindrical pipe that is set at 300 K as the result of an instantaneous (Time = 0) heat pulse that comes from the sun. The two sheets are similarly allowed to dissipate heat to the surroundings through their structures. From the simulation, the virgin IM7 panel on the left in Figure 5.3-1 shows a steeper temperature thermal gradient versus that for the aluminum alloy 6061-T6 on the right. As a result, the virgin IM7 panel provides a much lower ability to conduct heat as evidenced by the darker (i.e., bluer) colors exhibited. As such, virgin IM7 shows highly inferior results compared to the aluminum alloy.

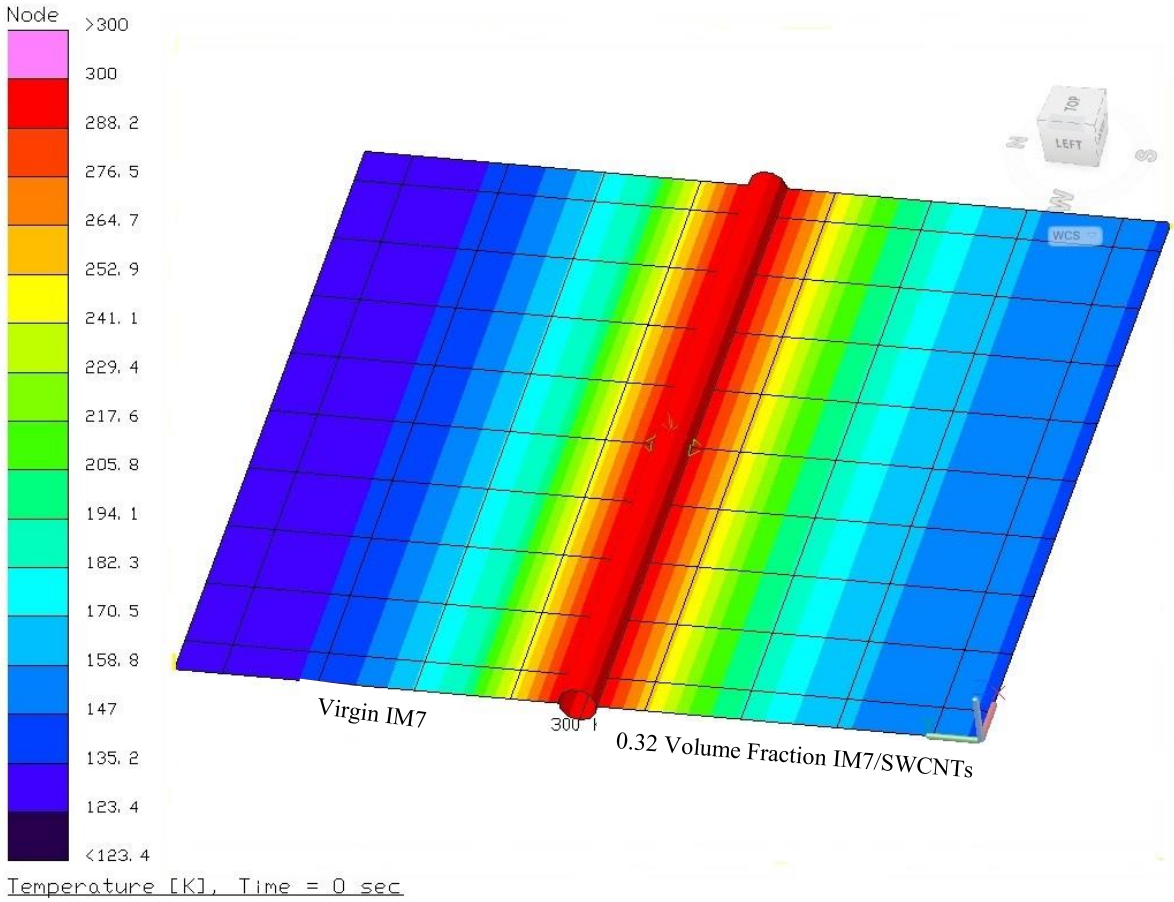

Figure 5.3–2. Finite element modeling results for a thermal radiator consisting of a central heat pipe at 300 K, and attached panels composed of virgin IM7 (on the left) and IM7/SWCNT hybrid composite with SWCNT volume fraction of 0.32 (on the right). Heat from the radiator is transferred into space. Physical dimensions are provided in the text.

Figure 5.3–2 provides a similar comparison where the thermal gradients across a thermal radiator of related constructions are shown. In the figure, one side of the central pipe is connected to a sheet of virgin IM7 (as in Figure 5.3-1) and the other side to a sheet of an IM7/SWCNT composite with a SWCNT volume fraction of 0.32. The two sheets share a common boundary condition at their junction with a cylindrical pipe at 300 K, and are allowed to similarly dissipate heat throughout their structures to the surroundings (space). Of the two

materials in Figure 5.3-2, the virgin IM7 shows the steeper temperature gradient. With the addition of the SWCNTs to the IM7, the temperature gradient was less steep at each individual node than for the virgin IM7 yielding a more conductive surface. The result is that there is increased heat flow for the IM7/SWCNT composite due to the presence of the incorporated SWCNTs. The heat flow through the IM7/SWCNT composite in Figure 5.3-2 is less than that for the Al 6061-T6 alloy in Figure 5.3-1. A comparison between these figures suggest that while the composite materials prepared in this work may not achieve the benchmarks for an aluminum alloy, they may be suitable for some applications where the thermal properties of virgin IM7 are insufficient. For aerospace applications, improvements in the heat transfer efficiency of IM7 could lead to useful weight savings in spacecraft and satellite constructions when used to replace traditional metallic alloys.

To summarize, this research identified a process to develop SWCNTs as additives to a IM7 composite ply and characterized their influence on various thermal properties. The SWCNTs were incorporated as stratified layers between IM7 plies. Through measurements of heat capacity and thermal diffusivity for these SWCNT-containing IM7 composites, improvements in the overall thermal conductivity in IM7 were achieved. As IM7 ages, its thermal conductivity can decrease by as much as 20 percent from its initial value due to related changes in the heat capacity of IM7. These decreases negatively influence the usefulness of IM7 in heat transfer applications; however, by the addition of SWCNTs as a dispersion to IM7, the overall thermal conductivity of IM7 can be made to overcome these losses and exceed values for virgin IM7. For these IM7/SWCNT composites, their interfacial resistance is reduced as the SWCNTs have a dominating influence on the phonon mean free paths to produce higher thermal conductivities throughout the prepreg structure. For the practical use of the IM7/SWCNT composites, another consideration is the coefficient of thermal expansion

for such composite materials. At elevated temperatures, the composite coefficient of thermal expansion increases (swells). As a result, the surface area increases in the composite and more greatly affects the mean free path than do the carbon nanotubes. Adversely, in certain processes (heat shields, thermal fins, efficient thermal radiators, etc.), having high thermal conductivities at lower temperatures are optimum.

CHAPTER VI

CONCLUSIONS

By introducing randomly single-walled carbon nanotubes (SWCNT) as an additive in IM7, the thermal conductivity of the resulting hybrid composites can be increased above their value for the virgin material. These novel composite structures were processed and characterized to improve their thermal properties. At the low temperatures encountered in outer-space environments, the addition of SWCNTs increases the thermal conductivity of IM7 composites by their presence. The interface resistance may play a role in the low thermal conductivities for these organic materials. This study showed that the addition of randomly oriented SWCNT as stratified layers within IM7 composites contributes to larger conductivity values that positively impact thermal transfer. The measured through-plane values are consistent with modeling results developed in this work. These models also predict that increases in the in-plane thermal properties of the IM7 composites by SWCNTs to be at least as high as the increases in the measured through-plane values that provided verification to the models. Highly efficient, directional heat dissipation is required for many components, pipes, and heat exchangers that comprise the thermal transfer and thermal control systems architectures in such systems such as those developed for the heavy-lift rocket under the Space Launch System (SLS) capability. Hence, the methods used in this work to add SWCNTs to a composite could offer an approach to positively impact the performance, capacity, reliability, and safety of future space vehicles.

Further studies should be done to assess the effect of using oriented SWCNTs as well as non-oriented and oriented multi-walled CNTs on the thermal properties of such hybrid composites. Related investigations on the use of different mixtures of solvents/acids to better

disperse the CNTs onto the IM7 prepreg composites would also be valuable. The development of an automated spray process would be essential for controlling the amount of CNTs deposited onto the prepreg composite and the resulting properties of the final composite structures.

REFERENCES

1. Ajayan, P.M. & Tour, J.M. (2007) Materials Science: Nanotube Composites. *Nature* **447**, 1066-1068.
2. Chakravarthi, Divya K. (2010) Carbon Nanotubes Filled Polymer Composites: A Comprehensive Study on Improving Dispersion, Network Formaulation and Electrical Conductivity. Houston, TX: Rice University.
3. National Research Council: Committee on High-Performance Structural Fibers for Advanced Polymer Matrix Composites. (2005) High-Performance Structural Fibers for Advanced Polymer Matrix Composites. Washington, D.C.: The National Academics Press.
4. Schlea M.R., Brown T.R., Bush J.R. Criss Jr. J.M., Mintz E. and Shofer M.L. (2010) Dispersion control and characterization in multiwalled carbon nanotube and phenylethynyl-terminated imide composites. *Composites Science and Technology* **70**, 822-828.
5. Engineering Materials Handbook™ Volume 1 Composites (1987).
6. Hussain, F., Hojiati, M., Okamoto, M. & Gorga, R.E. (2006) Polymer Matrix Nanocomposites, Processing, Manufacturing and Application: An Overview. *Journal of Composite Materials* **40**, 1511-1575.
7. Luo, J. & Daniel I.M. (2003) Characterization and modeling of mechanical behavior of polymer/clay nanocomposites. *Composites Science and Technology* **63**, 1607-1616.
8. Science Policy Section. (2004) Nanoscience and nanotechnologies: opportunities and uncertainties. London, England: The Royal Society.

9. Oberlin A, Endo M, Koyama T. (1976) Filamentous growth of carbon through benzene decomposition. *Journal of Crystal Growth* **32**(3), 335-349.
10. Iijima, S. (1991) Helical microtubles of graphitic carbon. Nature **354**, 56-58.
11. Bhushan B. and Marti O. (2004) Handbook of Nanotechnology. Springer-Verlag Berlin Heidelberg New York.
12. Kong J., Soh H-T., Cassell A-M., Quate C-F. and Dai H. (1998) Synthesis of individual single-walled carbon nanotubes on patterned silicon wafers. *Nature* **395**(29 October 1998), 878-881.
13. Berber S., Young-Kyun K. and Tomanek D. (2000) Unusually high thermal conductivity of carbon nanotubes. *Phys Rev Lett* **84**(20), 4613-4616.
14. Kim P., Shi L., Majumdar A., McEuen P.L. (2001) Thermal transport measurements of individual multiwalled nanotubes. *Phys Rev Lett* **87**(21), 215502-1.
15. Moisala A., Li Q., Kinloch I.A. and Windle A.H. (2006) Thermal and electrical conductivity of single- and multi-walled carbon nanotube-epoxy composites. *Composites Sci Technol* **66**(10), 1285-1288.
16. Chalopin Y., Volz S. and Mingo N. (2009) Upper bound to the thermal conductivity of carbon nanotube pellets. *J Appl Phys* **105**(8), 084301.
17. Park J-H. (2001) Chemical Vapor Deposition Surface Engineering Series Volume 2. ASM International, Materials Park OH 44073-0002.
18. Kunadian I., Andrews R., Qian D. and Pinar M. M. (2009) Growth kinetics of MWCNTs synthesized by a continuous-feed CVD method. *Carbon* **47**(2), 384-395.
19. Cheo J-L., Seung C-L., Hyoun-Woo K., Chong-Yun P.K and Cheol-Woong Y. (2002) Large-scale production of aligned carbon nanotubes by the vapor phase growth method. *Chemical Physics Letters* **359**(1-2), 109-114.

20. Zhang L, Tan Y and Resasco DE. (2006) Controlling the growth of vertically oriented single-walled carbon nanotubes by varying the density of Co{single bond}Mo catalyst particles. *Chemical Physics Letters* **422**(1-3), 198-203.
21. Flashline^{TM} Thermophysical Instruments: Operating and Service Manual. (2009) Anter Corporation, Pittsburgh PA.
22. Carslaw H.S. and Jaeger J.C. (1959) Conduction of Heat in Solids, 2nd Edition. Oxford University Press, London.
23. Taylor, R.E. (1975) Radiation loss in the flash method for thermal diffusivity. *J. Appl. Phys.* **46**(714), 714-719.
24. Standard Test Methods for Thermal Diffusivity by the Flash Method. ASTM Designation E 1461-01.
25. TA Instruments. (2013) Concentric In-Plane Method for Thermal Diffusivity Testing.
26. Veca M., Meziani M., Wang W., Wang X., Lu F., Zhang P., Lin Y., Fee R., Connell J. and Sun Y-P. (2009) Carbon Nanosheets for Polymeric Nanocomposites with High Thermal Conductivity. *Adv. Mater*. (21), 2088-2092.
27. Krapez J-C., Spagnolo L., Frieb M., Maier H-P and Neuer G. (2004) Measurement of in-plane diffusivity in non-homogeneous slabs by applying flash thermography. *International Journal of Thermal Sciences.* **43**, 967-977.
28. Zamel N., Litovsky E., Shakhshir S., Li X. and Kleiman J. (2011) Measurement of in-plane thermal conductivity of carbon paper diffusion media in the temperature range -20°C to 120°C. *Applied Energy* **88**, 3042-3050.
29. Haines P. J., "Principles of Thermal Analysis and Calorimetry," Royal Society of Chemistry, 2002.

30. Kappagantula K. and Pantoya M. (2012) Experimentally Measured Thermal Transport Properties of Aluminum-Polytetrafluoroethylene Nanocomposites with Graphene and Carbon Nanotube Additives. *Conference Publication, 40th Annual Conference of North American Thermal Analysis Society*, Orlando Florida.

31. Evseeva L.E. and Tanaeva S.A. (2008) Influence of the Concentration of Carbon Nanotubes (CNT) on the Thermophysical Properties of Epoxy/CNT Nanocomposites at Low Temperatures. *Mechanics of Composite Materials*, **44**(5), 487-494.

32. Dresselhaus M., Dresselhaus G. and Jorio A. (2007) Raman Spectroscopy of Carbon Nanotubes. *J. Phys. Chem. C.* **111**(48), 17887-17893.

33. Parás-Peña, L. (2010) Dispersion of Carbon Nanotubes in Vinyl Ester Polymer Composites. Rice University: Houston, Texas.

34. Practice Guide: Spectroscopy, http://www.msel.nist.gov/Nanotube2/Practice%20Guide_Section4_Spectroscopy.pdf.

35. Freiman S., Hooker S. and Miger K. (2008) Measurement Issues in Single Wall Carbon Nanotubes. National Institute of Standards and Technology, Washington D.C.

36. Wang S, Liang Z, Liu T, Wang B, Zhang C. (2006) Effective amino-functionalization of carbon nanotubes for reinforcing epoxy polymer composites. *Nanotechnology* **17**(6), 1551-1557.

37. Yang D, Rochette J, Sacher E. (2005) Functionalization of Multiwalled Carbon Nanotubes by Mild Aqueous Sonication. *J. Phys. Chem. B* **109**(16), 7788-7794.

38. Peng H, Alemany L, Margrave J, Khabashesku V. (2003) Sidewall Carboxylic Acid Functionalization of Single-Walled Carbon Nanotubes. *J. Am. Chem. Soc.* **125**(49), 15174-15182.

39. Arepalli S., Nikolaev P., Gorelik O., Hadjiev V.G., Holmes W., Files B. and Yowell L. (2004) Protocol for the characterization of single-wall carbon nanotube material quality. *Carbon* **42**(8-9), 1783-1791.

40. Hu Y., Shenderova O.A., Hu Z., Padgett C.W and Brenner D.W. (2006) Carbon nanostructures for advanced composites. *Rep. Prog. Phys.* **69**(6), 1847-1895.

41. Seyhan A., Gojny F., Tanoglu M. and Schulte K. (2007) Rheological and dynamic-mechanical behavior of carbon nanotube/vinyl ester-polyester suspensions and their nanocomposites. *European Polymer Journal* **43**(7), 2836-2847.

42. Gojny F.H., Wichmann M.H.G., Kopke U., Fiedler B. and Schulte K. (2004) Carbon nanotube reinforced epoxy-composites: enhanced stiffness and fracture toughness at low nanotube content. *Composites Science and Technology* **64**(15), 2363-2371.

43. Wang Y., Wu J. and Wei F. (2003) A treatment method to give separated multi-walled carbon nanotubes with high purity, high crystallization and a large aspect ratio. *Carbon* **41**(15), 2939-2948.

44. Moniruzzaman M., Du F., Romero N. and Winey K.I. (2006) Increased flexural modulus and strength in SWNT/epoxy composites by a new fabrication method. *Polymer* **47**(l), 293-298.

45. Chisholm N., Mahfuz H., Rangari V.K., Ashfaq A. and Jeelani S. (2005) Fabrication and mechanical characterization of carbon/SiC-epoxy nanocomposites. *Composite Structures* **67**(1), 115-124.

46. Park C., Ounaies Z., Watson K.A., Crooks R.E., Smith J., Lowther S.E., Connell J.W., Siochi E.J., Harrison J.S. and Clair T.L.S. (2002) Dispersion of single wall carbon nanotubes by in situ polymerization under sonication. *Chemical Physics Letters* **364**(3-4), 303-308.

47. Seyhan A.T., Gojny F.H., Tanoglu M. and Schulte K. (2007) Critical aspects related to processing of carbon nanotube/unsaturated thermoset polyester nanocomposites. *European Polymer Journal* **43**(2), 374-379.

48. Niyogi S., Hamon M., Perea D., Kang C., Zhao B., Pal S., Wyant A., Itkis M. and Haddon R. (2003) Ultrasonic Dispersions of Single-Walled Carbon Nanotubes. *J. Phys. Chem. B* **107**(34), 8799-8804.

49. Gibson R.F., Ayorinde E.O. and Wen Y. (2007) Vibrations of carbon nanotubes and their composites: A review. *Composites Science and Technology* **67**(1), 1-28.

50. Yang D., Rochette J. and Sacher E. (2005) Functionalization of Multiwalled Carbon Nanotubes by Mild Aqueous Sonication. *J. Phys. Chem. B* **109**(16), 7788-7794.

51. Hilding J, Grulke E. A., Zhang Z. G. and Lockwood F. (2003) Dispersion of Carbon Nanotubes in Liquids. *Journal of Dispersion Science and Technology* **24**(1), 1-41.

52. Strano M.S., Moore V.C., Miller M.K., Allen M.J., Haroz E.H., Kittrell C., Hauge R.H. and Smalley R.E. (2003) The Role of Surfactant Adsorption during Ultrasonication in the Dispersion of Single-Walled Carbon Nanotubes. (2003) J. Nanosci. Nanotech. **3**, 81-86.

53. Lee Y.H. (2005) Raman Spectroscopy and TGA of sonicated SWNTs with artificial defects. National Institute of Standards and Technology: *2nd Joint Workshop on Measurement Issues in CNTs*.

54. Lau K., Lu M., Chun-ki L., Cheung H., Sheng F. and Li H. (2005) Thermal and mechanical properties of single-walled carbon nanotube bundle-reinforced epoxy nanocomposites: the role of solvent for nanotube dispersion. *Composites Science and Technology* **65**(5), 719-725.

55. Safadi B., Andrews R. and Grulke E.A. (2002) Multiwall Carbon Nanotube Polymer Composites: Synthesis and Characterization of Thin Films. *Journal of Applied Science,* **84**, 2660-2669.

56. Hexply® Prepreg Technology. *Hexcel Corporation*, January 2013.

57. Hutchings I.M. (1992) Tribology: Friction and Wear of Engineering Materials. CRC Press, Inc. 2000 Corporate Blvd., N.W., Boca Raton, Florida, 33431.

58. Zhou S, Xu J., Yang Q-H., Chaing S., Li B., Du H., Xu C. and Kang F. (2013) Experiments and modeling of thermal conductivity of flake graphite/polymer composites affected by adding carbon-based nano-fillers. *Carbon*, **57**, 452-459.

59. Lee J-K. and Kim J-G. (2010) Generalized Self-Consistent Model for Predicting Thermal Conductivity of Composites with Aligned Short Fibers. *Materials Transactions*, **51**(11), 2039-2044.

60. Wang M., Kang Q. and Pan N. (2009) Thermal conductivity enhancement of carbon fiber composites. *Applied Thermal Engineering*, **29**, 418-421.

61. Grujicic M., Zhao C.L., Dusel E.C., Morgan D.R., Miller R.S. and Beasley D.E. (2006) Computational analysis of the thermal conductivity of the carbon-carbon composite materials. *Journal of Materials Science*, **41**, 8244-8256.

62. Silva G., Calado H., Musumeci A., Martens W., Waclawik E., Frost R. and George G. (2006) Polymer nanocomposite based on P3OT, TPU and SWCNT: preparation and characterization. *Proceedings of the 2006 International Conference on Nanoscience and Nanotechnology,* 182-185.

63. Strano M.S., Dyke C.A., Usrey M.L., Barone P.W., Allen M.J., Shan H., Kittrell C., Hauge R.H., Tour J.M. and Smalley R.E. (2003) Electronic Structure Control of Single-Walled Carbon Nanotube Functionalization. *Science*, **Sep 1**, 3011519-1522.

64. Chang T., Kisliuk A., Rhodes S., Brittain W. and Sokolov A. (2006) Conductivity and mechanical properties of well-dispersed single-wall carbon nanotube/polystyrene composite. *Polymer,* **47(22)**, 7740-7746.

65. Izard N. and Penicaud A. (2005) Raman studies of suspensions and solutions of single-wall carbon nanotubes. *Mater. Res. Soc. Symp. Proc.,* **858E**, HH1 1.1.1.

66. Liu J., Liu T. and Kumar S. (2005) Effect of solvent solubility parameter on SWNT dispersion in PMMA. *Polymer,* **46(10)**, 3419-3424.

67. Rols R., Alvarez, Anglaret A., Journet B., Sauvajol B., Maser M., Martinez L.F. and D-Girard A. (2000) Diameter distribution of single wall carbon nanotubes in nanobundle. *The European Physical Journal B - Condensed Matter and Complex Systems*, **18(2)**, 201-205.

68. Takahashi T. (2004) Dispersion and Purification of Single-Wall Carbon Nanotubes Using Carboxymethylcellulose. *Japanese Journal of Applied Physics,* **43(6A)**, 3636-3639.

69. Alvarez L. and Righi S.R. (2000) On the Raman Spectrum of Nanobundles of Single Wall Carbon Nanotubes. *Mater. Res. Soc. Symp. Proc.*, **593,** 107-112.

70. Anderson D.P. (2005) Hierarchical Morphology of Nanoconstituents In Water-Based Suspensions And Epoxy Resins By Scattering Techniques. *SAMPE Journal*.

71. Yang H., Wang S.C., Mercier P. and Akins D.L. (2006) Diameter-selective dispersion of singlewalled carbon nanotubes using a water-soluble, biocompatible polymer. *Chem. Commun.,* **(13)**, 1425-1427.

72. Murakami T., Kisoda K., Tokuda T., Matsumoto K., Harima H., Mitikami K., and Isshiki T. (2007) Raman and photoluminescence from dispersed single walled carbon nanotubes. *Diamond and Related Materials*, **16(4-7)**, 1192-1194.

73. Chou S.G. and Dresselhaus M. (2003) Raman Analysis of Carbon Nanotube Bundles for Bio-Electronic Applications. *Mat. Res. Soc. Symp. Proc.,* **737**, F3.18.1 - F3.18.5.

74. Utsumi S., Kanamaru M., Honda H., Kanoh H., Tanaka H., Ohkubo T., Sakai H. and Abe M. (2007) RBM band shift-evidenced dispersion mechanism of single-wall carbon nanotube bundles with NaDDBS. *Journal of Colloid and Interface Science* **308(l)**, 276-284.

75. Ritter U., Scharff P., Dmytrenko O., Kulish N., Prylutskyy Y., Belyi N., Gubanov V., Komarova L., Lizunova S., Shlapatskaya V. and Bernas H. (2007) Radiation damage and Raman vibrational modes of single-walled carbon nanotubes. *Chemical Physics Letters Oct 25,* **447(4-6)**, 252-256.

76. Girifalco L.A., Hodak M. and Lee R.S. (2000) Carbon nanotubes, buckyballs, ropes, and a universal graphitic potential. *Phys. Rev. B.,* **62(19)**, 13104-13110.

77. Hulman M., Pfeiffer R. and Kuzmany H. (2004) Raman Spectroscopy of Small-Diameter Nanotubes. *New Journal of Physics,* **6(1)**, 1-18.

78. Henrard L. Raman Spectroscopy of Carbon Nanotubes. http://perso.fundp.ac.be/~lhenrard/Pdf/ECONOS.pdf

79. Hone J., Batlogg B., Benes Z., Johnson A.T., and Fischer J.E. (2000) Quantized Phonon Spectrum of Single-Wall Carbon Nanotubes. *Science,* **289 (8 September 2000)**, 1730-1733.

80. Mäklin J., Halonen N., Toth G., Sápi A., Kukovecz, Á., Kónya Z., Jantunen H., Mikkola J. and Kordas K. (2011) Thermal diffusivity of aligned multi-walled carbon nanotubes measured by the flash method. *Phys. Status Solidi B.*, **248(11)**, 2508-2511.

81. Han Z. and Fina A. (2011) Thermal conductivity of carbon nanotubes and their polymer nanocomposites: A review. *Progress in Polymer Science*, **36**. 914-944.

82. Yoo L. and Kim H. (2011) Conductivities of Graphite Fiber Composites with Single-Walled Carbon Nanotube Layers. *International Journal of Precision Engineering and Manufacturing*, **12(4)**, 746-748.

83. Powell R. W., Ho C. Y. and Liley P.E. (1966) Thermal Conductivity of Selected Materials. *National Standards Reference Data System – National Bureau of Standards – 8 (Category 5 – Thermodynamics and Transport Properties).*

84. MatWeb: Material Property Data, http://www.matweb.com/index.aspx.

85. Chiang, I.W., Brinson B.E., Huang A.Y., Willis P.A., Bronikowski M.J., Margrave J.L., Smalley R.E. and Hauge R.H. (2001) Purification and Characterization of Single-Wall Carbon Nanotubes (SWNTs) Obtained from the Gas-Phase Decomposition of CO (HiPco Process) *J. Phys. Chem. B,* **105**, 8297 – 8301.

86. Cycom® 977-2 Epoxy Resin System, *Cytec Engineering Materials*, 19 March 2012.

87. Slough C.G. and Heese N.D. (2007) High Precision Heat Capacity Measurements of Metals by Modulated DSC®. **TA Instruments**.

88. Thomas L.C. (2013) Making Accurate DSC and MDSC Specific Heat Capacity Measurements with the Q1000 Tzero™ DSC. **TA Instruments**.